UCLA
UCLA Electronic Theses and Dissertations

Title
Estrogen Sulfotransferase-Mediated Imaging with Positron Emission Tomography in Moyamoya Syndrome

Permalink
https://escholarship.org/uc/item/94f695bq

Author
Surmak, Andrew John

Publication Date
2017

Peer reviewed|Thesis/dissertation

eScholarship.org Powered by the California Digital Library
University of California

UNIVERSITY OF CALIFORNIA

Los Angeles

Estrogen Sulfotransferase-Mediated Imaging with Positron Emission Tomography in Moyamoya Syndrome

A dissertation submitted in partial satisfaction

of the requirements for the degree

Doctor of Philosophy in Biomedical Physics.

by

Andrew John Surmak

2017

© Copyright by

Andrew John Surmak

2017

ABSTRACT OF THE DISSERTATION

Estrogen Sulfotransferase-Mediated Imaging with Positron Emission Tomography in Moyamoya Syndrome

by

Andrew John Surmak

Doctor of Philosophy in Biomedical Physics

University of California, Los Angeles, 2016

Professor Jorge R. Barrio, Chair

Moyamoya syndrome presents a cerebrovascular pathology that progressively introduces chronic ischemia. The network of collateral vessels created in response to arterial stenosis causes hypoperfusion and stimulates inflammatory insults that jeopardize the brain. Within this study, we used positron emission tomography (PET) to image inflammatory responses in patients with moyamoya syndrome and present the first report of [^{11}C]-PiB in moyamoya patients. [^{11}C]-PiB has a high affinity for estrogen sulfotransferase (SULT1E1), which is a metabolic enzyme for estrogen that varies with inflammation. We used an animal model to verify whether SULT1E1 corresponded to [^{11}C]-PiB signal. As moyamoya syndrome is susceptible to chronic ischemia, we

hypothesized that resulting insults in tissue would present inflammatory responses that would cause SULT1E1 to be elevated. In addition to moyamoya patients, we also included a patient with multiple sclerosis (MS) for scanning before and after immunomodulatory therapy to verify whether changes in inflammation could be seen with therapy. [^{11}C]-PiB produced a dynamic signal in response to inflammatory insults. In the animal model, the [^{11}C]-PiB signal was localized with dense SULT1E1 immunohistochemistry stains in the peri-infarct area not seen on the contralateral side. [^{11}C]-PiB SRTM DVR was markedly increased in the thalamus, pons, corona radiata and internal capsule of moyamoya patients when compared to controls ($p<0.01$). The MS patient had vast reduction in signal after one month of therapy that even achieved a 34% reduction in the right ventral pallidum. Collectively, these observations establish that [^{11}C]-PiB signal reflects heightened inflammatory responses from SULT1E1. Aß imaging with [^{11}C]-PiB is not a signal achieved in this report. Neither MS nor moyamoya involve amyloid-beta (Aß) as consequences of their progression. Therefore, the results in this report reflect [^{11}C]-PiB signal as a consequence of fluctuating inflammatory responses in diseases that lack Aß.

The dissertation of Andrew John Surmak is approved.

Sung-Cheng Huang

Nagichettiar Satyamurthy

Gary W. Small

Jorge R. Barrio, Committee Chair

University of California, Los Angeles

2017

DEDICATION

I dedicate this work to my family, without whom I would not have had the privilege of pursuing this work. My parents, Andrew and Eugenia, and Luisa, my sister, have been a source of strength that guided me through these years. Although my mother passed away on May 31, 2016, we are all bound spiritually through time.

TABLE OF CONTENTS

LIST OF FIGURES

LIST OF TABLES

ACKNOWLEDGEMENTS

My graduate studies at UCLA have been a testament of strength and character. I have learned things I did not expect to encounter and experienced things I could not envision. Consequently, there are many people who deserve commendation for helping me along this journey.

I must express immense gratitude to Koon-Pong Wong (KP) in Dr. Huang's group. Without his expertise, I would not have been able to learn the programming skills necessary to complete the image analysis. I would also like to thank Kenji Hirata, MD, PhD in the Department of Nuclear Medicine at Hokkaido University. During his two year Wagner-Torizuka Fellowship from the Society of Nuclear Medicine (SNM) with Dr. Huang, he also taught me computer programming. I must also thank Weber Shao, who was formerly with Dr. Huang but is now with Spokeo for help with troubleshooting for Matlab and R. KP, Weber and Kenji have also extended their friendship, for which I am very grateful. Kenji even opened his home and family to me, and all of us at one point or another enjoyed an evening on Sawtelle Boulevard. The camaraderie spent with them helped me to balance my time.

I must thank my laboratory colleagues, who also helped me through my period at UCLA. Jie Liu was very helpful with figures in this document; Jie also provided good advice for living in Los Angeles. Brendon Villegas and Jie also helped me move during my period, which was a great help. Matt Silverman also provided good wisdom about UCLA and always had creative humor. It is also necessary for me to thank Davis Woodworth, my BMP classmate in the Ellingson group, for his help with ADC and DWI MRI, as well as his indefatigable humor.

During my period at UCLA, I was a teaching assistant for Life Sciences 3 (Introduction to Molecular Biology), which was a very time consuming process. Nonetheless, the experience provided me with three invaluable undergraduate research assistants, whose acumen was more impressive than most in my program. Alex Aabedi, Omid and Payam Mirfendereski helped to propel the momentum of these studies and allowed me to focus. I will miss them as they matriculate to medical and dental school.

My work would not have progressed without mentorship. Saty was instrumental in helping me refine my thoughts with discussions on literature. Vladimir Kepe was also very helpful in guiding me with the directions of the project. Dr. Huang was very helpful with quantitative assessment and generation of parametric images. Finally, I would not have had the opportunity to learn and progress in my knowledge of molecular imaging without Dr. Barrio. He gave me the opportunity to learn about PET imaging, quantitative image analysis, and moyamoya. I am very grateful to these three professors and Vladimir for their mentorship but am even more thankful for their compassion they expressed upon the passing of my mother.

Finally, this work was funded in part by the following: National Institutes of Training Grant (EB002101-35; Oct 2011 – Sep 2012), National Institutes of Training Grant (EB002101-36; Oct 2012 – Sep 2013), Graduate Research Mentorship Fellowship (Sep 2013 – Jun 2014), Graduate Division Fellowship (Jun 2014 – Aug 2014), Edward J. Hoffman Fellowship (Jun 2014 – Aug 2014), Dr. Ursula Mandel Fellowship (Sep 2014 – Jun 2015), Philip & Aida Siff Educational Foundation Scholarship (Sep 2014 – Jun 2015), Graduate Division Fellowship (Jul 2015 – Dec 2015).

VITA

May 2003	The George Washington University, Washington, DC
	Elliott School of International Affairs
	B.A. – International Affairs
	(International Economics Concentration)
May 2006	American University, Washington, DC
	College of Arts and Sciences
	B.S. – Biochemistry (*magna cum laude*)
Dec 2009	The Johns Hopkins University, Baltimore, MD
	Whiting School of Engineering
	M.M.S.E. – Materials Science &
	Engineering/Nanotechnology Option
Sep 2012 – Jan 2017	University of California at Los Angeles, Los Angeles, CA
	David Geffen School of Medicine
	Graduate Student Researcher in Biomedical Physics
	Interdepartmental Program
	(Jorge R. Barrio, Ph.D. – Department of Molecular and
	Medical Pharmacology)
Jan 2017	University of California at Los Angeles, Los Angeles, CA
	David Geffen School of Medicine
	Ph.D. Candidate – Biomedical Physics

PUBLICATIONS

1. Shi J, Son MY, Yamada S, Szabova L, Kahan S, Chrysovergis K, Wolf L, **Surmak A**, Holmbeck K. "Membrane-type MMPs enable extracellular matrix permissiveness and mesenchymal cell proliferation during embryogenesis." *Dev Biol*. 2007 Oct 23. **PMID: 18022611**.

2. Rebustini IT, Myers C, Lassiter KS, **Surmak A**, Szabova L, Holmbeck K, Pedchenko V, Hudson BG, Hoffman MP. "MT2-MMP-Dependent Release of Collagen IV NC1 Domains Regulates Submandibular Gland Branching Morphogenesis." *Dev Cell*. 2009 Oct; 17(4): 482-93. **PMID: 19853562**.

3. Tuli R, **Surmak A**, Reyes J, Hacker-Prietz A, Armour M, Leubner A, Blackford A, Tryggestad E, Jaffee E, Wong J, DeWeese TL and Herman JM. "Development of a Novel Preclinical Pancreatic Cancer Research Model: Bioluminescence Image Guided Focal Irradiation and Tumor Monitoring of Orthotopic Xenografts." *Translational Oncology*. 2012. Volume 5, Issue 2. **PMID: 22496923**.

4. Tuli R, Armour M, **Surmak A**, Reyes J, Iordachita I, Patterson M, Wong J. "Accuracy of Off-Line Bioluminescence Imaging to Localize Targets in Preclinical Radiation Research." *Radiat Res.* 2013 Feb 22. **PMID: 23432050**.

5. Tuli R, **Surmak AJ**, Reyes J, Armour M, Hacker-Prietz A, Wong J, DeWeese TL, Herman JM. "Radiosensitization of Pancreatic Cancer Cells In Vitro and In Vivo through Poly (ADP-ribose) Polymerase Inhibition with ABT-888." *Transl Oncol*. 2014 May 13. pii: S1936-5233(14)00038-2. **PMID: 24836647**.

6. Hirata K, Kobayashi K, Wong KP, Manabe O, **Surmak A,** Tamaki N, Huang SC. "A semi-automated technique determining the liver standardized uptake value reference for tumor delineation in FDG PET-CT." *PLoS One*. 2014 Aug 27;9(8):e105682. **PMID: 25162396.**

Chapter One: Introduction

1.1 - Moyamoya Syndrome

Moyamoya (もやもや)is a Japanese term for "puff of smoke" that resembles the angiographic profile of a collateral network of leptomeningeal vessels branching from the basal ganglia; the term "moyamoya" in itself refers to the network of collateral vessels that develop after major arterial stenosis in the brain. This pattern of collateralization is a response to stenosis of major arterial vessels supplying the brain. Moyamoya disease is a classification of moyamoya syndrome, as the branching network of subcortical collateral vessels is a consequence of arterial stenosis in both instances. The diagnostic guidelines for moyamoya disease entail the following:

1.) intimal thickening of the internal carotid artery at the terminal segment (C7), where bilateral stenosis or occlusion of the lumen occurs typically
2.) variable stenosis in arteries of the Circle of Willis that include the anterior and middle cerebral arteries in addition to the posterior communicating arteries, all of which demonstrate fibrocellular intimal thickening, a waving of elastic lamina and attenuation of the medial wall
3.) small yet abundant perforations and anastomic branches around the Circle of Willis
4.) reticular conglomerates of small vessels witnessed in the pia matter (Fukui, 1997).

When Suzuki and Kodama reviewed 100 cases between 1961 and 1980, the angiographic presentation and pathologic findings lacked uniformity, yet intimal thickening and aberrations in the elasticity of lamina from either thickening or deficiencies were prominent (Suzuki and Kodama, 1983). This seminal review and other studies referenced cases of moyamoya syndrome. Stenosis in the internal carotid, anterior or middle cerebral arteries, or a combination of thereof, was found in conjunction with a

subcortical vascular network in patients with moyamoya syndrome. Unilateral progression is not a definitive diagnostic criterion, yet arteriosclerosis, brain tumors, Down's syndrome, Recklinghausen's disease, radiation therapy to the head and autoimmune diseases among others constitute underlying diseases that present certain risk factors for moyamoya syndrome (Burke *et al.*, 2009; Research Committee on the *et al.*, 2012). Hence, the presence of moyamoya vessels manifests a response to sustain and divert cerebrovascular flow in a variety of conditions, all of which jeopardize principal circulatory structures with stenosis. When patients present with these angiographic findings in the absence of aforementioned risk factors, then moyamoya disease is an appropriate diagnosis. Otherwise, moyamoya syndrome is an appropriate diagnosis for stenosis of principal cerebral arteries that are in the presence of branching collateral vessels.

Moyamoya vessels and their impact differ between pediatric and adult patients. The compliance of vessels differs among pediatric and adult patients with moyamoya disease such that pediatric vessels are more dilatory and less stenotic than adult patients (Yamashita *et al.*, 1983). Ischemia and cognitive impairment are more common in children than adults, but hemorrhaging and seizure are also possible (Weinberg *et al.*, 2011a). Pediatric cases will also involve occlusion of the ipsilateral ICA and Posterior Carotid Artery (PCA) and make children susceptible to hemiplegia (Mugikura *et al.*, 2002). Arterial stenosis causes the brain to develop collateral flow from smaller vessels that are within the leptomeningeal spaces. These vessels within the leptomeningeal spaces, however, define the progression of the disease in both children and adults.

Figure 1.1: Suzuki Staging of Moyamoya Disease

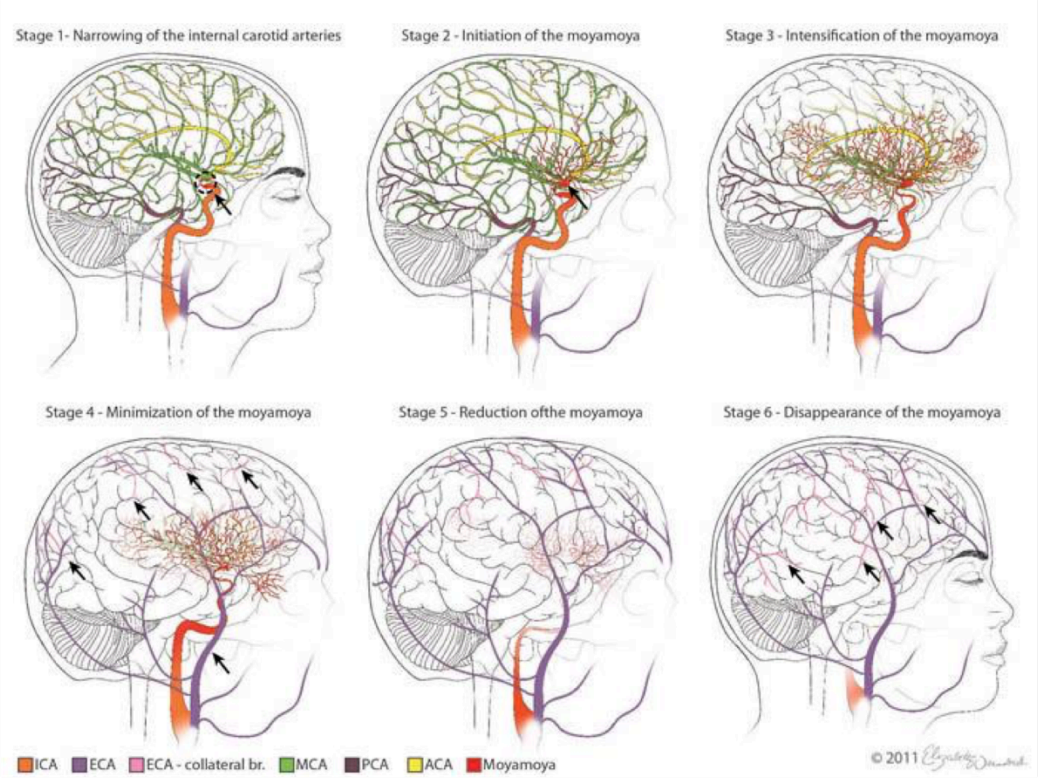

Weissbrod, E. 2011 (https://www.childrenshospital.vanderbilt.org/services.php?mid=9170**)**

An illustrated diagram of Suzuki staging in moyamoya disease, as proposed by Suzuki and Takaku in 1969. Stages 1-6 illustrate how the occlusion of the internal carotid arteries influence stenosis throughout the Circle of Willis and give rise to moyamoya collateral vessels. The moyamoya collateral vessels ultimately divert from the internal carotid artery to the external carotid artery. Moyamoya syndrome caused by other risk factors, such as radiation or neurofibromatosis, also inflicts arterial stenosis throughout the brain, which causes the development of moyamoya collateral vessels to restrict flow.

The coordinated collateral flow in response to stenosis within moyamoya disease can pose a significant threat to patients over time. Figure 1.1 illustrates the staging of moyamoya disease proposed by Suzuki and Takaku in 1969 (Weissbrod, 2011). The disease begins through stenosis of the ICA in Stage 1, which gives rise to the collateral vessels in Stage 2. Stage 3 witnesses the amplification of the moyamoya vessels. Ultimately in Stages 4-6, the moyamoya vessels will diminish and enable further

occlusion in the Circle of Willis, yet the external carotid artery (ECA) will facilitate flow for the ICA in the end stages of the disease. As the brain adjusts flow to compensate for deficient flow in the ICA, the moyamoya vessels within the leptomeningeal spaces develop in response to occlusion in the Circle of Willis. It is necessary to emphasize that the collateralization develops in response to stenosis, yet the pattern of vasculopathy is not entirely uniform in each risk factor associated with moyamoya syndrome. The pattern of collateralization may differ from the Suzuki stages in different cases of moyamoya syndrome. Ultimately, however, these vessels form from prolific angiogenic activity in the leptomeningeal space following arterial stenosis and cause damage from inadequate flow.

Moyamoya vessels have demonstrated a distinct profile that distinguishes itself from atherosclerotic cerebrovascular disease. Moyamoya vessels had significantly elevated microvascular density and diameter, microvascular surface per unit area, and arterial and microvascular mean transit times when compared to both healthy and atherosclerotic patients (Czabanka *et al.*, 2008). Additionally, the number of circulating progenitor endothelial cells in moyamoya vessels were substantially higher than those documented in healthy and atherosclerotic patients (Rafat *et al.*, 2009). The pronounced vessel density and delayed hemodynamics of the moyamoya collateralization constitutes an ischemic threat.

1.2 - Diagnostic Assessment of Moyamoya with Imaging

Present conventions for imaging moyamoya involve a variety of modalities that fundamentally identify hemodynamic abnormalities. Table 1.1 summarizes the modalities and their clinically observed outcomes (Lee *et al.*, 2009). Essentially, each of the imaging

modalities will reflect impaired cerebral blood flow (CBF). Stenosis can increase vascular resistance and reduce cerebral positive pressure (CPP) beyond the autoregulatory capacity that keeps CBF constant by exhausting the oxygen exhaustion fraction (OEF) (Lee *et al.*, 2009).

Table 1.1: Summary of Conventional Diagnostic Imaging Methods for Hemodynamic Assessment in Moyamoya Patients

Modality	Image Contrast Agent	Hemodynamic Measures	Hemodynamic Indicators
PET	$^{15}O_2$, $C^{15}O_2$, $H_2{}^{15}O$	CBF, CBV, rOEF	↓CBF, ↑rOEF
SPECT	^{133}Xe, ^{99m}Tc-HMPAO, ^{99m}Tc-ECD, ^{123}I-IMP	CBF	↓CVR*
Xe-CT	Stable Xenon Gas	CBF	↓CVR*
Dynamic Perfusion CT	Iodinated Contrast	CBF, CBV, MTT, T_{max}	↓CBF, ↑MTT, ↑CBV, ↓CBF
Dynamic Susceptibility Contrast Perfusion MRI	Gadolinium	CBF, CBV, MTT, T_{max}	↑T_{max}, ↑MTT, Mismatch between perfusion and diffusion weighted images
Arterial Spin Labeled Perfusion MRI	None	CBF	↓CBF, ↓CBF*
Ultrasound Doppler	None	Blood Flow Volume for ICA	↓CBF+

Contents summarized from Lee M., et al. *Neurosurg Focus* 2009; 26(4): E5. *Postvasodilatory Challenge from either acetazolamide or CO_2. +Estimation compared with contralateral hemisphere.

A summary of diagnostic modalities used to assess hemodynamic abnormalities in moyamoya patients. CT, MRI, PET, SPECT, and Ultrasound Doppler establish hemodynamic indicators that reflect impaired perfusion. Cerebral vascular reserve is established after a vasodilatory challenge that gauges the autoregulatory response to keep cerebral blood flow constant after a drop in cerebral positive pressure. Cerebral Blood Flow, Cerebral Blood Volume, Mean Transit Time, Time to Peak Contrast Signal, Cerebral Vascular Reserve, and relative Oxygen Extraction Fraction (CBF, CBV, MTT, Tmax, CVR, and rOEF, respectively).

Figure 1.2.1: Preoperative and Postoperative Evaluation Using [$^{15}O_2$]-gas PET and [^{123}I]-IMP SPECT

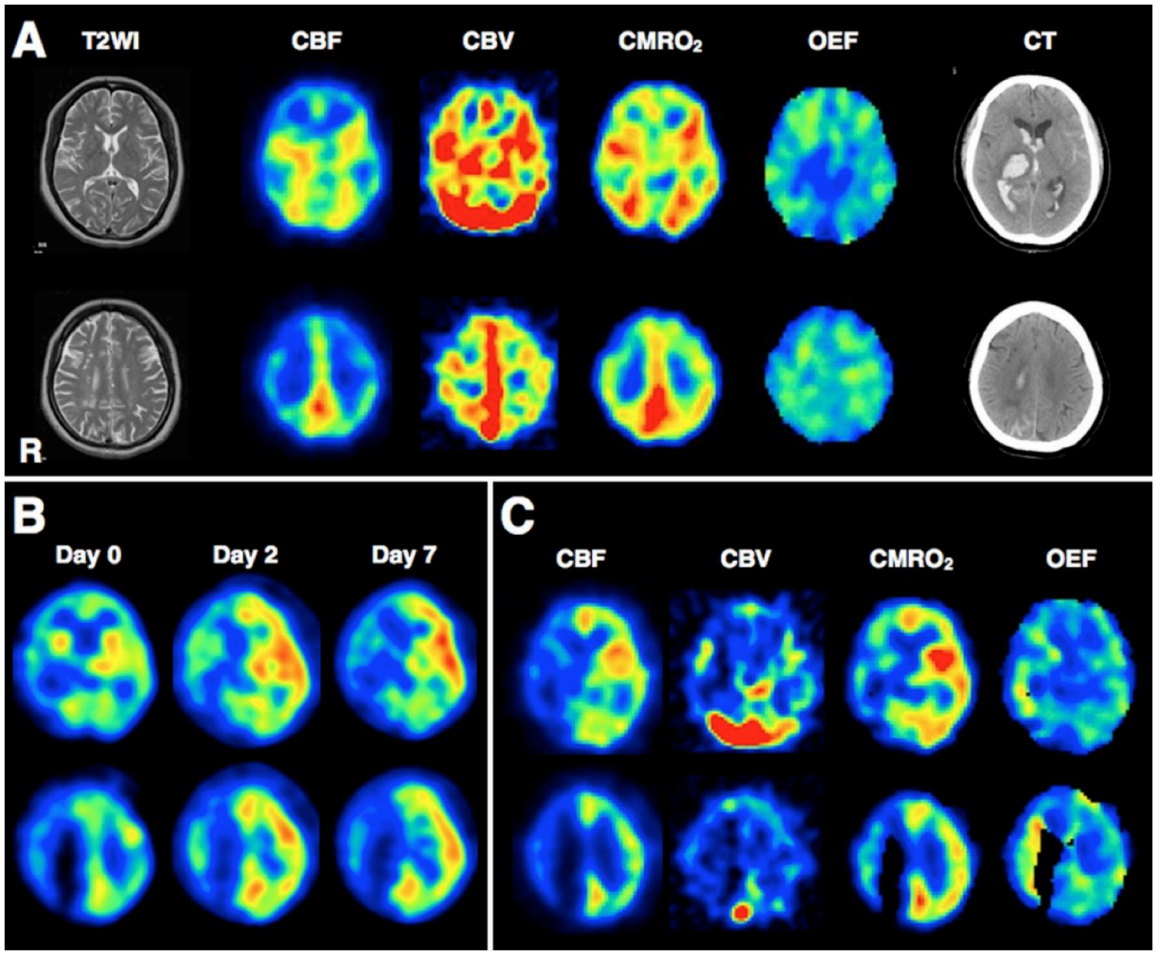

Uchino H, *et al*. Stroke. 2012;43:2610-2616.

A case report of a 52-year old female patient with moyamoya disease, who required bypass surgery to alleviate impaired flow. Surgery on the patient's left side followed an intracerebral hemorrhage in the right thalamus six months earlier. Images presented here are in radiologic convention. The higher row in each panel represents the transaxial image of the basal ganglia, while the lower row represents a plane superior to the basal ganglia. Panel A shows preoperative T2 weighted MRI confirmation of rarefaction in white matter and increased flow, whereas CT shows damage from hemorrhage in the right thalamus. Preoperative [$^{15}O_2$]-gas PET scans indicated decreased frontal CBF and $CMRO_2$ (Cerebral Metabolic Oxygen Rate) but elevated CBV and OEF. Postoperative [^{123}I]-IMP SPECT scans in Panel B show that frontal flow resumed immediately after surgery yet hyperperfusion in the left frontal lobe followed on days 2 and 7 after surgery. Postoperative [$^{15}O_2$]-gas PET scans one month after surgery in Panel C show stabilization of CBF, CBV, $CMRO_2$, and OEF in the patient's left hemisphere.

Figure 1.2.1 demonstrates a number of these hemodynamic indicators in a case of 52-year old female moyamoya patient who received bypass surgery six months on her left side after an intracerebral hemorrhage in the right thalamus (Uchino *et al.*, 2012). Her preoperative [$^{15}O_2$]-gas Positron Emission Tomography (PET) images in Panel A show bilateral frontal lobes with reduced CBF and cerebral metabolic rate of oxygen ($CMRO_2$), yet an elevated OEF and cerebral blood volume (CBV). Panel B shows postoperative CBF with [^{123}I] *N*-isopropyl-*p*-iodo-amphetamine single photon emission CT ([^{123}I]-IMP SPECT). Restoration of bilateral flow immediately after surgery encountered hyperperfusion in the patient's left frontal lobe on days 2 and 7 after surgery. One month after surgery, the patient's left hemisphere had resumed normal CBF, CBV and OEF ([$^{15}O_2$]-gas PET images in Panel C). PET and SPECT can assess hemodynamic indicators in moyamoya that can change with therapeutic intervention and progression of the disease. They also can establish some form of hemodynamic risk.

Moyamoya patients have chronically impaired cerebral vascular reserve (CVR) on account of variable CPP. CVR measures the vasodilatory ability to sustain CBF when CPP falls (Powers, 1991). Assessment of CVR requires a physiological challenge, which can either be through the administration of carbon dioxide or acetazolamide, which is a carbonic anhydrase inhibitor and vasodilator. CVR is then measured as the difference between CBF before and after the challenge divided by the baseline CBF (Vagal *et al.*, 2009). [^{123}I]-IMP SPECT, for example, has reliable CVR determination that has been validated with $H_2{}^{15}O$ PET (Ogasawara *et al*., 2003). Reliable CVR assessment in moyamoya patients underscores the severity of their reserve depletion from compromised flow and CPP. Patients who started with a low baseline CBF that demonstrated no

increase after acetazolamide present a high risk that may warrant surgical bypass or other intervention to establish hemodynamic stability (Rogg *et al*., 1989). The impact of reduced CBF, therefore, merits serial imaging where possible to monitor progression of disease.

Diagnosis and surveillance of moyamoya relies extensively on MRI. MRI lacks the radiation from PET, SPECT, and CT. Dynamic susceptibility contrast (DSC) MRI happens to a very versatile modality that provides useful hemodynamic parameters. DSC MRI also provides useful insight when paired with diffusion MRI that can demonstrate inverse signals, as Table 1.1 notes. Figure 1.2.2 shows a seven-year old boy with sickle cell anemia who had right-sided hemiparesis 5 weeks prior to scanning and reported disparate velocities between his right and left ICA/MCA with transcranial doppler (Kirkham *et al*., 2001). Here, MR angiography (MRA) confirms severe bilateral turbulence in the Left and Right ICA and moyamoya collaterals off of the right MCA. T2-weighted MRI indicates a left occipital infarct that is bright to reflect tissue damage. This location of this infarct is consistent in both diffusion-weighted and apparent diffusion coefficient (DWI and ADC, respectively) MRI. Moreover, this mismatch between MTT and the dark appearance of the left occipital infarct suggests an infarct from a while ago. The perfusion abnormalities in this patient show decreased CBF, increased mean transit time (MTT), and decreased CBV in the same area as the infarct. MTT is defined as CBV/CBF but indicates the amount of time that blood cells spend in capillary circulation. An increased MTT is proportional to an increased OEF and results when CPP falls. Here, MTT is also elevated on the patient's right hemisphere, where the arrows also highlight low CBF. DSC MRI also provides a map for T_{max}, which is the time

required for peak signal to achieve detection. Gadolinum delivery should be rather uniform with normal perfusion but can experience delay with cerebrovascular disease.

Figure 1.2.2: Perfusion Abnormality Detection Using Dynamic Susceptibility Contrast MRI

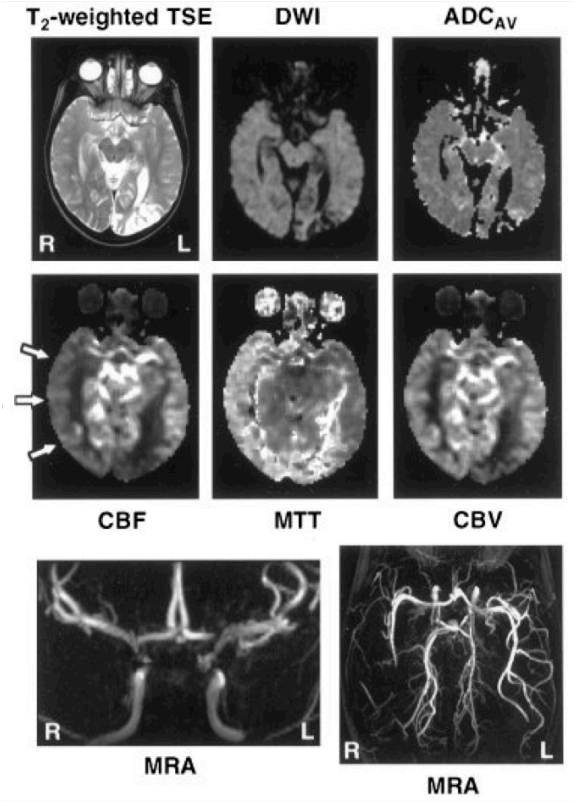

Kirkham FJ, *et al*. *Ann Neur* 2001; 49(4): 477-85.

A case report featuring a seven-year old pediatric patient with sickle cell disease that developed moyamoya collateral vessels. Dynamic susceptibility contrast MRI is presented with diffusion-weighted and apparent diffusion coefficient MRI (DWI and ADC, respectively) to reveal darkness in a left posterior infarct confirmed with bright T2 signal in the same region. Decreased CBF and CBV is presented in the infarcted region alongside suppressed CBF in the right hemisphere, as indicated by arrows. Increased MTT is present where flow is decreased. Magnetic Resonance Angiography reveals turbulence in the internal carotid arteries and moyamoya collateral vessels stemming off of the right middle cerebral artery (bottom left and right, respectively).

Figure 1.2.3 shows a male 19-year old moyamoya patient who has a fluid attenuated inversion recovery (FLAIR) MRI (a), ASL MRI (b) and T_{max} (c) (Lee *et al*., 2009). An arrow in the ASL MRI is consistent with the T_{max} map in the same region, thus verifying reduced flow in the left posterior cerebral artery. ASL, unlike DSC MRI, does not use contrast agent and reports signal from water in the vessels. ASL, though, will only provide CBF. The parameters afforded by DSC imaging, therefore, are useful when assembled collectively to evaluate perfusion abnormalities resulting from moyamoya collaterals.

Figure 1.2.3: FLAIR, ASL and T_{max}

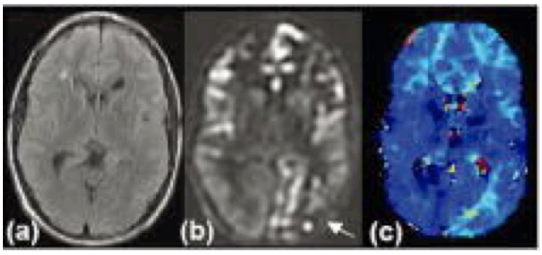

Lee M., *et al*. *Neurosurg Focus* 2009; 26(4):E5.

A case report featuring a nineteen-year old male patient with moyamoya. Panel (a) shows a fluid-attenuated inversion recovery (FLAIR) MRI with perturbed flow in the left posterior cerebral artery. This is clearer in panel (b) with the arrow pointing in the arterial spin-labeled MRI. Increased T_{max} in panel (c) conformed the reduced left posterior flow.

Collateralization in moyamoya patients develops over time and recruits a wide range of leptomeningeal and deep parenchymal vessels, the latter of which have poorer development in the basal ganglia (Liebeskind, 2003). Extensive arterioles arising directly from the circle of Willis and its proximal branches supply both the basal ganglia and brainstem but experience enhanced susceptibility to mechanical stresses imposed by chronic hypertension or stiffening of large arteries and reductions in blood flow (Brown

et al., 2007; Scuteri *et al.*, 2011; Soros *et al.*, 2013). Deep white matter structures, such as the centrum semiovale, corona radiata and periventricular white matter, that are supplied by these long arteries and arterioles have low persistently perfusion pressure (Wodarz, 1980; Moody *et al.*, 1990). Diminished media in moyamoya vessels also compromise compliance that stabilizes cerebral perfusion. The loss of arterial and arteriolar distention threatens autoregulatory responses in cerebral blood vessels that aim to sustain constant cerebral blood flow (Heistad *et al.*, 1990). Consequently, chronic ischemia ensues in structures that are perfused by collaterals.

Imaging studies have investigated white matter and subcortical structures to verify that they are indeed at risk from moyamoya collaterals. Diffusion tensor imaging (DTI) MRI confirmed that microstructural changes in white matter pose a greater risk than in cortical tissue (Kazumata *et al.*, 2015). Fractional anisotropy (FA) reflects the integrity of the neuron by establishing if diffusion is restricted during DTI imaging and was lower in white matter of moyamoya patients when compared to controls. Diffusion Kurtosis Imaging (DKI) demonstrated microstructural changes in the corona radiata, corpus callosum, frontoparietal subcortical white matter and thalamus of moyamoya patients (Kazumata *et al.*, 2016a). The study used both DTI and DKI, which has fewer constraints than DTI with respect to spatial orientation and represents tissue microstructure well (Jensen *et al.*, 2005). DTI and DKI parameters were inversely correlated but nonetheless confirmed both demyelination (RD/RK) and axonal loss (AD/AK) in the aforementioned structures. Ultimately, chronic insufficient flow established microstructural changes in white matter of moyamoya patients to impact core neural pathways associated with working memory and attention (Kazumata *et al.*, 2016b).

ADC MRI has also achieved similar results to show the perilous state of white matter in moyamoya patients. Normally appearing white matter had elevated ADC signal in the impaired hemisphere with a higher T_{max}, decreased FA, and higher asymmetry indices for ADC and FA in moyamoya patients when compared to controls (Jeong *et al.*, 2011). A similar study found the normally appearing white matter in moyamoya had an elevated ADC in the hemisphere with a negative CVR (Conklin *et al.*, 2010). The impact of these and other studies help to build off of information from perfusion studies to realize the damage posed by moyamoya vessels. Moyamoya is a chronic condition that persists. While the inflammatory nature of the disease may change over time, the threat of chronic hypoperfusion is resilient in the brains of moyamoya patients.

1.3 - Clinical Presentation of Moyamoya

Chronic hypoxic insults from moyamoya present themselves as long-term threats from hemodynamic instability. Moyamoya patients with reduced frontal cerebrovascular reserve, as defined by cerebral blood volume normalized to cerebellar blood volume, presented with dysexecutive cognitive syndrome (Calviere *et al.*, 2012). In a cohort of twenty patients with moyamoya but no ischemic stroke, small hyperintensities on T2 MRI were observed with cognitive impairment, executive dysfunction and heightened anxiety and distress (Karzmark *et al.*, 2012). A case report of an elderly female patient with an acutely confused state in the absence of prior psychiatric illness or neurodegenerative disease witnessed the presence of moyamoya vessels and bifrontal ischemic lesions (Nakanishi *et al.*, 2010). Another case report of a 23-year old male presented an interesting comorbidity of moyamoya with schizophrenia that exemplified executive dysfunction and stimulus driven behavior (Lubman *et al.*, 2003). Hence,

aberrations in cerebrovascular flow associated with moyamoya can manifest detriments to cognition, executive function and mood.

Moyamoya has different impacts in both adult and pediatric patients, with hemorrhage more common in the latter and chronic hypoxia from weak collateral vessels in the former. Intelligence is particularly vulnerable in pediatric moyamoya patients, whereas the greatest threat in adult moyamoya patients is diminished executive dysfunction (Weinberg *et al.*, 2011b). Presurgical neuropsychological evaluation of thirty-six adult patients with moyamoya disease revealed moderate to severe cognitive impairment in fifteen patients, mild to moderate depression in seven patients, high rates of executive dysfunction reflected in initiation and mental set-shifting efficiency (Karzmark *et al.*, 2008). By comparison, preoperative neuropsychological evaluation of pediatric moyamoya patients revealed prevalent reduction of the intelligence quotient, which was more severe in older patients and those with a markedly decreased mean CBF (Ishii *et al.*, 1984). Surgical revascularization has demonstrated improvements in neurocognitive status (Jefferson *et al.*, 2006). The impact of chronic hypoxia from moyamoya, however, is not permanently reversed with surgery.

The presentation of moyamoya is unmistakably identifiable with angiography, yet the symptoms associated with moyamoya may be less discriminating. Moyamoya introduces confounding factors for presentation of neurodegenerative diseases in adults. In a prior report of three cases where moyamoya patients were originally diagnosed with MS, patients presented with demyelination as seen on frontal biopsies, diffuse inflammation on MRI and oligoclonal bands in cerebrospinal fluid that evolved into migraines, dysphasia and hemiparesis (Dorfman *et al.*, 2012). In the aforementioned

study, the patients' confirmed arterial stenosis with MRI and correct diagnoses were delayed for 4, 19 and 5 years. The arteriogram, therefore, is vital toward diagnosing the disease, as the symptoms are less definitive than the confirmed presence of moyamoya vessels.

1.4 - Pathophysiological Factors of Moyamoya

The etiology of moyamoya distinguishes itself from other cerebrovascular diseases and specifically targets flow that is provided by the Circle of Willis. Cerebral blood supply relies upon the circuit of flow provided by the Circle of Willis that is supplied by the ICA. The subsequent flow in the Anterior Cerebral and Middle Cerebral Arteries (ACA and MCA, respectively) branches off into the white matter. The smaller vessels that branch off of the MCA and ACA are typically where the moyamoya collateralization will transpire. Stenosis will occur typically in the distal internal carotid artery and often involves the proximal anterior and middle cerebral arteries but can also involve posterior circulation, including the basilar and posterior cerebral arteries (Scott and Smith, 2009). The onset of stenosis, however, is notably different from atherosclerosis or arteriosclerosis. The reduced interior lumen of affected vessels, such as the middle cerebral artery (MCA), in moyamoya displays migration of smooth muscle cells from the media to demonstrate hyperplasia in the intima, which lacks macrophage infiltration and lipid deposits (Fukui *et al.*, 2000). Mural thrombi are also frequently found in stenotic lesions (Yamashita *et al.*, 1984).

Figure 1.4.1: Pathological and Histopathological Findings in Moyamoya

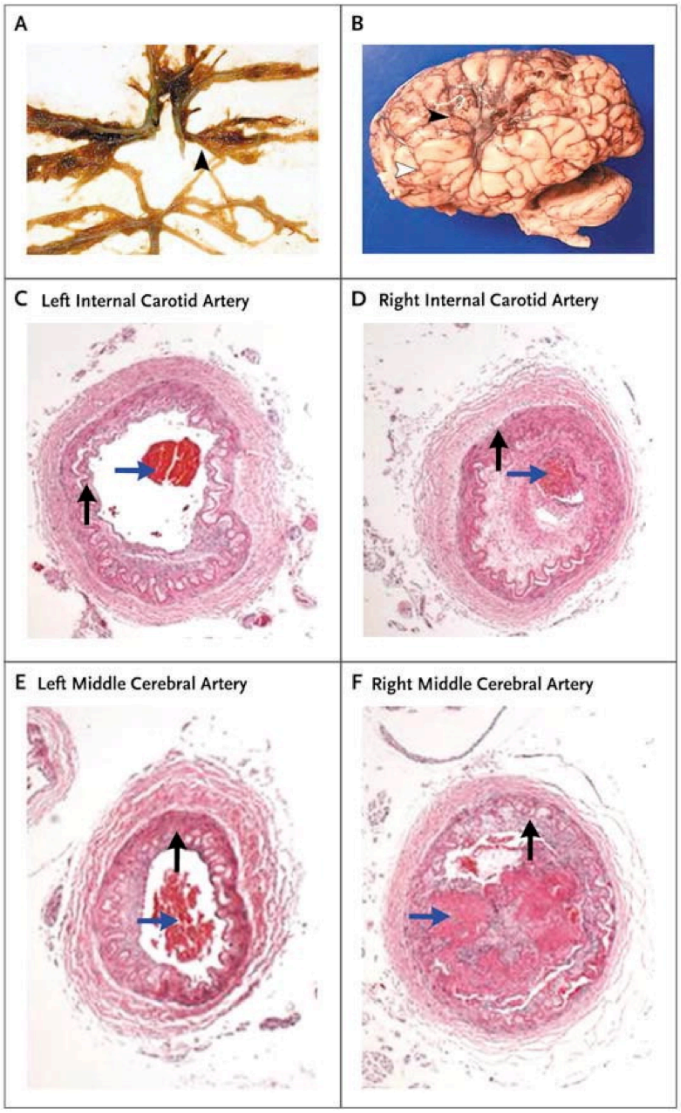

Scott RM, Smith ER.
***N Engl J Med* 2009;360:1226-1237.**

A pathological presentation of moyamoya. In panel A, stenosis is present in both of the middle cerebral arteries but notably higher illustrated by the black arrow. The white arrow in Panel B shows an acute infarct that is present with a chronic infarct, as indicated by the black arrow. Panels C-F show deterioration of the arterial wall and intraluminal thrombi (black and blue arrows, respectively). The loss of elasticity in the medial wall that is highlighted by black arrows accounts for the loss of arterial compliance. In addition to luminal thrombi, hyperplasia from smooth muscle cells drives occlusion in these main arteries.

Figure 1.4.1 displays MCA stenosis in Panel A and its resulting infarct in Panel B, while black arrows highlight medial thinning in Panels C-F with intraluminal thrombi shown with blue arrows. MCA specimens from moyamoya patients revealed thinner media than control specimens that had immunoreactivity to both cleaved caspase-3 in the medial smooth muscle cells and hypoxia-inducing factor 1 α (HIF-1 α) in the intima, hence suggesting apoptosis in the medial wall and hypoxic onset in the endothelium (Takagi *et al.*, 2006; Takagi *et al.*, 2007a; Takagi *et al.*, 2007b). Increased matrix metalloproteinase (MMP) levels in response to ischemic stroke and hemorrhage from the unstable collateral vessels have been noted in moyamoya disease (Rosell *et al.*, 2008; Fujimura *et al.*, 2009). The extracranial-intracranial bypass surgeries performed to restore ICA flow in moyamoya patients demonstrates the fragility of the network of collateral flow. The increase in pressure from the revascularization can leave patients vulnerable to hemorrhaging. MMP-9 inhibition with minocycline proved useful in postoperative management of cerebral hyperperfusion in moyamoya disease patients (Fujimura *et al.*, 2014a). The progression of the moyamoya vasculopathy is an example of dynamic vascular remodeling on account of prolific yet variable MMP activity.

Figure 1.4.2 illustrates both the anatomy of cerebral blood flow in Panel A and its reach into white matter in Panel B; Panel C illustrates how the zones with long arteries that transition into the arteriolar space are rich with glial cells and astrocytes and form the foundation for the blood-brain barrier (Iadecola, 2013). These smaller vessels will augment their presence in response to stenosis in the Circle of Willis to provide additional blood flow but are fragile and have limited flow.

Figure 1.4.2: Arterial Supply in the Brain

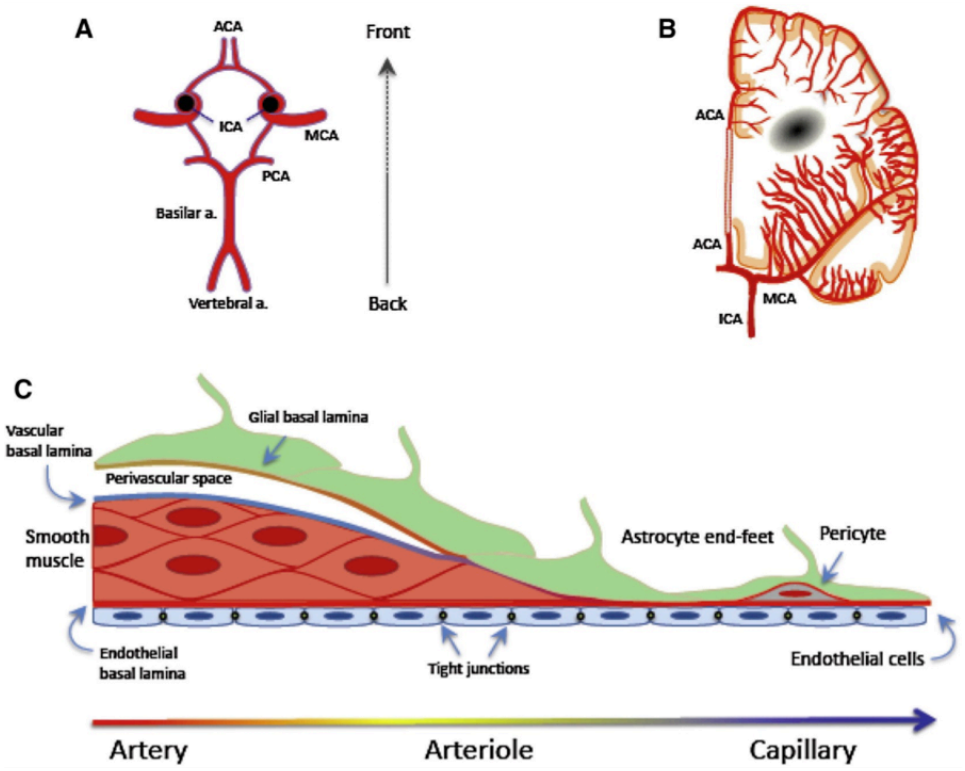

Iadecola C. *Neuron*. 2013 Nov 20;80(4):844-66.

Arterial supply into the human brain. Panel A shows the Circle of Willis and its components that provide arterial flow. It is also these same arterial structures that bear vulnerability to stenosis in moyamoya. Panel B illustrates the arterial flow in deep white matter that is provided by the anterior and middle cerebral arteries. When critical arteries encounter stenosis, moyamoya vessels will stem off of the anterior and middle cerebral arteries and restrict flow in white matter. Autoregulatory responses in white matter are compromised in healthy white matter, hence causing deep white matter to be vulnerable to hypoxia with restricted flow. Panel C shows the end of the arterial zone rich with glial cells and astrocytes that form the foundation for the blood-brain barrier.

Within 30 minutes of MCA occlusion, cerebral white matter itself is susceptible to notable swelling of both oligodendrocytes and astrocytes, whereas astrocytic swelling persists with vacuole formation and pallor of white matter with axonal swelling after 24 hours (Pantoni *et al.*, 1996). Histopathological confirmation of vulnerability to ischemia

in oligodendrocytes and myelinated axons was evident from rarefaction, or thinning, and glial formation (Pantoni and Garcia, 1997). Observable signs of moyamoya seen as hyperintensities on T2-weighted and diffusion weighted MRI scans are white matter lesions known as leukoaraiosis. Leukoaraiosis is an artifact of ischemic damage and exhibits rarefaction of white matter. These lesions display inflammation associated with cytokine-mediated processes from astrocytes that direct angiogenesis and breakdown of the blood-brain barrier.

1.5 - Genetic Susceptibility of Moyamoya

Moyamoya has a low rate of occurrence. In the United States alone, the incidence rate of moyamoya disease is 0.0001%, and the number of in-patient admissions for moyamoya vasculopathy between 1988 and 2004 was 2247 for ICD-9-CM code 437.5 (Uchino *et al.*, 2005; Lee and Liebeskind, 2011). The annual prevalence and incidence rate in Japan for moyamoya disease is 10.5 and 0.94 per 100,000 people, respectively (Kuroda and Houkin, 2008). In Korea, the incidence rate of moyamoya rose from 5.2 to 9.0 in 100,000 between 2004 and 2008, whereas the female to male ratio was 1.8 in 2011 (Im *et al.*, 2012; Ahn *et al.*, 2014). The higher incidence in Asian populations justified moyamoya as a heritable risk. Genome wide analysis confirmed that RNF213 as the susceptibility gene for moyamoya on account of its influence for angiogenesis and its expression in blood cells and splenocytes (Kamada *et al.*, 2011; Liu *et al.*, 2011).

The influence of RNF213 on the prognosis of moyamoya is reliant upon the single nucleotide polymorphism of the gene. Sequencing of the RNF213 gene revealed genetic variants with different outcomes. The c.14429G>A (p.R4810K) polymorphism, or mysterin, demonstrated a higher incidence in patients with moyamoya disease than

healthy controls, a familial history and a propensity for cerebral infarction at diagnosis with a poor prognosis (Kim *et al.*, 2016). In comparison with healthy controls, mysterin is also elevated in patients with moyamoya syndrome and coexists with autoimmune disease, Down's syndrome, hyperthyroidism and neurofibromatosis (Morimoto *et al.*, 2016). Despite the vulnerability for cerebral hypoxia, overexpression of mysterin in endothelial cells suppressed moyamoya vessel formation in the absence of interferon-β, which was not seen in RNF213 wild-type animals (Kobayashi *et al.*, 2015). Hence, the impact of RNF213 on moyamoya relies on the polymorphism of the gene, yet the gene is interestingly pertinent to ischemia itself.

RNF213 in itself has not been characterized as essential for the development of moyamoya. Transient models of ischemia in RNF213 knockouts and wild-type animals demonstrated no significant differences in intimal or medial thickness of the common carotid artery (CCA) at 7, 21 and 28 days after CCA ligation; the Circle of Willis and leptomeningeal spaces also had no visual differences between the two groups (Sonobe *et al.*, 2014). RNF213 deficient mice developed enhanced vessels in an ischemic model with lower MMP-9 expression (Ito *et al.*, 2015). Upregulation of RNF213 in animal models of transient ischemia, though, occurred in neurons as soon as six hours after reperfusion (Sato-Maeda *et al.*, 2016). It is suggested from these studies, therefore, that RNF213 requires additional stimulus to engender moyamoya vasculopathy.

The inflammatory nature of brains in moyamoya patients is indisputable. The role of inflammation, however, is less clear. The enhanced expression of matrix metalloproteinases and angiogenic factors, such as VEGF, with RNF213 support the inflammatory guided role in angiogenesis rather than tissue damage (Fujimura *et al.*,

2014b). Yet, pro-inflammatory cytokines TNF-α and IFN-γ synergistically increase RNF213 expression (Ohkubo *et al.*, 2015). Therefore, the type and source of stimulus is necessary to evaluate to appropriately gauge which impact inflammation will have in moyamoya.

IFN-γ in particular is presented by T cells and overexpressed in autoimmune conditions. IFN-γ is elevated in T cells for autoimmune conditions of the thyroid and enables lymphocyte recognition of vascular endothelial cells (Pober *et al.*, 1983; Karanikas *et al.*, 2005). Reports of elevated thyroid autoantibodies in both adult and pediatric patients with moyamoya disease suggest that enhanced inflammation from autoimmune conditions can interact with the pathophysiologic onset of the disease (Kim *et al.*, 2010; Li *et al.*, 2011). Intracranial stenosis in large arteries also demonstrated elevated thyroid autoantibody levels (Shi *et al.*, 2014). IFN-γ also has been found to suppress remyelination in models of experimental autoimmune encephalomyelitis (Lin *et al.*, 2006). The conspicuous presence of elevated IFN-γ and other cytokines in moyamoya, therefore, suggests that forthcoming microstructural changes are consequences of the inflammatory environment that involve T cell signaling.

1.6 - SULT1E1 and Inflammation in Vascular Disease

Elevated cytokines stimulate growth factors that mediate both the angiogenic and mitogenic changes in Moyamoya disease. When compared to normal patients, elevated levels of IL-1β, MCP-1, basic Fibroblast Growth Factor (FGF-2), Vascular Endothelial Growth Factor (VEGF), Platelet Derived Growth Factor (PDGF) and MMPs have been detected in the cerebrospinal fluid of Moyamoya patients (Kang *et al.*, 2010). In addition to the stimulus from cytokines on growth factors that influence cell proliferation,

heightened MMP activity is capable of causing breakdown of the blood-brain barrier and intimal hyperplasia. In another study, myometrial microvascular endothelial cells stimulated with VEGF demonstrated upregulation of a metabolic enzyme for estrogens known as estrogen sulfotransferase, or SULT1E1 (Weston *et al.*, 2002). Hence, the elevated cytokines and growth factors, such as VEGF, support the possibility of heightened estrogen metabolism in moyamoya, as estrogen counteracts inflammatory stimuli.

Estrogen Sulfotransferase (SULT1E1) is a regulatory enzyme for the metabolism of estrogen. It belongs to a class of enzymes known as sulfotransferases that are found within the thyroid, intestine, liver, breast, blood, brain, lungs, kidneys and adrenal glands (Falany, 1997; Miki *et al.*, 2002) Specifically, SULT1E1 will render estrone or estradiol inactive by sulfating it, hence disabling the hormone from binding with its receptor and preparing the hormone for excretion through the biliary and urinary routes. Figure 1.6 illustrates metabolic pathways for steroid hormones and how Steroid Sulfatase (STS) can counteract SULT1E1 through desulfation, thereby enabling STS and SULT1E1 to facilitate equilibrium for estradiol utilization and metabolism (Kirk *et al.*, 2001). In both prostate and breast cancer, for example, STS and SULT1E1 expression is confirmed, and the presence of SULT1E1 demonstrates a reduced risk of recurrence and better prognosis in the in the latter (Suzuki *et al.*, 2003; Nakamura *et al.*, 2006). Hence, STS and SULT1E1 can serve as indications of pathologic risk in diseases with tissue where estrogen metabolism is active.

Figure 1.6: Synthetic and Metabolic Pathways for Steroidal Hormones

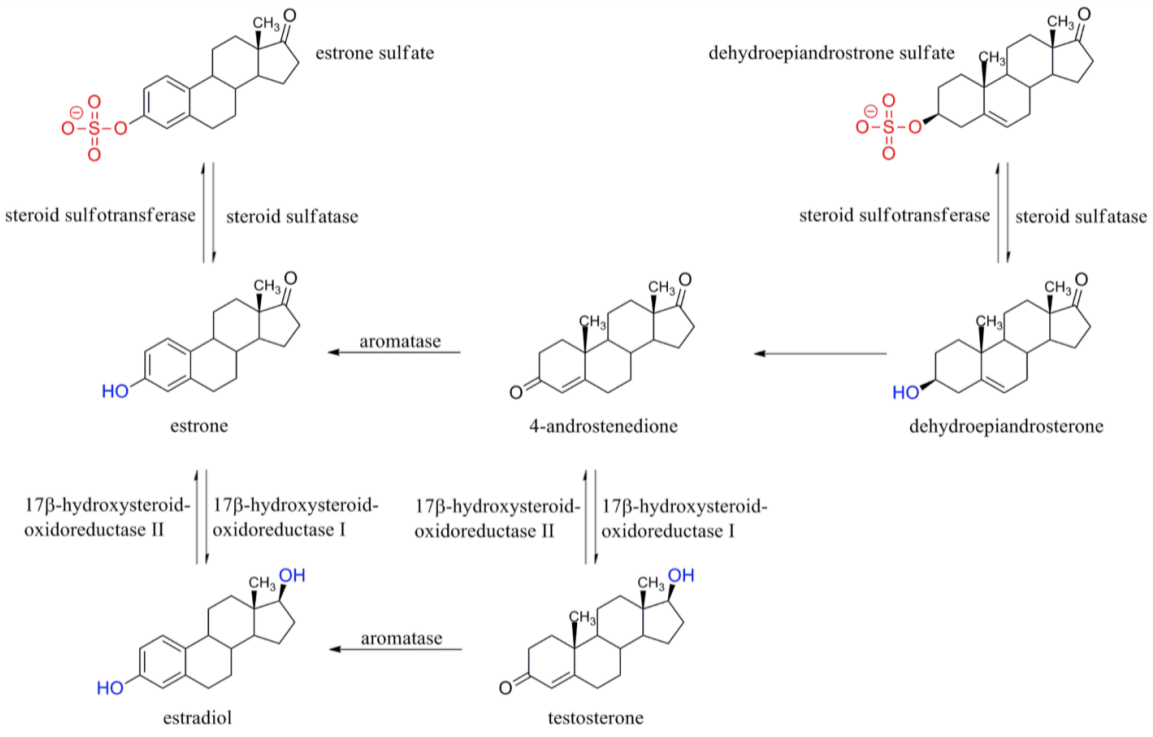

Adapted from Kirk CJ, *et al*. *Biochem Soc Tran*, 2001 May; 29 (Pt2): 209-216.

An overview of synthetic and metabolic pathways for steroidal hormones. Sulfation of steroids by sulfotransferases is common in both androgens and estrogens, as seen with estrone sulfate and dehydroepiandrostone sulfate. Sulfatase activity is common to both steroidal paths, as the red sulfate groups are replaced with hydroxyl substituents. Additionally, 17βhydroxysteroid-oxidoreductase I and II enable reduction and oxidation, respectively, for both androgens and estrogens. Irreversible processes are featured in the production of 4-androstenedione by 3β hydroxysteroid-dehydrogenase and the conversion of androgens into estrogens by aromatase.

The balance between STS and SULT1E1 is important for diseases that involve cell proliferation in vascular diseases. Both estradiol production from circulating androgens and estradiol metabolism fluctuate with the stage of atherosclerosis. Aromatase expression detected in the atherosclerotic lesions of the aorta from female patients was significantly higher than in those of male patients, thus emphasizing the prominence of estradiol conversion from androgens (Murakami *et al.*, 2001). Aortic

VSMCs from female patients with advanced atherosclerosis and male patients had markedly higher SULT1E1 levels than in VSMCs of female patients with milder atherosclerotic progression (Nakamura *et al.*, 2005). Nakamura and colleagues also discovered the density of neointimal Estrogen Receptor α and β (ERα and ERβ, respectively) in females with milder changes was double that of severe female atherosclerotic patients, who had elevated STS. Albeit complex, the role of estrogen metabolism in cell proliferation varies with the stage of disease in a dynamic fashion.

2-(4'-[^{11}C]methylaminophenyl)-6-hydroxybenzothiazole, also known as Pittsburgh Compound B or [^{11}C]-PiB, is a substrate for SULT1E1 with a reported K_m of 1.42±0.12 μM and has produced signal in Positron Emission Tomography (PET) scanning of a rat model, whose brain homogenates had confirmed sulfation of the tracer trapped in the tissue (Cole *et al.*, 2010). Consequently, [^{11}C]-PiB is capable of imaging diseases where the activity of SULT1E1 is associated with pathophysiological changes. ICA stenosis gives rise to hemodynamic instability in moyamoya that can cause inadequate collateral flow. The intricate collateralization is deep within white matter and capable of inflicting subcortical damage in addition to generating zones where cerebral flow is jeopardized. Inevitably, these regions exhibiting pathophysiological characteristics of Moyamoya will be influenced by inflammation. Elevated cytokines in moyamoya can induce growth factors, MMP activity and stimulate SULT1E1 activity, which should vary with the progression of cerebrovascular disease. The purpose of this study is to use [^{11}C]-PiB to image inflammation in disease that lacks Aß to validate SULT1E1 as a target.

1.7 - Pittsburgh Compound B ([^{11}C]-PiB)

Figure 1.7.1: Beta Amyloid (Aß) Imaging Probes for PET

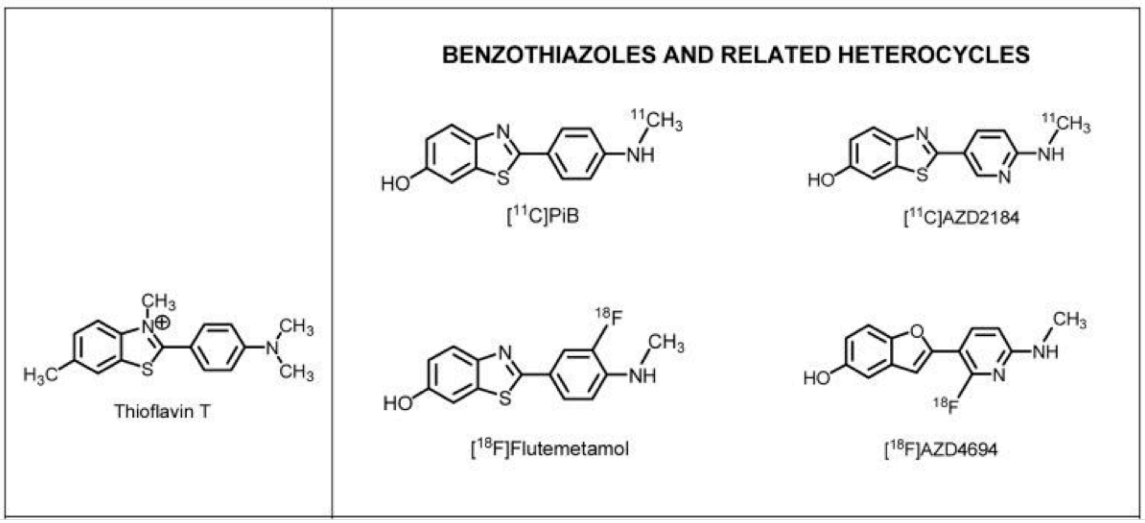

Adapted from Kepe V, *et al. J Alzheimers Dis*. 2013 Jan 1; 36(4): 613–631.

Imaging probes for beta amyloid (Aß) utilized with Positron Emission Tomography (PET). Benzothiazoles are heterocyclic candidates for radiolabeled tracers that are derivatives of Thioflavin T. Thioflavin T is a charged dye used to stain Aß fibrils. Unlike Thioflavin T, the radiolabeled benzathiazoles are both uncharged and lipophilic. [^{11}C]-PiB and [^{18}F]-Flutemetamol are confirmed substrates for SULT1E1 on account of the phenolic substituents found in these molecules.

Imaging beta amyloid (Aß) with radiolabeled probes requires a hydrophobic molecule that can easily cross the blood brain barrier. Researchers at the University of Pittsburgh developed [^{11}C]-PiB to image beta amyloid (Aß) plaques by radiolabeling molecules known as benzothiazoles. Figure 1.7.1 features several benzothiazole tracers presently in use for imaging Aß with PET. These heterocyclic molecules are derivatives of Thioflavin T, which is a dye that binds to Aß fibrils. When bound to Aß fibrils, Thioflavin T has a strong fluorescent signal (Biancalana and Koide, 2010). Thioflavin T, however, bears a charge that makes it ineligible to cross the blood brain barrier. Klunk

and Mathis, therefore, used benzothiazoles since they are both hydrophobic and uncharged molecules with an affinity for Aß (Klunk *et al.*, 2001).

Figure 1.7.2: Range of [^{11}C]-PiB Signal in Alzheimer's Disease

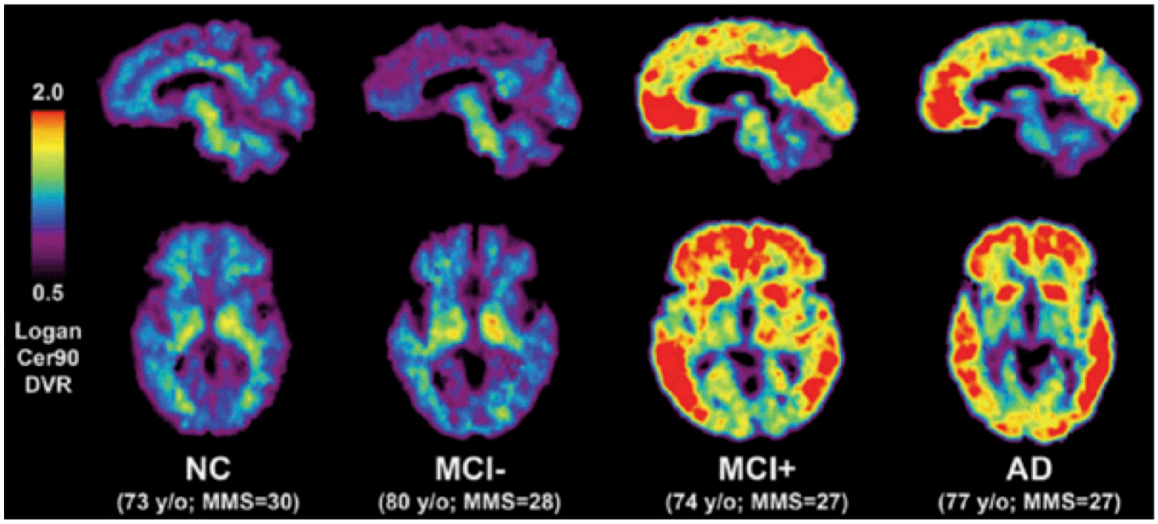

Kaj Blennow & Henrik Zetterberg. *Nature Medicine* - 12, 753 - 754 (2006).

The range of [^{11}C]-PiB signal in the diagnosis of Alzheimer's Disease (AD). Here signal from parametric images represented represent accumulation of the tracer after a dynamic scan that is normalized to uptake in the cerebellar grey matter. [^{11}C]-PiB signal in cortical tissue becomes progressively stronger as the disease advances through mild cognitive impairment (MCI) and AD. The mini-mental state exam scores also show decline with increasing [^{11}C]-PiB signal. The [^{11}C]-PiB signal in MCI- and MCI+ differs on account of the presence of dense Aß.

[^{11}C]-PiB produced a strong signal corresponding to affected cortical regions. In its first report, patients with Alzheimer's Disease (AD) showed strong [^{11}C]-PiB cortical binding that was inversely correlated with glucose metabolism established with [^{18}F]-FDG (Klunk *et al.*, 2004). Post-mortem validation of [^{11}C]-PiB signal demonstrated Aß colocalization with dense uptake that was notably high in the frontal cortex (Ikonomovic *et al.*, 2008). Figure 1.7.2 summarizes results from the Pittsburgh group to show increasing [^{11}C]-PiB accumulation with advancing stages of AD (Blennow and

Zetterberg, 2006). This figure, however, illustrates, how patients in the Mild Cognitive Impairment (MCI) stage may have vastly different signal. Here the +/- designation is intended to show how the presence of heavy Aß produces a [^{11}C]-PiB signal different in patients lacking Aß. Ultimately, patients to be imaged with [^{11}C]-PiB were classified as either [^{11}C]-PiB positive or negative, with [^{11}C]-PiB positive defined as a global cortical [^{11}C]-PiB uptake to cerebellar uptake ratio of 1.5 or higher (Jack *et al.*, 2008). Evaluation of a [^{11}C]-PiB negative case showed diffuse focal Aß clusters versus dense Aß in a [^{11}C]-PiB positive case (Ikonomovic *et al.*, 2012). Despite confirmation of Aß in both cases, the [^{11}C]-PiB negative case in this study diagnosed with dementia with Lewy bodies was substantially lower than the [^{11}C]-PiB positive case (Figure 1.7.3).

Figure 1.7.3: [^{11}C]-PiB Negative versus [^{11}C]-PiB Positive Scan

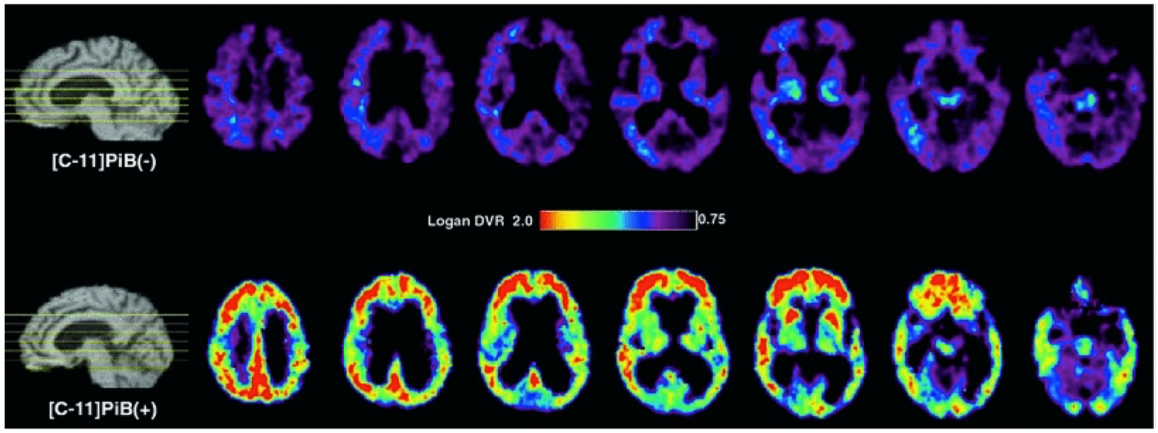

Ikonomovic MD, *et al*. *Acta Neuropathol* (2012) 123: 433.

Comparison of [^{11}C]-PiB signal between dementia with Lewy bodies and a patient with probable AD designated as [^{11}C]-PiB negative and positive, respectively. The [^{11}C]-PiB negative case had much lower signal than the [^{11}C]-PiB positive case despite confirmation of Aß both patients. The [^{11}C]-PiB negative case had produced diffuse focal Aß clusters, whereas the [^{11}C]-PiB positive case had dense Aß plaques.

Reports of confounding cases with [^{11}C]-PiB has cast doubt on the fidelity of the tracer's specificity for Aß. In a study that validated postmortem tissue from patients

imaged with [^{11}C]-PiB, one [^{11}C]-PiB negative patient produced dense Aß staining in the frontal cortex (Leinonen *et al.*, 2008). Another case disclosed a [^{11}C]-PiB negative scan in a patient who demonstrated declining memory, Aß and tau in CSF and dense Aß postmortem staining (Cairns *et al.*, 2009). [^{11}C]-PiB signal in patients with AD type dementia matched four of 41 non-demented patients, two of which were indistinguishable from the demented patients (Mintun *et al.*, 2006). Authors of these studies and the Pittsburgh group have indicated that these aberrations may be a consequence of different types of amyloid, for which [^{11}C]-PiB lacks an affinity. [^{11}C]-PiB, however, has failed to produce reliable in-vivo testing that could substantiate this hypothesis.

[^{11}C]-PiB has encountered problems imaging transgenic mouse models that produce Aß abundantly. The PS-1/APP (presenilin-1/amyloid precursor protein) transgenic mouse model yielded scarce [^{11}C]-PiB uptake despite Aß deposition higher than seen in AD (Klunk *et al.*, 2005). In another study, [^{11}C]-PiB uptake in wild mice exceeded that in transgenic mice with dense cortical deposition of Aß on account of reduced cerebral blood flow (Toyama *et al.*, 2005). Additional investigation of suppressed [^{11}C]-PiB uptake in transgenic mouse models concluded the following: ex-vivo autoradiography is best at later time points beyond 16 months and Aß from PS-1/APP mice lacks AßN3-pyroglutamate and PiB binding sites necessary for a model of amyloidosis (Maeda *et al.*, 2007). First, reduced cerebral blood flow is a condition to be anticipated in an aging brain, which would contradict signal witnessed in geriatric [^{11}C]-PiB positive patients. Second, the PS-1/APP model expresses genes associated with early deposition of transgenic human Aß deposits in the cerebral cortex and hippocampus to produce a model of Alzheimer's pathology (Holcomb *et al.*, 1998). Hence, the in-vivo

studies have contributed dubious insight concerning the reliability of [^{11}C]-PiB imaging Aß with fidelity.

Additional complications raise questions about [^{11}C]-PiB that question its ability to target Aß well on account of white matter uptake. Albeit lower than cortical tissue, [^{11}C]-PiB has an undeniable signal in white matter that is higher in healthy controls yet attributed to slower clearance (Fodero-Tavoletti *et al.*, 2009). Arterial transit time of white matter, however, is longer than in cortical tissue, and an aged brain with disease may exhibit even longer transit times (Liu *et al.*, 2012). The white matter signal, therefore, is conspicuous, as longer transit times would suggest higher signal than in cortical tissue. In an aging brain, longer transit times would suggest an even higher white matter signal. Partial volume effects in the Alzheimer's brain also support the notion of [^{11}C]-PiB spillover between the cortical tissue and white matter in both directions (Moghbel *et al.*, 2012). Hence, [^{11}C]-PiB imaging of white matter raises concern about the ability to image Aß reliably.

[^{11}C]-PiB imaging has patterns that are not characteristic with AD pathology in the medial temporal lobe. The medial temporal lobe includes, the hippocampus, the middle frontal gyrus, superior and middle temporal gyri, entorhinal cortex and amygdala. Amyloid and neurofibrillary tangle deposition in these regions have distinct association with Clinical Dementia Rating (Thal *et al.*, 2000; Thal *et al.*, 2002). [^{11}C]-PiB signal in the medial temporal, however, is virtually absent (Kepe *et al.*, 2013). Therefore, the deficit of [^{11}C]-PiB uptake in the medial temporal lobe presents question as to whether the compound is Aß specific since dense Aß exists there in AD.

The aforementioned complications encountered while imaging Aß with [^{11}C]-PiB dilute confidence in the tracer as an amyloid-imaging probe. What presents additional inconsistency, however, is [^{11}C]-PiB imaging in meningioma. Meningioma is a common brain tumor in adults that forms in the meninges, which are membranes that encapsulate the brain and spinal cord. Tumor proliferation in meningiomas engages in inflammatory signaling. Upregulation of cyclooxygenase-2 (COX-2) and subsequent enhanced prostaglandin synthesis from arachidonic acid provide pro-inflammatory stimuli for tumorigenesis (Ragel *et al.*, 2005). COX-2 inhibitors, such as non-steroidal anti-inflammatory drugs, suppress prostaglandin synthesis and abate proliferative effects (Ragel *et al.*, 2007). Several reports confirmed [^{11}C]-PiB uptake in meningiomas, particularly in subjects with mild or no dementia. Yet, what is of importance is that meningioma lacks Aß (Johnson *et al.*, 2012). Figure 1.7.4 illustrates one report that compared [^{11}C]-PiB uptake in metastatic melanoma on the left with [^{11}C]-PiB uptake in meningioma on the right (Bengel and Minoshima, 2012). Unlike the meningioma, the melanoma metastasis failed to demonstrate [^{11}C]-PiB uptake, hence suggesting that [^{11}C]-PiB uptake colocalizes with increased inflammation.

Figure 1.7.4: Select [^{11}C]-PiB Uptake in Brain Tumors

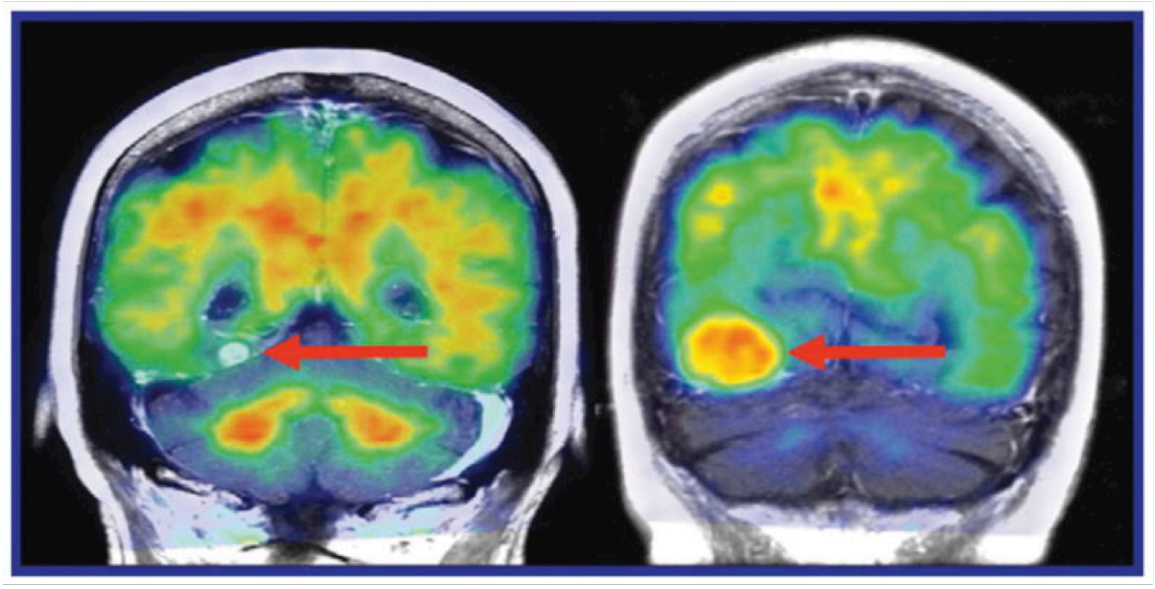

Bengel FM, Minoshima S. *JNM* 2012; 53(9): 15N-31N.

[^{11}C]-PiB scans from two different patients with confirmed brain tumors. The left patient has metastatic melanoma highlighted by the red arrow; the right patient has a meningioma. Despite uptake within the patient on the left, [^{11}C]-PiB retention is not within the melanoma metastasis but clearly in the meningioma. Contrary to the [^{11}C]-PiB uptake, meningiomas lack Aß expression and overexpress COX-2, which causes increased prostaglandin synthesis.

The [^{11}C]-PiB results documented in meningioma corroborates the concept of the tracer demonstrating a capacity for high signal in inflammatory diseases that lack Aß. Consequently, elevated activity from SULT1E1 should reflect increased estrogen metabolism in response to inflammatory signaling. In this study, [^{11}C]-PiB signal is evaluated in a non-hemorrhagic model of stroke, a cohort of moyamoya syndrome patients and a multiple sclerosis patient receiving immunomodulatory therapy. Each assessment lacks Aß but entails massive inflammatory signaling, which should reflect in both SULT1E1 expression and [^{11}C]-PiB signal.

Chapter Two: Materials and Methods

2.1 - Radiochemistry and Preparation Of 6-Hydroxy-2-(4'-{[^{11}C] Methylamino}Phenyl) Benzathiazole ([^{11}C]PiB)

Figure 2.1.1: Scheme 1

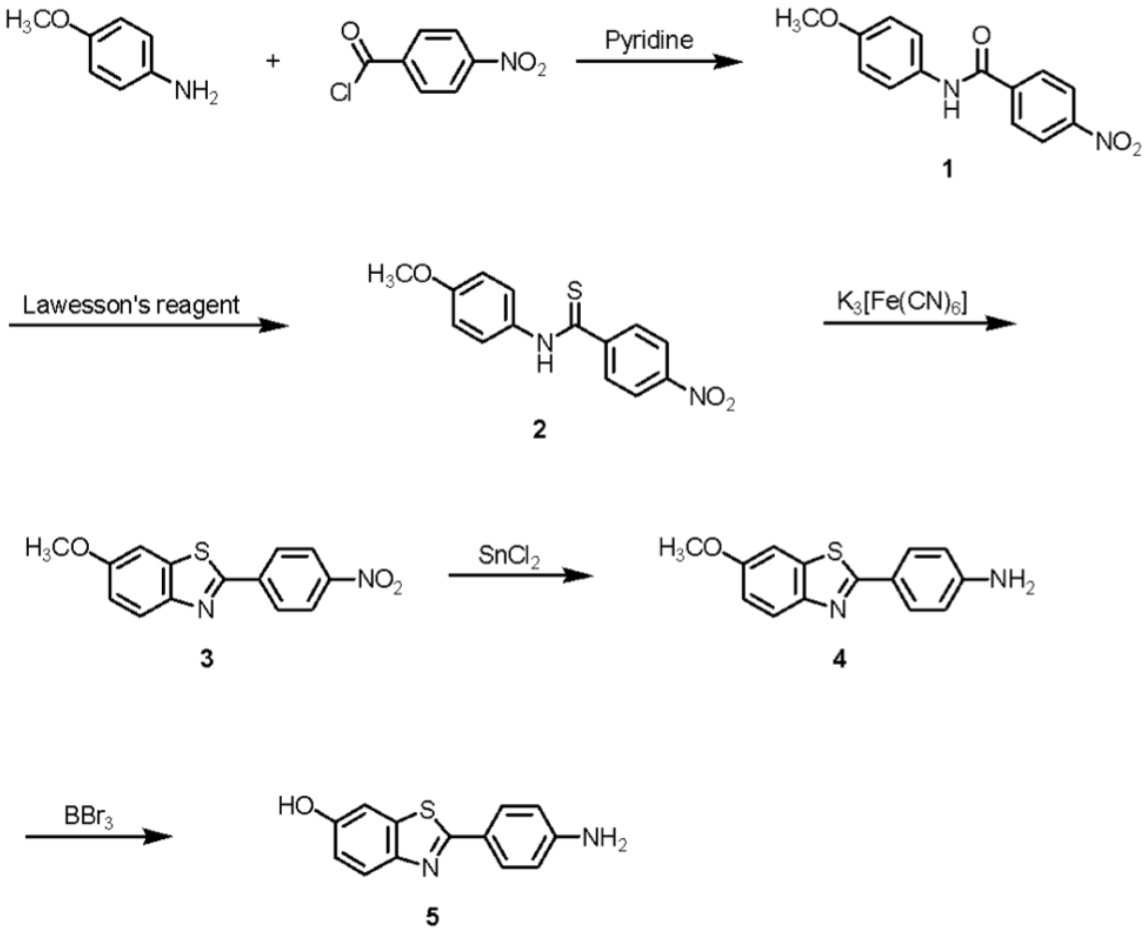

Scheme 1

*Preparation of the precursor 2-(4'-aminophenyl)-6-hydroxybenzothiazole (**5**). Conversion of N-(4'-methoxyphenyl)-4-nitrobenzamide (**1**), prepared by condensing p-anisidine with 4-nitrobenzoyl chloride in pyridine medium, to the corresponding thiobenzamide **2** transpired by a reaction with Lawesson's reagent in chlorobenzene. Compound **2** reacted with potassium ferricyanide in the presence of sodium hydroxide in ethanol to yield 6-methoxy-2-(4'-nitrophenyl)benzothiazole (**3**), which tin (II) chloride reduced in the next step to 2-(4'-aminophenyl)-6-methoxybenzothiazole (**4**). Demethylation with boron tribromide in dichloromethane of the derivative **4** yielded 2-(4'-aminophenyl)-6-hydroxybenzothiazole (**5**), the precursor for preparation of 6-hydroxy-(4'-{[^{11}C] methylamino}phenyl)benzothiazole ([^{11}C]PiB).*

Preparation of 2-(4'-Aminophenyl)-6-hydroxybenzothiazole (5)

(Precursor for the preparation of [^{11}C]PiB)

Precursor 2-(4'-aminophenyl)-6-hydroxybenzothiazole (**5**) was prepared as described in the literature and is depicted accordingly in Figure 2.1.1: Scheme 1 above (Mathis *et al.,* 2003). Briefly, *N*-(4'-methoxyphenyl)-4-nitrobenzamide (**1**), prepared by condensing p-anisidine with 4-nitrobenzoyl chloride in pyridine medium, was converted to the corresponding thiobenzamide **2** by a reaction with Lawesson's reagent in chlorobenzene. The reaction of compound **2** with potassium ferricyanide in the presence of sodium hydroxide in ethanol yielded 6-methoxy-2-(4'-nitrophenyl)benzothiazole (**3**) which was reduced in the next step to 2-(4'-aminophenyl)-6-methoxybenzothiazole (**4**) with tin (II) chloride. Demethylation of the derivative **4** with boron tribromide in dichloromethane yielded 2-(4'-aminophenyl)-6-hydroxybenzothiazole (**5**), the precursor for preparation of 6-hydroxy-(4'-{[^{11}C] methylamino}phenyl)benzothiazole ([^{11}C]PiB).

***N*-(4'-Methoxyphenyl)-4-nitrobenzamide (1).**

To a solution of 4-methoxyaniline (12.3 g, 0.1 mmol) in pyridine (150 mL) was added 4-nitrobenzoyl chloride (18.5 g, 0.1 mmol). The reaction mixture was heated to reflux for 2 h. Upon cooling to room temperature, the reaction was quenched with water. The precipitate that formed was filtered and was washed with 5% sodium bicarbonate solution and water and then dried at room temperature to give 20.0 g (74%) of *N*-(4'-methoxyphenyl)-4-nitrobenzamide. ^{1}H NMR (300 MHz, DMSO-d_6) δ: 10.47 (s, 1 H, NH), 8.37 (d, J = 8.5 Hz, 2 H), 8.18 (d, J = 8.4 Hz, 2 H), 7.69 (d, J = 8.6 Hz, 2 H), 6.96 (d, J = 8.4 Hz, 2 H), 3.77 (s, 3 H).

***N*-(4'-Methoxyphenyl)-4-nitrothiobenzamide (2).**

To a solution of *N*-(4'-methoxyphenyl)-4-nitrobenzamide (**1**) (20.0 g, 73.5 mmol) in chlorobenzene (50 mL) was added Lawesson's reagent (17.8 g, 44 mmol). The reaction mixture was heated to reflux for 3 h. Upon cooling, the product slowly precipitated out from the reaction mixture and was filtered and recrystallized from methanol to give 13.6 g (64%) of the product **2**. ^{1}H NMR (300 MHz, DMSO-d_6) δ: 8.29 (d, J = 8.5 Hz, 2 H), 8.00 (d, J = 8.4 Hz, 2 H), 7.76 (d, J = 8.6 Hz, 2 H), 7.03 (d, J = 8.4 Hz, 2 H), 3.80 (s, 3 H, OCH_3).

6-Methoxy-2-(4'-nitrophenyl)benzothiazole (3).

N-(4'-Methoxyphenyl)-4-nitrothiobenzamide (**2**) (13.6 g, 47.2 mmol) was first wetted with ethanol (~2 mL), and 30% aqueous sodium hydroxide solution (15 g, 0.38 mol) was added. The mixture was diluted with water to provide a final suspension in 10% aqueous sodium hydroxide. Aliquots of this mixture were added at 1 min intervals to a stirred solution of potassium ferricyanide (62 g, 0.19 mol) in water (200 mL) at 80-90° C. The reaction mixture was heated for a further period of 30 min and then allowed to cool to room temperature. The precipitate was filtered and washed with water to give 12.5 g of crude product, which was used in next step without further purification. ^{1}H NMR (300 MHz, acetone-d_6) δ: 8.36 (m, 4 H), 7.08 (d, J = 8.5 Hz, 1 H), 7.61 (s, 1 H), 7.13 (d, J = 8.5 Hz, 1H), 3.93 (s, 3 H).

2-(4'-Aminophenyl)-6-methoxybenzothiazole (4).

To a solution of 6-methoxy-2-(4'-nitrophenyl)benzothiazole (**3**) (22 mg, 0.077 mmol) in ethanol (10 mL) was added tin(II) chloride dehydrate (132 mg, 0.45 mmol). The reaction mixture was refluxed under nitrogen for 4 h. Ethanol was then evaporated and the residue was dissolved in ethyl acetate (10 mL). The resulting solution was washed with 1 *N* sodium hydroxide (2 mL) followed by water (5 mL) and dried over $MgSO_4$. Evaporation of the solvent gave 19 mg (97%) of the product as a yellow solid. ^{1}H NMR (300 MHz, $CDCl_3$) δ: 7.85 (d, J = 8.7 Hz, 2 H), 7.75 (dd, J_1 = 8.8 Hz, J_2 = 1.3 Hz, 1 H), 7.31 (d, J = 2.4 Hz, 1 H), 7.03 (dd, J_1 = 8.8 Hz, J_2 = 2.4 Hz, 1 H), 6.56 (d, J = 7.6 Hz, 2 H), 3.84 (s, 3 H).

2-(4'-Aminophenyl)-6-hydroxybenzothiazole (5).

To a suspension of 2-(4'-aminophenyl)-6-methoxybenzothiazole (**4**) (500 mg, 1.95 mmol) in dichloromethane (20 mL) was BBr_3 (1*M* in dichloromethane, 5 mL, 5 mmol) was added via a syringe. The reaction mixture was stirred at room temperature for 16 h and then quenched with 5% HCl. The mixture was neutralized with saturated sodium bicarbonate and extracted with ethyl acetate (6 x 50 mL). The organic layers were combined and washed with water and dried over $MgSO_4$. Evaporation of the solvent gave ~500 mg of the crude product, which was purified by flash chromatography (silica gel, hexanes:ethyl acetate = 2:1) to give 360 mg (76%) of the hydroxythiazole product **5**. ^{1}H NMR (300 MHz, acetone-d_6) δ: 7.86 (s, 1H, OH), 6.95 (d, J = 9.1 Hz, 2H), 6.91(d, J = 8.8 Hz, 1H), 6.55 (d, J = 2.5 Hz, 1 H), 6.17 (dd, J_1 = 8.8 Hz, J_2 = 2.5 Hz, 1 H), 5.95 (d, J = 9.1 Hz, 2 H), 4.45 (s, 2 H, NH_2).

Preparation of 6-Hydroxy-2-(4'-{methylamino}phenyl) benzothiazole (10) (non-radioactive PiB standard)

Non-radioactive 6-hydroxy-2-(4'-{methylamino)phenyl)benzothiazole (**10**) standard was prepared as previously described in the literature and is depicted in Scheme 2 below (Mathis *et al.*, 2003). In short, 2-amino-5-methoxythiophenol (**7**), prepared from the commercially available 6-methoxythiazole (**6**) by alkaline hydrolysis, was reacted with 4-(methylamino)benzoic acid (**8**) in polyphosphoric acid to yield 6-methoxy-2-(4'-{methylamino}phenyl)benzothiazole (**9**). The benzothiazole **9** was O-demethylated with BBr_3 in dichloromethane to yield 6-hydroxy-2-(4'-{methylamino}phenyl)benzothiazole (**10**).

2-Amino-5-methoxythiophenol (7).

6-methoxybenzothiazole (**6**) (30.0 g, 172 mmol) was suspended in 50% KOH (180 g KOH dissolved in 180 mL water) and ethylene glycol (40 mL). The suspension was heated to reflux for 48 h. Upon cooling to room temperature, toluene (300 mL) was added and the reaction mixture was neutralized with glacial acetic acid (180 mL). The organic layer was separated, and the aqueous layer was extracted with another 200 mL of toluene. The toluene layers were combined and washed with water and dried over $MgSO_4$. Evaporation of the solvent gave 15.3 g of 2-amino-5-methoxythiophenol (**7**) as a yellow solid. ^{1}H NMR (300 MHz, acetone-d_6) δ: 6.66 (d, J = 2.6 Hz, 1 H), 6.57 (d, J = 8.5 Hz, 1 H), 6.43 (dd, J_1 = 2.6 Hz, J_2 = 8.5 Hz, 1 H), 3.77 (s, 3 H).

Figure 2.1.2: Scheme 2

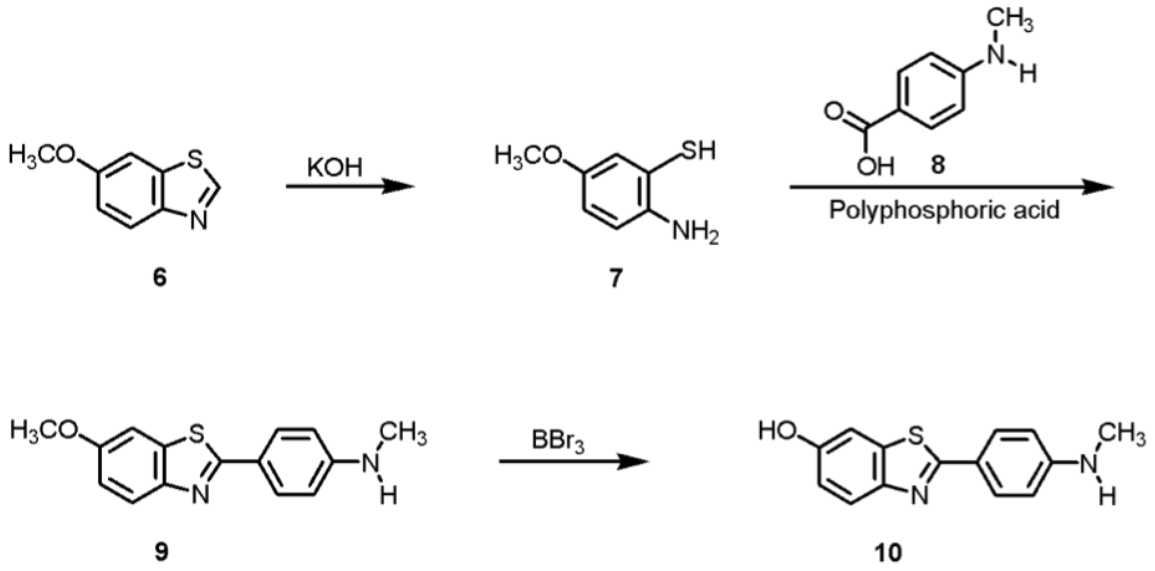

Scheme 2

*Preparation of the non-radioactive 6-hydroxy-2-(4'-{methylamino)phenyl)benzothiazole (**10**) standard. 4-(methylamino)benzoic acid (**8**) in polyphosphoric acid reacted with 2-amino-5-methoxythiophenol (**7**), prepared from the commercially available 6-methoxythiazole (**6**) by alkaline hydrolysis, to yield 6-methoxy-2-(4'-{methylamino}phenyl)benzothiazole (**9**). The O-demethylation of benzothiazole **9** with BBr_3 in dichloromethane yielded 6-hydroxy-2-(4'-{methylamino}phenyl)benzothiazole (**10**).*

6-Methoxy-2-(4'-{methylamino}phenyl)benzothiazole (9).

4-(Methylamino)benzoic acid (**8**) (11.5 g, 76.2 mmol) and 2-amino-5-methoxythiophenol (**7**) (12.5, g, 80 mmol) were mixed together with polyphosphoric acid (~30 g) and heated to 170° C under a nitrogen atmosphere for 1.5 h. The reaction mixture was cooled to room temperature and poured into 10% K_2CO_3 solution. The precipitate that formed was filtered and was first purified by recrystallization from acetone/water followed by treatment with activated charcoal in THF/water to give 4.6 g (21%) of the product **9**. ^{1}H NMR (300 MHz, acetone-d_6) δ: 7.84 (d, J = 9.0 Hz, 2 H), 7.80

(d, J = 9.0 Hz, 1 H), 7.51 (d, J = 3.0 Hz, 1 H), 7.05 (dd, J_1 = 9.0 Hz, J_2 = 3.0 Hz, 1 H), 6.70 (d, J = 9.0 Hz, 2 H), 3.88 (s, 3 H), 2.85 (d, J = 6.0, 3 H).

6-Hydroxy-2-(4'-{methylamino}phenyl)benzothiazole (10).

To a suspension of 6-methoxy-2-(4'-methylaminophenyl)benzothiazole (**9**) (3.0 g, 10.4 mmol) in dichloromethane (100 mL) BBr_3 (1*M* in dichloromethane, 35 mL, 35 mmol) was added via a syringe. The reaction mixture was stirred at room temperature for 16 h. After quenching with water, the reaction mixture was extracted with ethyl acetate (6 x 100 mL). The organic layers were combined, washed with water, and dried over $MgSO_4$. Evaporation of the solvent gave 2.5 g of the crude product, which was purified by flash chromatography (silica gel, hexanes:ethyl acetate = 1:8, followed by THF and MeOH) to give 2.1 g (75%) of 6-hydroxy-2-(4'-{methylamino}phenyl)benzothiazole (**10**). ^{1}H NMR (300 MHz, acetone-d_6) δ: 7.88 (d, J = 9.1 Hz, 2 H), 7.73 (d, J = 8.8 Hz, 1 H), 7.38 (d, J = 2.5 Hz, 1 H), 6.99 (dd, J1 = 8.8 Hz, J2 = 2.5 Hz, 1 H), 6.83 (d, J = 9.1 Hz, 2 H), 2.83 (d, J = 9.5 Hz, 3 H).

Radiosynthesis of 6-Hydroxy-2-(4'-{[^{11}C]methylamino}phenyl) bezothiozole (10) ([^{11}C]PiB)

Radiosynthesis of 6-hydroxy-2-(4'-{[^{11}C]methyalamino}phenyl)benzothiazole (**10**) ([^{11}C]PiB) was performed using the methodology described previously in the literature and is depicted in Scheme 3 below (Mathis *et al.*, 2003; Wilson, 2004; Solbach *et al.*, 2005).

Figure 2.1.3: Scheme 3

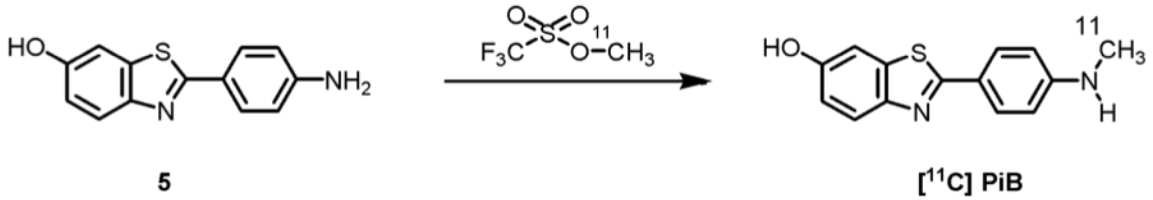

5 **[^{11}C] PiB**

Scheme 3

*Preparation of 6-hydroxy-2-(4'-{[^{11}C]methyalamino}phenyl)benzothiazole (**10**). [^{11}C]Methyl triflate bubbled into a solution of 2-3 mg of 2-(4'-aminophenyl)-6-hydroxybenzothiazole (**5**) in 300 µl of acetone at -10° C in a V-shaped vial immersed in an ice – salt cooling bath. Upon maximal trapping of radioactivity (~1 min), the reaction mixture was heated at 95° C for 2 min, cooled in the ice – salt cooling bath and quenched with 0.5 mL of ethanol:water (42:58 v/v) and injected into a Waters Symmetry Prep C_{18} (300 x 7.8 mm; 7 µm) HPLC column. The HPLC column was eluted with a mobile phase of ethanol:sterile water (42:58 v/v) at a flow rate of 3.5 ml/min. The column effluent was monitored with UV (350 nm) and gamma radioactivity detectors. Under these conditions, chemically and radiochemically pure [^{11}C]PiB (**10**) eluted with a retention time of 9-10 min.*

[^{11}C]Carbon dioxide was produced via $^{14}N(p,\alpha)^{11}C$ nuclear reaction by irradiating a mixture of 99 % $^{14}N_2$ and 1 % $^{16}O_2$ in an aluminum target body with 11 MeV protons in a RDS-112 cyclotron. A typical irradiation utilized 40 µA of 11 MeV protons for 60 min to produce about 1.4 Ci of [^{11}C]CO_2 which was preferentially cryo-trapped in a stainless steel coil dipped in liquid argon. The [^{11}C]CO_2 was subsequently released by warming the stainless steel coil, mixed with hydrogen gas and passed through a nickel catalyst kept at 400^o C to obtain [^{11}C]CH_4. [^{11}C]CH_4 was mixed with iodine vapors and helium gas and passed through a quartz tube at ~ 850^o C to produce [^{11}C]CH_3I. [^{11}C]CH_3I in helium was then passed through a cartridge of silver triflate at 180^o C which produced [^{11}C]methyl triflate.

[^{11}C]Methyl triflate thus produced was bubbled into a solution of 2-3 mg of 2-(4'-aminophenyl)-6-hydroxybenzothiazole (**5**) in 300 µl of acetone at -10° C in a V-shaped vial immersed in an ice – salt cooling bath. Upon maximal trapping of radioactivity (~1 min), the reaction mixture was heated at 95º C for 2 min, cooled in the ice – salt cooling bath and quenched with 0.5 mL of ethanol:water (42:58 v/v) and injected into a Waters Symmetry Prep C_{18} (300 x 7.8 mm; 7 µm) HPLC column. The HPLC column was eluted with a mobile phase of ethanol:sterile water (42:58 v/v) at a flow rate of 3.5 ml/min. The column effluent was monitored with UV (350 nm) and gamma radioactivity detectors. Under these conditions, chemically and radiochemically pure [^{11}C]PiB (**10**) eluted with a retention time of 9-10 min. This fraction containing the radiolabeled product was collected, diluted with an equal volume of sterile water, passed through a classic Waters C_{18} Sep-Pak cartridge [previously equilibrated with ethanol (5 mL) and sterile water (15 mL)]. The Sep-Pak was flushed with 20 mL of sterile water followed by 5 mL of sterile normal saline. The [^{11}C]PiB was eluted off the Sep-Pak with 1 mL of absolute ethanol. The ethanol solution containing [^{11}C]PiB was mixed with 9 mL of sterile normal saline and sterilized by passing through a Millex GV 0.22 µm sterile filter into a sterile multi-injection vial. The radiochemical yield for [^{11}C]PiB was 10-25% after an overall preparation time of ~ 40 min.

Overall, the preparation of [^{11}C]PiB in our laboratories followed the USP 823 guidelines for the production of positron emitter labeled biomarkers. Each batch of [^{11}C]PiB produced was subjected to quality control tests for chemical and radiochemical purities and apyrogenicity before administered into humans. Sterility of the biomarker preparation was also ascertained as per USP 823 guidelines.

The chemical and radiochemical purities of the final [^{11}C]PiB product was determined by analytical HPLC: Column: Waters Symmetry C_{18}, 150 x 4.6 mm, 5 μm; Mobile phase: ethanol:water (50:50 v/v); Flow rate: 0.7 ml/min; Detectors: UV (254 nm) and gamma radioactivity. Under these conditions, retention time for [^{11}C]PiB was 5.1 min and its chemical and radiochemical purities were greater than 95%. Specific activity of [^{11}C]PiB was determined by analytical HPLC and found to be 40–100 GBq/μmol (1.1-2.7 Ci/μmol) at the time of the injection. Figure 2.1.4 illustrates record of analytical HPLC for [^{11}C]-PiB preparation and confirms its purity when assessed against the cold standard.

The radionuclidic purity of the final product was determined with a calibrated HPGe detector. Radionuclidic identity was determined by the half-life measurement method.

The absence of pyrogens in the [^{11}C]PiB preparation was verified by the standard Limulus Amebocyte Lysate (LAL) test before injection into humans.

[^{11}C]PiB, prepared as described above, was tested for sterility using standard thioglycollate medium procedure over a period of two weeks and was found to be sterile.

Overall, the preparation of [^{11}C]PiB in our laboratories followed the USP 823 guidelines for the production of positron emitter labeled biomarkers. Each batch of [^{11}C]PiB produced was subjected to the quality control tests described above before administered into humans (except sterility and radionuclidic purity tests. These tests were done after the fact.).

Figure 2.1.4: Analytical HPLC of [^{11}C]-PiB Preparation

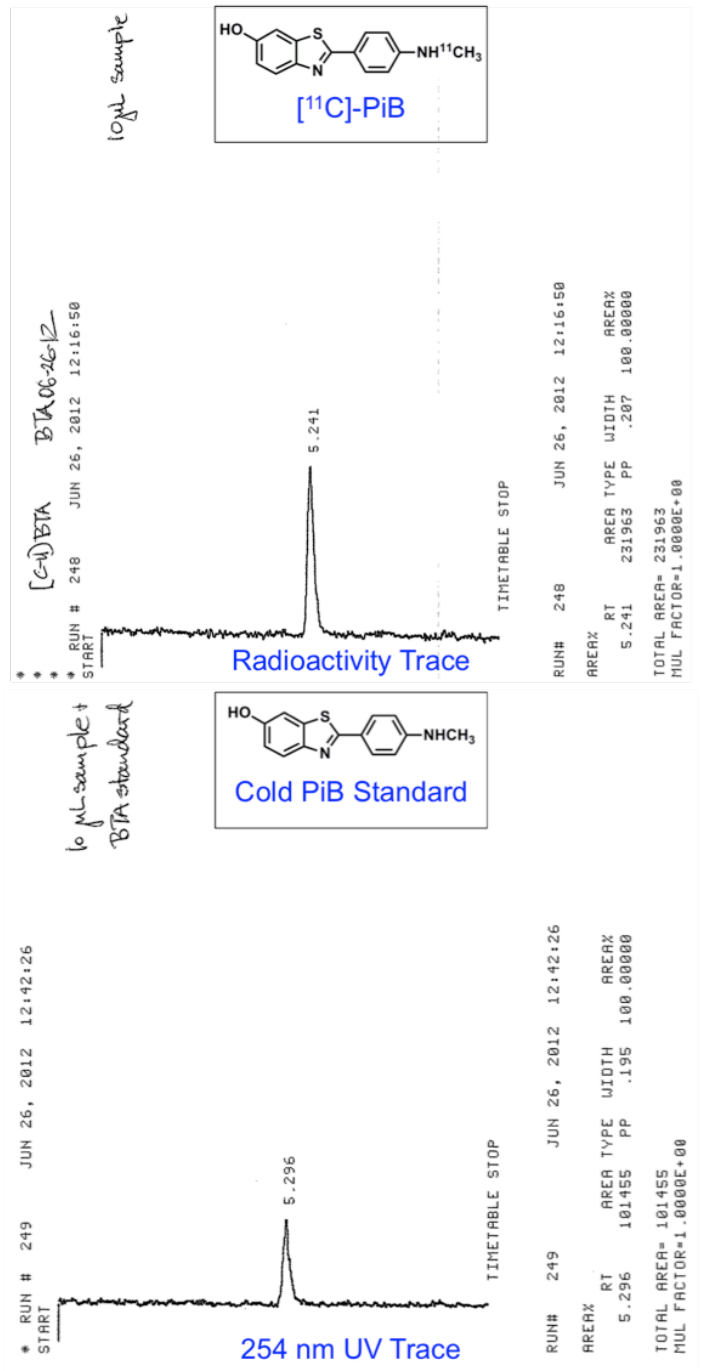

*Confirmation of the purity of [^{11}C]-PiB (**10**) eluted in the analytical HPLC based on a similar retention time to the cold standard for PiB (**10**) during the June 26, 2012 production run for [^{11}C]-PiB.*

2.2 - Patient Cohorts

Table 2.1: Moyamoya Syndrome Cohort Demographics*

Patient ID	Age	Gender	Symptoms	Clinical Presentation	Surgical Treatment
Moyamoya 1	27.0	Female	Dysphagia, dysarthria, facial droop, bilateral nystagmus, right motor deficits	radiation-induced vasculopathy, complete right ICA occlusion, severe left ICA and M1 occlusion, right intracranial vertebral occlusion, prior history of astrocytoma, and left midbrain, left pontomesencephalic and right cerebellar strokes	Ventriculoperitoneal Shunt
Moyamoya 2	30.2	Female	Headaches, insomnia, diminished cognition, problems assigning words and misplacing objects	bilateral moyamoya syndrome with ICA, ACA and MCA occlusion	Bilateral EDAS
Moyamoya 3	33.4	Female	Numbness, diffuse bilateral headaches, difficulty concentrating and articulating	Cushing syndrome	Bilateral EDAS
Moyamoya 4	38.0	Female	Headaches, carpal tunnel syndrome	moyamoya syndrome, type I diabetes	-
Moyamoya 5	38.4	Male	Lightheadedness, left arm tingling, numbness, clumsiness	moyamoya syndrome, bifrontal hypoperfusion (R>L) recommendation for right frontal bur hole surgery	Bilateral EDAS
Moyamoya 6	51.0	Male	Persistent dull bifrontal headaches	moyamoya syndrome	-
Moyamoya 7	51.2	Male	Improved palpitations	possible moyamoya disease, prior subdural hemorrhage concurrent with non-ST elevation myocardial infarct, hypertension, ventricular bigeminy	-
Moyamoya 8	55.7	Male	Dysarthria	multiple intracranial stenoses, post-operative stroke after STA-MCA bypass, 42% occlusion of clinoid segment of left ICA	STA-MCA bypass
Moyamoya 9	66.4	Female	Mild yet persistent problems with memory	intraventricular hemorrhage with history of moyamoya syndrome	-
Moyamoya 10	76.9	Female	Vertigo, hallucinations, bilateral numbness, lower extremity weakness, trigeminal neuralgia	prior right occipital stroke and atherosclerotic disease with history of moyamoya syndrome	-

***Time elapsed for Moyamoya 2-10 is approximately 6 months to 2 years between the [^{11}C]-PiB scan and diagnosis. Moyamoya 1 has had moyamoya syndrome since childhood.**

A summary of the moyamoya cohort studied in this report reveals diversity of symptoms, yet no patient had signs of dementia at the time of imaging. The mean age was 47.3±16.5, with six female and four male patients. Four of the ten patients had surgical intervention to establish a bypass. Bilateral encephaloduroarteriosynangiosis (EDAS) is an indirect revascularization procedure that places a segment of the temporal artery on the surface of the brain without an anastomosis to connect vessels. This is unlike the STA-MCA bypass that forms a junction between the superior temporal artery and the middle cerebral artery to improve perfusion. One patient had a ventriculoperitoneal shunt for hydrocephalus.

Moyamoya syndrome patients were compared against control patients, whose [^{11}C]-PiB signal was negative. [^{11}C]-PiB negative patients were defined as having an uptake ratio between global cortical tissue and that in cerebellar grey matter of less than

1.5 (Jack *et al.*, 2008). The moyamoya cohort had ten patients at varied stages of the disease whose mean age was 47.3±16.5, with six female and four male patients. Four of the ten patients had surgical intervention to establish a bypass. Bilateral encephaloduroarteriosynangiosis (EDAS) is an indirect revascularization procedure that places a segment of the temporal artery on the surface of the brain without an anastomosis to connect vessels. This is unlike the STA-MCA bypass that forms a junction between the superior temporal artery and the middle cerebral artery to improve perfusion. Moyamoya 1 presented with a ventriculoperitoneal shunt and hydrocephalus. All patients in this cohort, however, did not show signs of dementia at the time of imaging.

The control cohort had thirteen patients, of which ten were female and three were male; the mean age was 32.8±8.1. Additionally, one male 50.3 year-old patient with relapse-remitting multiple sclerosis was scanned with [^{11}C]-PiB before and one month after receiving the combination of interferon-β (Avonex®) and methylprednisolone therapy. The patient was on interferon-β prior to the first scan but received methylprednisolone with interferon-ß after the first scan.

2.3 - PET Imaging

The moyamoya and control cohorts were imaged either on the Siemens (Erlangen, Germany) ECAT-HR+ PET or Biograph 64 PET/CT Scanner. Table 2.2 indicates which scanner was assigned to which moyamoya patient. A 10 mCi intravenous [^{11}C]-PiB bolus was injected in all patients at the beginning of the scan. Moyamoya patients imaged with the ECAT-HR+ Scanner underwent a 60 minute dynamic scan with the following framing protocol: 6 x 30 seconds, 3 x 1 minute, 3 x 3 minutes and 9 x 5

minutes. Reconstruction of dynamic images utilized filtered backprojection with a 5.0mm transaxial and z-direction FWHM Hann filter and a 128x128 matrix. A final resolution of 1.47 mm x 1.47 mm x 2.43 mm (128x128x63) resulted after application of the referenced movement correction procedure (Wardak *et al.*, 2010). Images acquired with the ECAT HR+ were attenuation corrected by transmission scans with a rotating ^{68}Ge rod.

Table 2.2: PET Imaging Protocol for Moyamoya Cohort

Patient ID	PET Scanner	Scan Duration	Histogram Protocol	Final Resolution
Moyamoya 2 **Moyamoya 5** **Moyamoya 9** **Moyamoya 10**	ECAT HR+	60 minutes	6 x 30 seconds, 3 x 1 minute, 3 x 3 minutes and 9 x 5 minutes	1.47 mm x 1.47 mm x 2.43 mm (128x128x63)
Moyamoya 1 **Moyamoya 3** **Moyamoya 4** **Moyamoya 6** **Moyamoya 7** **Moyamoya 8**	Siemens Biograph 64 PET/CT	60 minutes	6 x 30 seconds, 4 x 3 minutes and 9 x 5 minutes	2.04 mm x 2.04 mm x 2.03 mm (128x128x109)

A summary of the PET imaging protocol for the moyamoya cohort. Patients in this cohort were divided between the ECAT HR+ and the Biograph® 64. All PET scans, however, were 60 minutes in length.

Figure 2.3: Workflow for Motion Correction

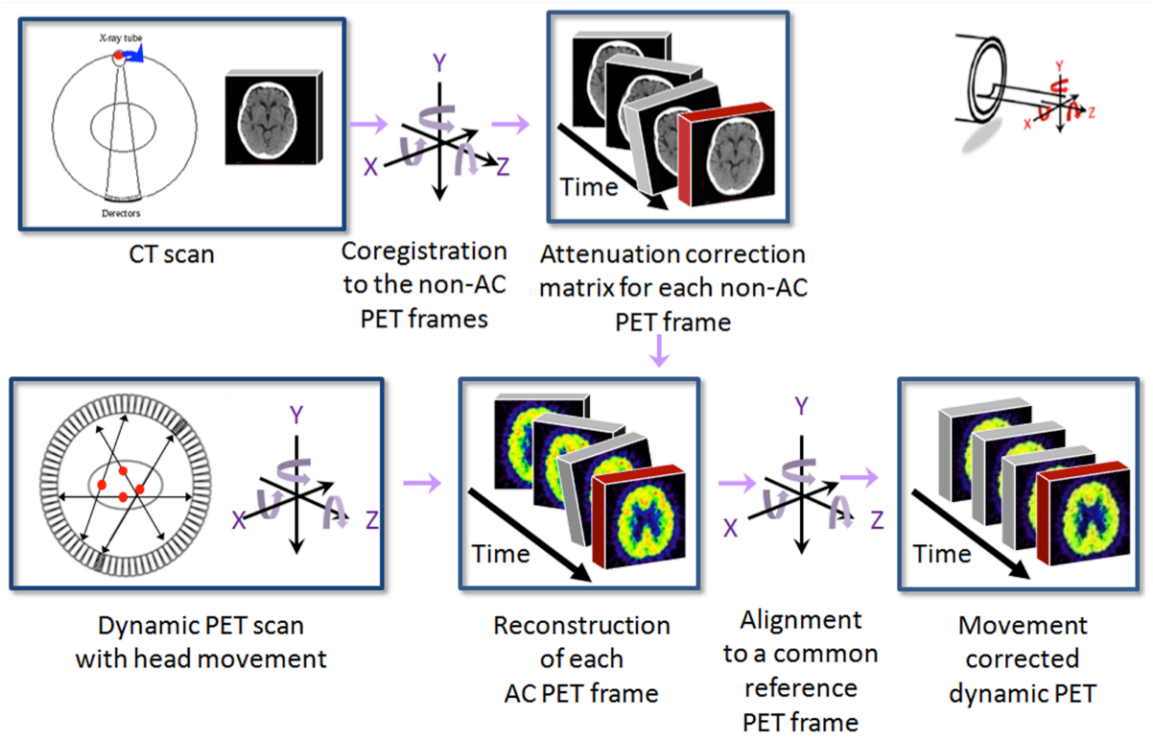

Ye H, *et al. PLoS One* 2014; 9(8): e103745.

An overview of movement correction performed on all PET images to suppress motion artifacts that can impact quantification. This workflow was similar for images from both scanners, except that the ECAT HR+ scanner had ^{68}Ge transmission scans that provided attenuation data. Attenuation data was coregistered to the non-corrected PET frames before reconstruction of attenuation-corrected frames. After reconstruction, all PET frames were aligned to an earlier frame around five minutes into the scan, where limited motion was observed.

The scanning protocol observed for some moyamoya and all control patients imaged with the Biograph 64 were as follows: 6 x 30 seconds, 4 x 3 minutes and 9 x 5 minutes. These scans were also reconstructed using filtered backprojection to achieve a final resolution of 2.04 mm x 2.04 mm x 2.03 mm (128x128x109) also after previously referenced movement correction (Ye *et al.*, 2014). A 5.0 mm transaxial and z-direction FWHM Gaussian filter was applied with a 336 x 336 matrix. Attenuation correction for

images from this scanner was applied from a quick CT scan. The pre-treatment scan for the multiple sclerosis patient was performed on the ECAT HR+ scanner, while the post-treatment scan was performed on the Biograph 64; both scans observed the aforementioned protocol for each scanner and received motion correction. Figure 2.3 summarizes the motion correction workflow and is fundamentally equivalent for images acquired from both scanners. Affine registration to an earlier frame suppresses motion artifacts that can impact signal quantification.

2.4 - MRI Imaging

The control cohort received structural T1 MRI scans. The MP-Rage sequence performed by the Siemens (Erlangen, Germany) 1.5 T Sonata scanner at UCLA Medical Center (TR=1900 msec, TE=4.38 msec, TI=1100 msec, flip angle = 15°) to achieve a final resolution of 1.2 mm x 1.05 mm x 1.05 mm (176x240x256). The multiple sclerosis patient also received a T1 MRI that observed the same protocol.

The entire moyamoya cohort received both T2 and diffusion weighted MRI scans. The protocol for T2 scanning used the Siemens (Erlangen, Germany) TrioTrim 3.0 T scanner at UCLA Medical Center. The tseB2dl_30 sequence was applied (TR=6470 msec, TE=107 msec, flip angle = 120°) that resulted in a final resolution of 0.58 mm x 0.58 mm x 6.5 mm (384 x 384 x 23).

Some moyamoya patients received a contrast enhanced T1 MRI with a Siemens (Erlangen, Germany) 3.0T Verio Scanner. A 20 cc bolus of Multihance® was injected in patients prior to the application of the fl2dl sequence (TR=250 msec, TE=2.58 msec, flip angle = 70°) to achieve a final resolution of 0.6875 mm x 0.6875 mm x 6.5 mm (260x320x22).

Diffusion weighted MRI scanning was performed on the Siemens (Erlangen, Germany) Avanto 1.5 T scanner at UCLA Medical Center with the ep_b0_1000 sequence (TR=4100 msec, TE=89 msec, flip angle = 90°; *b*=1000 sec/mm^2). This protocol achieved a final resolution of 1.69 mm x 1.69 mm x 6 mm (130x130x26). Apparent Diffusion Coefficient image maps were then constructed using Equation 2.4:

$$ADC = \left(D_{xx} + D_{yy} + D_{zz}\right)/3 = -\frac{1}{b}\ln\left[\frac{S_{DWI}}{S_0}\right] \quad (2.4).$$

The Diffusion Weighted Image signal (S_{DWI}) is the MRI created where *b*=1000 sec/mm^2, and the baseline MRI signal is the MRI created with no applied field. The DWI MRI represents the trace of the signal, whereas ADC is the average of the direction specific diffusion coefficients. The advantage of using DWI and ADC maps is that each highlights specific information. Diminished ionic gradients in ischemic stroke cause restricted diffusion that is bright on DWI MRI where ADC will be dark (Schaefer *et al.*, 2000). Diffusion MRI, therefore, can confirm perfusion related damage.

2.5 - Image Analysis

Parametric PET images used the Simplified Reference Tissue Model to measure Distribution Volume Ratio (SRTM DVR) of [^{11}C]-PiB with cerebellar grey matter as reference tissue. SRTM DVR values from these parametric images reflect accumulation of tracer in tissue. SRTM has been established to be less time sensitive than other parametric methods, such as Logan, and was validated with 60 minutes of dynamic scanning for [^{11}C]-PiB with cerebellar grey matter as a reference tissue (Lammertsma and Hume, 1996; Lopresti *et al.*, 2005; Meyer *et al.*, 2011). The SRTM equation is written as Equation 2.5.1 below:

$$C_T(t) = R_1 C_R(t) + \left(k_2 - \frac{R_1 k_2}{DVR}\right) C_R(t) \otimes e^{-\left(\frac{k_2}{DVR}\right)t} \quad (2.5.1).$$

SRTM provides DVR as well as R_1, which is the ratio of tracer influx in target tissue divided by that in reference tissue. Its estimation relies upon counts from the tracer in the target and reference tissues as well as the efflux rate from target tissues (C_T, C_R, and k_2 respectively). A basis model approach, however, has simplified calculation of SRTM in the Equation 2.5.2 (Gunn *et al.*, 1997).

$$C_T(t) = \alpha_1 C_R(t) + \alpha_2 B_i(t);$$

$$\alpha_1 = R_1;\ \alpha_2 = k_2 - \left(\frac{R_1 k_2}{DVR}\right);$$

$$\theta_i = \left(\frac{k_2}{DVR}\right) + \lambda;$$

$$B_i(t) = C_R(t) \otimes e^{-\theta_i t} \quad (2.5.2).$$

λ is the physical decay constant for the isotope. With weighted linear least squares regression, a set of discrete values can be tested for θ_i to determine the basis functions for $B_i(t)$. Constraints set at $\frac{0.0007}{sec} < \theta_i < \frac{0.0004}{sec}$ for [^{11}C]-PiB were appropriate for SRTM determination for a 90-minute scan (Lopresti *et al.*, 2005). A 60-minute [^{11}C]-PiB scan also produced reliable data that agreed with existing values for cerebellar efflux rates (Meyer *et al.*, 2011). SRTM, however, does have underlying assumptions that are critical to observe for accurate assessment of uptake (Salinas *et al.*, 2015):

1.) The reference region is devoid of specific/displaceable binding.

2.) The kinetic behavior of the tracer in both the reference and target tissue can be represented by a one Tissue Compartment model.

3.) The blood volume (V_B) contribution to both the reference and target tissues is negligible.

4.) Reference and target tissue have the same non-displaceable volume of distribution (V_{ND}).

[^{11}C]-PiB has no cerebellar grey matter binding in these patients, yet the effect of partial volume is not negligible in these patients on account of tissue damaged from hypoxia. Other kinetic models, however, would also be susceptible to partial volume effects, particularly in the reference region. Each case had cerebellar grey matter reference regions carefully segmented from MRI that was carefully overlaid with grey matter in early frames to limit potential spillover from white matter in later frames. The time activity curves also demonstrated one compartment dynamics where gradual decline in the later frames followed a surge of influx in the first few frames.

The procedure for image analysis was previously referenced (Wong *et al.*, 2015). Figure 2.5 summarizes the workflow of the image analysis. Briefly stated, all MP-Rage MRI scans in the control cohort and T2 MRIs in the moyamoya cohort were warped to an atlas, whose volumes of interest (VOIs) transformed into patient MRI space were then coregistered to patient PET images using the symmetric image normalization (SyN) method implemented in the Advanced Normalization Tools (ANTs) version 1.9 release 4 (Avants *et al.*, 2008). The Johns Hopkins White Matter DTI Atlas was applied as the template with its entire VOI set generated for each patient (Mori *et al.*, 2008; Oishi *et al.*, 2009). Additionally, VOIs were drawn on the Johns Hopkins atlas to reflect tissue perfused by major arteries using the ITK-Snap as per the referenced text (Yushkevich *et al.*, 2006; Tatu *et al.*, 2012).

Figure 2.5: Workflow for Image Analysis

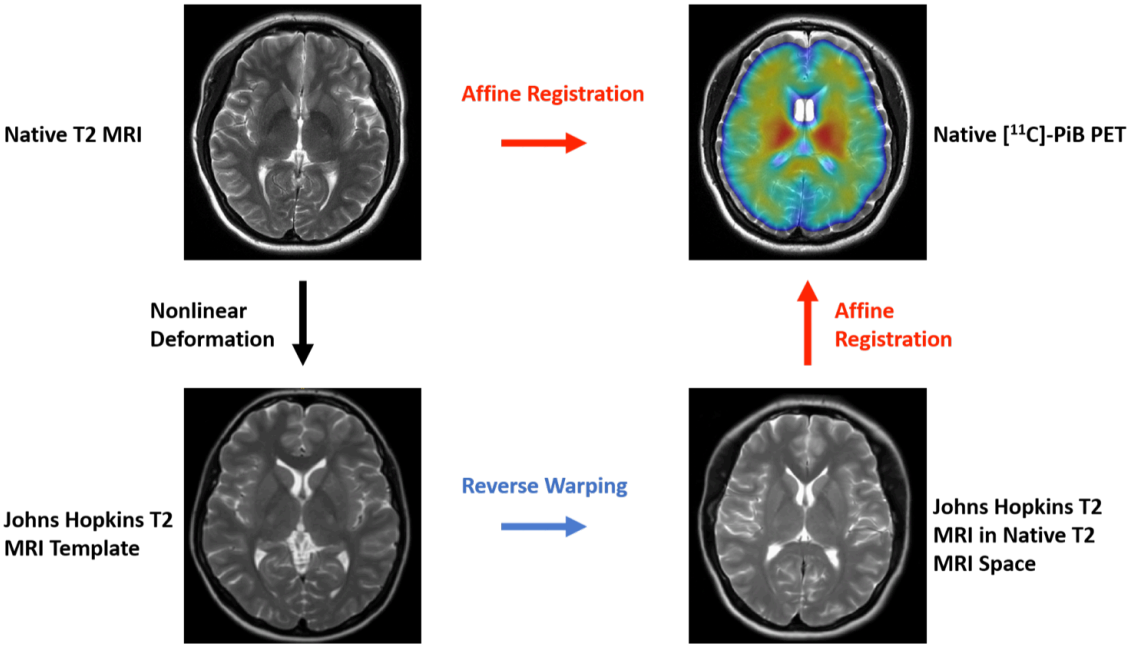

A summary of the image analysis in this study. Native MRI scans were T2 weighted for the moyamoya cohort and T1 weighted for the controls and the multiple sclerosis patient. Each patient MRI was coregistered to a summed PET image comprising of the first few minutes of the scan, as noted by the top row with the red arrow for affine registration. Native MRI scans were also warped to the Johns Hopkins template, which offered both a T1 and T2 template to accommodate for the differences between structural MRI protocols for the controls and moyamoya patients. Warping entailed affine registration of the patient scan to the template followed by nonlinear deformation, where the fixed image was the template MRI. Only Moyamoya 1 had the subject image as the fixed image, as several large lesions were masked out to facilitate more stable warping. The transformation matrix from warping was applied to generate volumes of interest (VOIs) in the native MRI space that were then coregistered into the PET space.

When warping the subject MRI images, the Johns Hopkins template was the fixed image. Warping would entail affine registration of the subject MRI to the template that was followed by non-linear deformation. The only instance when the subject MRI was the fixed image was with Moyamoya 1, whose damage to the brain produced several large lesions. These lesions interfered with warping, which required binary masks of the lesions to be created in ITK-Snap. These masks nullified damaged regions during the warping process and enabled relatively successful warping to continue with an intact

cerebellum and subcortical structures.

2.6 - Animal Experimentation

All procedures and protocols pertaining to animal experimentation, autoradiography and tissue staining have been reported previously (Cole, 2011). Briefly stated, all animal experiments were in compliance with the UCLA Animal Care and Use Committee guidelines. A middle cerebral arterial occlusion (MCAO) procedure was performed on male rats with one hour of occlusion. After 48 hours of reperfusion, animals were unconscious when injected with 10-15 mCi of [^{11}C]-PiB for 30 minutes of uptake prior to being sacrificed with pentobarbital overdose. Brain tissue was flash frozen with 2-methylbutane and ethanol before being sectioned in 20 μm sections. These sections were exposed to phosphor plates for 3 hours before scanning, in addition to undergoing immunhistochemical (IHC) staining SULT1E1 and 2,3,5-Triphenyltetrazolium Chloride (TTC) staining that would identify the ischemic core.

2.7 - Statistical Analysis

All statistical analysis was performed with R-Studio version 0.99.486 (Team, 2015). Non-parametric analysis was used to establish statistically significant differences between [^{11}C]-PiB uptake in patients with moyamoya syndrome and controls by using the Wilcoxon rank sum and Kruskal-Wallis tests. Neither associations between gender and diagnosis nor age and diagnosis achieved statistical significance when verified with Friedman testing. Non-parametric cross correlation analysis was performed in R-Studio using the Latent Traits Model package (Rizopoulos, 2013-12-20). All statistical analysis was corrected for multiple comparisons using the Holm correction.

Chapter Three: Results

3.1 - Confirmation that SULT1E1 is a target for [^{11}C]-PiB in MCAO Model

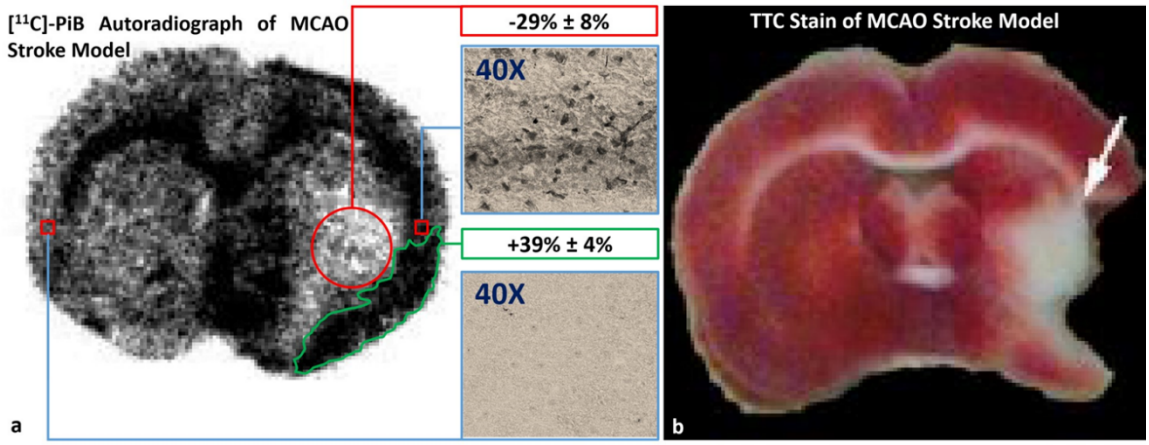

Figure 3.1: Uptake of [^{11}C]-PiB and SULT1E1 Confirmation in MCAO Model
Autoradiography of a non-hemorrhagic stroke model in a rat 48 hours after reperfusion with [^{11}C]-PiB. (a)The ischemic core, represented by the red circle, had suppressed retention of [^{11}C]-PiB compared to the contralateral side, whereas the peri-infarct region represented in green had elevated [^{11}C]-PiB when compared to the contralateral side. IHC staining for SULT1E1 expression demonstrates dense expression in the peri-infarct region, whereas the contralateral side lacked visible expression. (b) The white region in TTC stain confirms the presence of the ischemic core.

A non-hemorrhagic middle cerebral arterial occlusion (MCAO) model of ischemic stroke in Figure 3.1a confirms a distribution of [^{11}C]-PiB within the peri-infarct area that is elevated when compared to the contralateral side. The [^{11}C]-PiB signal within the ischemic core, however, is suppressed when compared to the contralateral side. Additionally, Figure 3.1b validates the location of the ischemic core with the TTC stain, where diminished tracer uptake was noted when compared to the contralateral side. The SULT1E1 IHC staining confirms dense expression in the peri-infarct region that is absent on the contralateral side. Hence, the resulting [^{11}C]-PiB signal is peripheral to the site of injury and is consistent with SULT1E1 expression there.

SULT1E1 expression and activity demonstrates variability in the presence of cytokines and pathogenesis of disease. SULT1E1 expression exhibited strong positive correlation with tumor necrosis-factor α (TNF-α) expressed in adipocytes (Ahima *et al.*, 2011). Vascular smooth muscle cells (VSMCs) from atherosclerotic patients demonstrated an increase in SULT1E1 expression and decrease in STS activity upon the introduction of interleukin 1-β (IL-1β), where the effect was more pronounced in severe postmenopausal female patients (Nakamura *et al.*, 2003; Nakamura *et al.*, 2005). Hence, SULT1E1 expression and activity can reflect dynamic changes in inflammation resulting from disease.

The presence of reactive astrocytes ipsilateral to the ischemic core in the peri-infarct area and the formation of the glial scar follow MCAO (Shimada *et al.*, 2010). Astrocytes are a well-defined source of cytokines and matrix metalloproteinases (MMPs) that respond to brain injury (Ridet *et al.*, 1997; Muir *et al.*, 2002). Augmented cytokine signaling and metalloproteinase activity following ischemia induces destruction of tissue.

Among its paracrine signaling roles, estrogen provides an equilibrating response to inflammation. The action of estrogen on inflammation includes direct action with both immune cells and inflammatory factors that mediate progression of disease (Straub, 2007). Cytokines, in particular, are chemical messengers that mediate the onset of inflammation. Among many functions, their release coordinates signaling endocrine, paracrine and autocrine signaling in addition to the induction of chemotaxis (Arai *et al.*, 1990). Estrogen can suppress the onset of inflammation through inhibition of polymorphonuclear leukocyte migration and cytokine reduction in response to vascular injury (Miller *et al.*, 2004; Nadkarni *et al.*, 2011). Attenuation of cytokine-mediated

inflammation in tissue, therefore, requires coordinated availability of estrogen, thereby making estrogen sulfotransferase activity susceptible to change with inflammation.

Figure 3.1 demonstrated a model of focal ischemic lesion within a rat that underwent MCAO surgery. The elevated [^{11}C]-PiB uptake and pronounced SULT1E1 immunohistochemical stain in the peri-infarct region are suggestive of active estrogen metabolism. Acute elevations of IL-1 β in the rat brain have been reported after the development of focal ischemia (Liu *et al.*, 1993). Reactive astrocytic proliferation ipsilateral to the ischemic core is a known phenomenon (Shimada *et al.*, 2011). Astrocytes within the per-infarct region are also known to express aromatase following MCAO (Carswell *et al.*, 2005). Enhanced expression and activity of aromatase in addition to elevated estradiol levels protect neurons and reduce reactive gliosis (Garcia-Segura *et al.*, 1994; Arevalo *et al.*, 2015). The pattern of [^{11}C]-PiB retention in the peri-infarct region is consistent with the previously reported literature concerning images of ischemic stroke patients with [^{11}C]-PiB (Ly *et al.*, 2012). The density of the SULT1E1 stain in the peri-infarct region, however, is consistent with the [^{11}C]-PiB affinity for the enzyme in addition to the presence of other estrogen regulatory enzymes responding to astrogliosis, such as aromatase. Estrogen metabolism in the peri-infarct region, therefore, reflects a response to injury from cerebral ischemia.

Estrogen sulfotransferase (SULT1E1) is a regulatory enzyme for the metabolism of estrogen. SULT1E1 has a global distribution with confirmed reports of expression in both human fetal and adult tissues. Adult tissues in particular demonstrate SULT1E1 expression in the aorta, adrenal gland, endometrial tissue and brain, among other tissues (Miki *et al.*, 2002). SULT1E1 sulfates the hydroxyl group at the third carbon of estrogen,

which can subsequently disable the hormone from binding to its receptor. SULT1E1 demonstrates high affinity for both estradiol and estrone at low concentrations to facilitate sulfation (Falany, 1997). Sulfation by SULT1E1 can also establish a reservoir for the hormone within the cell since steroid sulfatase (STS) can remove the sulfate moiety. Together, the pair of enzymes modulates the availability of estrogen in target tissues (Hobkirk, 1985; Song, 2001).

Sulfotransferases contribute to the metabolism of xenobiotic, foreign and endogenous compounds by facilitating sulfation of compounds. Sulfotransferases enable sulfation by catalyzing the transfer of the sulfonate moiety from 3'-phosphoadenosine 5'-phosphosulfate (PAPS) to either a hydroxyl group to form a sulfate ester or to an amine group resulting in a sulfamate ester (Falany, 1997). Sulfated compounds can augment the solubility of metabolites for excretion through the renal or hepatobiliary systems yet can also alter biological availability and activity. Sulfation entails enzymatic processing with high affinity and low capacity, as opposed to glucuronidation by UDP-glucuronosyltransferases high capacity and low affinity (Burchell and Coughtrie, 1997). Metabolism of low-level exposure compounds, therefore, are more likely to be addressed by sulfotransferases (Gamage *et al.*, 2006).

Sulfotransferases can be broadly divided into membrane-bound and cytosolic variants. Membrane-bound sulfotransferases are found on the Golgi apparatus and sulfate proteins, lipids and glycosaminoglycans, while the cytosolic enzymes participate in metabolism of xenobiotics and small endogenous substrates such as steroids, bile acids and neurotransmitters (Falany, 1997; Negishi *et al.*, 2001). Cloning and characterization of 47 mammalian sulfotransferase isoforms, one insect isoform, eight plant isoforms from

nine sulfotransferase families and 14 subfamilies have transpired (Blanchard *et al.*, 2004). There are three families of human sulfotransferases, SULT1, SULT2 and SULT4, that contain thirteen members, of which nine cytosolic sulfotransferases have confirmed crystal structures (Gamage *et al.*, 2006). Table 3.1 summarizes the location and substrates for human cytosolic sulfotransferases, which participate in both the metabolism of both xenobiotic and endogenous substrates throughout the body.

Bovine SULT1E1 cDNA was the first cloned SULT1E enzyme, yet researchers also isolated SULT1E members from a variety of species including the guinea pig, rat, mouse and pig (Nash *et al.*, 1988; Blanchard *et al.*, 2004). Ultimately, human SULT1E1 cloning from a human liver library confirmed high activity with estradiol and estrone at physiological concentrations, unlike SULT1A1 and SULT2A1 (Falany *et al.*, 1995; Falany, 1997). SULT1E1 also sulfates thyroid hormones but at notably higher concentrations than estrogens (Kester *et al.*, 1999).

SULT1E1 was the first cytosolic sulfotransferase to be crystallized among the nine crystallized cytosolic sulfotransferases. Specifically, the crystallization of murine SULT1E1 confirmed that His108 coordinated to the 3-phenolic group of estradiol and acted as a catalytic base in the sulfuryl transfer mechanism (Kakuta *et al.*, 1997). In all cytosolic sulfotransferases, His108 is a conserved residue, the absence of which by mutation experiments eliminated activity in murine SULT1E1 (Kakuta *et al.*, 1998). Additional studies with crystal structures of human SULT1E1:PAPS elucidated the role of additional residues that coordinated the S_N2 in-line displacement mechanism catalyzing the sulfation of estrogens in the active site of SULT1E1 (Pedersen *et al.*, 2002).

Table 3.1: Brief Summary of Substrates and Locations for Human Cytosolic Sulfotransferases

Subfamily	Endogenous Substrates	Xenobiotic Substrates	Location
SULT1A1	Iodothyronines: 3,3'diiodothyronine (T2), 3,3',5-triiodothyronine (T3), (Anderson et al., 1995; Li et al., 2001); Estrogens: β-estradiol (E2) (Falany, 1997)	Simple phenolic compounds: p-nitrophenol, m-nitrophenol, p-ethylphenol, p-cresol (Wilborn et al., 1993; Brix et al., 1999b); Drugs: paracetamol (Lewis et al., 1996), minoxidil (Meisheri et al., 1993); Carcinogens: N-Hydroxy -PhIP (Ozawa et al., 1994).	Adrenal Gland, Brain, Breast, Kidney, Intestine, Endometrium, Jejunum, Lung, Placenta, Platelets
SULT1A2	Not known	Simple phenolic compounds: p-nitrophenol (Zhu et al., 1996); Carcinogens: N-Hydroxy –2-AAF (Glatt, 2000)	Liver and Colon
SULT1A3	Catecholamines: dopamine, (Brix et al., 1999b; Dajani et al., 1999b), Norepinephrine (Ganguly et al., 1995)	Simple Phenols: p-nitrophenol (Brix et al., 1999b); Carcinogens: 1-Hydroxymethylpyrene (Glatt, 2000)	Jejunum, Lung
SULT1B1	Iodothyronines: 3,3'diiodothyronine (T2), 3,3',5-triiodothyronine (T3), 3,3',5'-reverse triiodothyronine (r-T3), and thyroxine (T4) (Wang et al., 1998)	Simple Phenol: 1-Naphthol (Wang et al., 1998)	Colon, Circulating Leukocytes, Liver, Small Intestine
SULT1C2	Not known	Simple Phenols: p-nitrophenol (Sakakibara, 1998b); Carcinogens: N-Hydroxy-2-AAF (Yoshinari et al., 1998b)	Kidney, Stomach, Thyroid
SULT1C4	Not known	Simple Phenols: p-nitrophenol (Yoshinari et al., 1998a); Carcinogens: N-Hydroxy-2-AAF (Sakakibara et al., 1998b)	Kidney, Ovary, Spinal Cord
SULT1E1	Estrogens: E2, estrone (E1) (Falany et al., 1995)	Estrogens: 17-ethinyl-E2, equilenin (Falany et al., 1995); Catechol estrogens: 2-hydroxyestrone, 2-hydroxyestradiol, 4-hydroxyestrone; 4-hydroxyestradiol (Adjei and Weinshilboum, 2002)	Brain*, Endometrium, Jejunum, Liver
SULT2A1	Steroids: DHEA (Comer and Falany, 1992)	Carcinogens: 1- Hydroxymethylpyrene (Meinl et al., 2002), 6 Hydroxymethylbenzo[a]-pyrene, hycanthone (Glatt, 2000)	Adrenal Gland, Brain, Bone Marrow, Liver, Small Intestine
SULT2B1_v1	DHEA (Her et al., 1998), Pregnenolone (Meloche and Falany, 2001)	Not known	Placenta, Prostate, Small Intestine, Trachea
SULT2B1_v2	DHEA (Her et al., 1998), pregnenolone (Meloche and Falany, 2001), cholesterol and oxysterols (Geese and Raftogianis, 2001)	Not known	Adrenal Gland, Colon, Kidney, Lung, Ovary, Placenta, Prostate, Small Intestine, Thymus, Thyroid, Trachea
SULT4A1	Not known	Not known	Brain

Contents summarized from Gamage N, *et al. Toxicol Sci* 2006; 90(1): 5-22. *SULT1E1 cDNA expression reported by Miki Y, et al. *The Journal of Clinical Endocrinology and Metabolism* 2002; 87(12): 5760-8.

A summary of human cytosolic sulfotransferases, their substrates and locations with confirmed expression.

Figure 3.1.1: Steroidal and Non-steroidal Substrates for SULT1E1

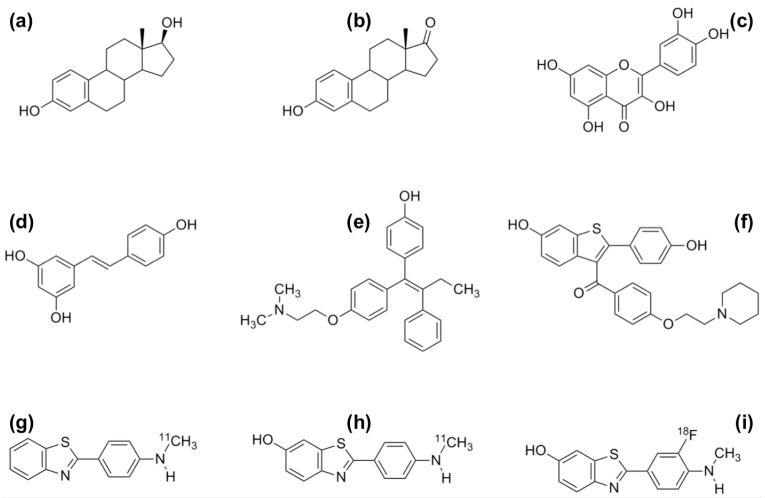

Figure 3.11: Substrate Affinity for Estrogen Sulfotransferase (SULT1E1)

	Compound	Classification	K_m (μM)	Reference
Steroidal Structures	**Estradiol (a)**	Steroidal Hormone	0.020	Falany CN. FASEB J 1997; 11(4): 206-16.
	Estrone (b)	Steroidal Hormone	0.020	
Non-Steroidal Structures	**Quercetin (c)**	Polyphenol	0.32	Otake Y, et al. J Steroid Biochem Mol Biol 2000; 73(5): 265-70.
	Resveratrol (d)	Polyphenol	0.53	
	(Z)-4-Hydroxytamoxifen (e)	Selective Estrogen Receptor Modulator	0.2 ± 0.1	Falany JL, et al. Drug Metab Dispos 2006; 34(3): 361-8.
	Raloxifene (f)	Selective Estrogen Receptor Modulator	*	
	Pittsburgh Compound A (g)	Benzothiazole Imaging Agent	++	Kepe V, et al. J Alzheimers Dis 2013; 36(4): 613-31.
	Pittsburgh Compound B (h)	Benzothiazole Imaging Agent	1.42 ± 0.12	Cole GB, et al. PNAS 2010; 107(14): 6222-7.
	[^{18}F]-Flutemetamol (i)	Benzothiazole Imaging Agent	0.56 ± 0.09	

*Formation of multiple sulfonated products prevented a reliable estimate. ++No value reported since the compound is not an eligible substrate for SULT1E1.

A summary of steroidal and non-steroidal substrates for SULT1E1 confirms phenolic substituents are eligible for sulfation.

The inherent function of SULT1E1 is to regulate estrogen metabolism, yet SULT1E1 is also capable of metabolizing non-steroidal structures. Figure 3.1.1 summarizes steroidal and non-steroidal substrates for SULT1E1 and their K_m values. In addition to a high affinity for estrogens, SULT1E1 sulfates Selective Estrogen Receptor Modulating (SERM) drugs such as tamoxifen. Additionally, SULT1E1 demonstrates an affinity for polyphenolic compounds. While Otake and colleagues have reported a low micromolar K_m for both quercetin and resveratrol, Furimsky and colleagues confirmed that SULT1E1 sulfates resveratrol at all three hydroxy groups with resveratrol 4'-O-sulfate as the main metabolite (Furimsky *et al.*, 2008). Raloxifene does not have an accurate K_m estimate for SULT1E1 on account of multiple sulfated products that include a disulfate (Falany *et al.*, 2006). Nonetheless, these compounds collectively illustrate how SULT1E1 sulfates substrates with phenolic substituents at low concentrations.

Interestingly, benzothiazoles are molecules utilized in radiolabeling for amyloid imaging that are evidently substrates for SULT1E1. Pittsburgh Compound B ([^{11}C]-PiB) and [^{18}F]-Flutemetamol have low micromolar K_m values for SULT1E1, yet the absence of a hydroxyl group in Pittsburgh Compound A ([^{11}C]-PiA) causes it to lack affinity for the enzyme. PET imaging with [^{11}C]-PiA achieved a different tracer distribution when compared to [^{11}C]-PiB. Figure 3.1.2 illustrates rather disparate PET uptake between [^{11}C]-PiA and [^{11}C]-PiB in patients with Alzheimer's Disease that display a different cortical pattern. While the K_i for amyloid ß fibrils is better with [^{11}C]-PiB, it does not explain the difference in signal adequately, as [^{11}C]-PiB possesses a low micromolar K_m for SULT1E1 that [^{11}C]-PiA lacks altogether. Thus, the resulting differences in PET signal reflect how the presence of the 6-hydroxy group within [^{11}C]-PiB does not cause

the tracer to label amyloid exclusively. Alternatively, the affinity of [^{11}C]-PiB for SULT1E1 that [^{11}C]-PiA lacks justifies the enzyme as a target for the tracer.

Cole and colleagues verified the affinity of many benzathiazole compounds with several sulfotransferases and found that SULT1E1 had the highest affinity when tested against SULT1A1*1, SULT1A1*2, SULT1A3 and SULT2A1 (Cole *et al.*, 2010). Specifically, the report disclosed that 6-hydroxy-2arylbenzothiazole substrates demonstrated a high V_{max}/K_m and subsequently notable affinity for SULT1E1 not seen with SULT1A1*1. The report further revealed several excellent correlations that further established 6-hydroxy-2arylbenzothiazole compounds as potent substrates for SULT1E1. The $\log(V_{max}/K_m)$ of these compounds correlated well with their respective polarities of the 4'substituents on the 2-aryl moiety, acidity of the 6-phenolic group, acidity mediated by the electron withdrawing capacity of the 4'substituent ($r = 0.964$ for Hammet σ_p, $r = 0.963$ for δ_{OH} from ^{1}H NMR, and $r = 0.987$ for δ_{C2} from ^{13}C NMR, respectively). The report further corroborated the capacity of SULT1E1 to metabolize [^{11}C]-PiB by verifying the presence of [^{11}C]-PiB-6-O-Sulfate in tissues ground after intravenous injection and imaging of animal models. The analysis confirmed [^{11}C]-PiB-6-O-Sulfate retention both throughout the rat brain and peripheral mouse tissue. The subcortical and hepatic tissues contained the highest [^{11}C]-PiB-6-O-Sulfate fractions in the brain and peripheral tissues (64.8% ± 1.8% and 82.7% ± 5.1% of total radioactivity, respectively); the plasma also contained a substantial [^{11}C]-PiB-6-O-Sulfate fraction that confirms peripheral sulfation. These results establish 6-hydroxy-2arylbenzothiazole compounds as potent substrates for SULT1E1. Moreover, sulfated metabolites trapped in regions with

high uptake reveal the impact of sulfation when imaging with [^{11}C]-PiB. These in-vitro and in-vivo results elucidate the role of SULT1E1 in [^{11}C]-PiB signal.

The [^{11}C]-PiB-6-O-Sulfate metabolite witnessed in brain tissue is a direct consequence of sulfation by SULT1E1 in the brain itself. When Klunk and colleagues developed amyloid imaging tracers, their aim was to to facilitate efficient entry across the blood-brain barrier by substituting groups on Thioflavin-T derivatives to achieve hydrophobic uncharged molecules (Klunk *et al.*, 2001). [^{11}C]-PiB evolved from the benzothiazole-aniline motif and produced an uncharged hydrophobic tracer upon injection. Charged metabolites do not cross the blood-brain barrier, thus supporting the concept of the trapped metabolite in tissue. Peripheral SULT1E1, however, produces polar charged metabolites in plasma. [^{11}C]-PiB-6-O-Sulfate itself is a major peripheral metabolite found in human plasma (Phelps and Barrio, 2010). Neumaier and colleagues also noted that the metabolism for [^{11}C]-PiA was notably slower than it was for [^{11}C]-PiB (Neumaier *et al.*, 2007). While the authors attributed the propensity for glucuronidation with [^{11}C]-PiB, sulfation of [^{11}C]-PiB is an appropriately designated metabolism due to a high affinity for SULT1E1. Mathis and colleagues reported sulfated [^{3}H]-PiB metabolites from rat liver and brain homogenates but dismissed sulfation of [^{11}C]-PiB in humans, as previusly frozen human homegenates failed to produce sulfated metabolites (Mathis, 2004). While Mathis and colleagues did not entirely dismiss peripheral sulfation of [^{11}C]-PiB, their analysis of metabolites in tissue entailed critical flaws that jeopardize enzyme viability. Sulfation by SULT1E1 requires PAPS, for which ATP is required to synthesize. Frozen tissue, therefore, presents inactive enzymatic activity from sulfotransferases and ultimately SULT1E1. Hence, the pathologic validation of sulfation in the human brain

presents challenges for producing rare fresh autopsy specimens. Nonetheless, the kinetic parameters concerning [^{11}C]-PiB as a substrate for SULT1E1 rationalize sulfation by this enzyme both peripherally and in the brain.

Figure 3.1.2: Comparison Between Pittsburgh Compound A and Pittsburgh Compound B

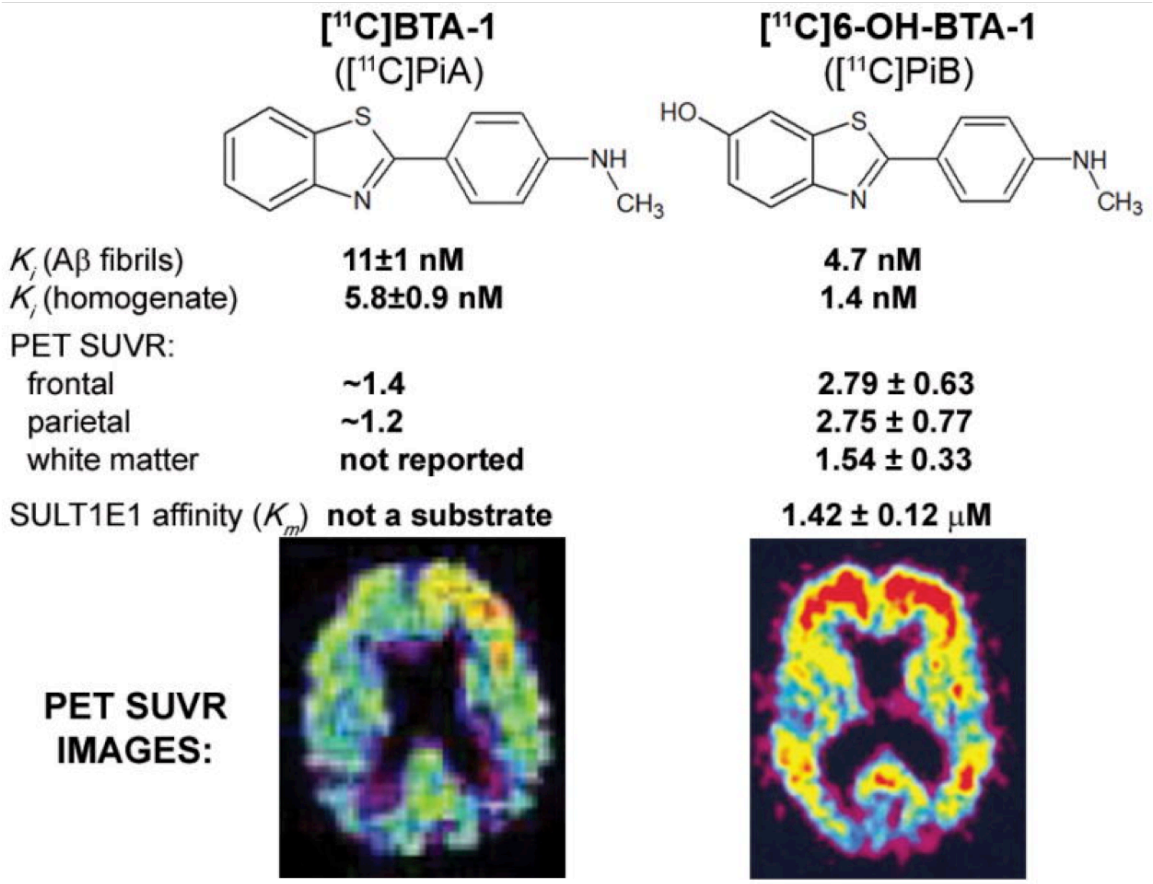

Kepe V, *et al*. *J Alzheimers Dis*. 2013 Jan 1; 36(4): 613–631.

A comparison between [^{11}C]-PiA and [^{11}C]-PiB shows a different pattern of uptake. [^{11}C]-PiA uptake in the cortical tissue is significantly less, and its uptake in the white matter bears no literature value. The absence of a phenolic group in [^{11}C]-PiA does not make it a valid substrate for SULT1E1, unlike [^{11}C]-PiB.

Quantitative surveillance of SULT1E1 in human tissue is possible through imaging with Positron Emission Tomography (PET) by using 2-(4'-[^{11}C]methylaminophenyl)-6-hydroxybenzothiazole, also known as Pittsburgh Compound B or [^{11}C]-PiB. Since SULT1E1 has demonstrable variation in response to inflammation through estrogen metabolism, it is reasonable to anticipate dynamic signal from [^{11}C]-PiB PET imaging resulting on account of inflammatory responses in hypoperfused tissue of moyamoya patients, which is the rationale for our study.

3.2 - [^{11}C]-PiB SRTM DVR in Moyamoya Syndrome

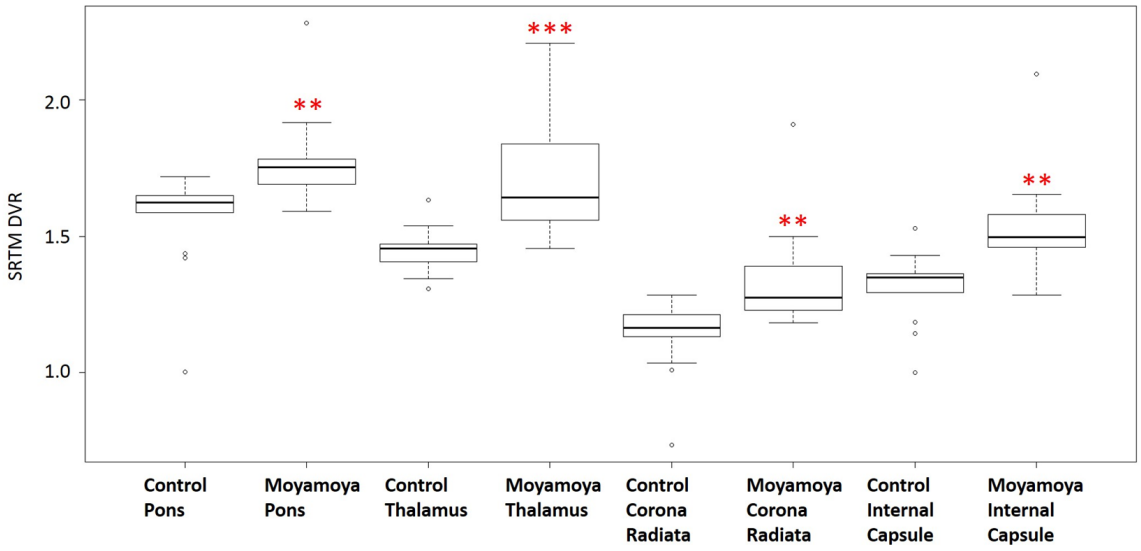

	Pons	Thalamus	Corona Radiata	Internal Capsule
Moyamoya Cohort SRTM DVR Mean	1.79 ± 0.06	1.74 ± 0.08	1.35 ± 0.07	1.55 ± 0.07
Control Cohort SRTM DVR Mean	1.56 ± 0.05	1.45 ± 0.02	1.13 ± 0.04	1.31 ± 0.04
Wilcoxon Test Two-Sided p-Value	2.54×10^{-3}	3.39×10^{-4}	1.15×10^{-3}	1.51×10^{-3}
Kruskal-Wallis Test p-Value	3.56×10^{-3}	8.11×10^{-4}	1.93×10^{-3}	2.38×10^{-3}

All means reported ± standard error. Moyamoya and Control Cohorts (n=10 and n=13, respectively).

Figure 3.2: Regions of Prominent [^{11}C]-PiB Uptake in Moyamoya Patients
*A boxplot figure and summary table of brain regions within moyamoya syndrome cohort whose [^{11}C]-PiB signal is significantly greater than corresponding regions in the Control cohort. Mean [^{11}C]-PiB signals are presented +/- standard error for each cohort and produced statistically significant differences resulting from the Wilcoxon and Kruskal-Wallis tests with p<0.01 and p<0.001 (** and ***, respectively).*

Figure 3.2 depicts uptake of [^{11}C]-PiB in regions that achieved a statistically significant difference between the moyamoya cohort and the control cohort. Although age in the moyamoya cohort had a larger range than among the control patients, the relationship between age and differences in [^{11}C]-PiB signal, as dictated by the Friedman test, between the two cohorts achieved a non-significant p-value (p>0.08). The presence of significant differences (p<0.01), however, was prominent and elevated in the corona radiata, thalamus, internal capsule and pons. Strong midbrain and subcortical signal in particular demonstrated both high SRTM DVR values and a coordinated response in moyamoya cases. Thalamic [^{11}C]-PiB uptake in moyamoya patients had strong correlations with [^{11}C]-PiB uptake in the internal capsule and pons (Spearman ρ=0.891 and ρ=0.879, respectively, where p<0.01) that were not observed in the controls (Spearman ρ=0.577 and ρ=0.533, respectively, where p=0.085).

The regions from Moyamoya patients in Figure 3.2 with prominent [^{11}C]-PiB uptake that differed with the control patients have been previously established to be regions with high aromatase expression. The concurrent presence of SULT1E1 and aromatase within invasive lobular carcinoma specimens, for example, supports aromatase dependent estrogen synthesis within these tumors (Takagi *et al.*, 2016). SULT1E1 regulates the availability of estrogen, thus making colocalization with aromatase a likely possibility. PET imaging with the radiolabeled aromatase inhibitor [^{11}C]-Vorozole has identified the pons and thalamus to possess significantly elevated binding potentials (Logan *et al.*, 2014). Hence, [^{11}C]-PiB binding in the same brain regions where aromatase activity was previously detected with [^{11}C]-Vorozole verifies the capacity of brain to metabolize estrogen.

Elevated [^{11}C]-PiB thalamic binding, in particular, exemplifies how inflammation resulting from microstructural changes. Studies with transient ischemia have also documented thalamic cell death (Lin *et al.*, 1990). In addition to reduced cerebral blood flow when compared to controls, differential kurtosis MRI evaluation of the thalamus after mild traumatic brain injury also confirmed decreased mean kurtosis, which confers microstructural changes in axonal and myelin density (Grossman *et al.*, 2013). Heightened SULT1E1 activity witnessed in the pons, thalamus, corona radiata and internal capsule exhibit regulatory mechanisms controlling estrogen availability in response to tissue damage from chronic hypoperfusion.

Chronic hypoperfusion from inadequate flow in white matter and subcortical structures exhibit damage that is verifiable with imaging. Differential kurtosis and differential tensor (DKI and DTI, respectively) MRI confirmed microstructural changes within the corona radiata and thalamus of moyamoya patients that reflect both demyelination and axonal loss (Kazumata *et al.*, 2016). Demyelination, as confirmed by increasing radial diffusivity (RD), has also been seen in conjunction with amyloid precursor protein (APP) (Song *et al.*, 2005). While a precursor for Aß, APP can also be expressed in response to DNA damage (Minopoli *et al.*, 2007). [^{11}C]-PiB affinity for APP is drastically lower when compared to Aß plaques (Klunk *et al.*, 2005). Hong and colleagues found APP and Aß expression in the white matter of patients with traumatic brain injury that coincided with a transient [^{11}C]-PiB signal in subcortical and midbrain structures (Hong *et al.*, 2014). This study, however, failed to match [^{11}C]-PiB PET signal with autoradiography in white matter from autopsy tissue using [^{3}H]-PiB. SULT1E1 in autopsy tissue fails to have activity, which explains the disparity between PET and ex-

vivo results. Additionally, the study used patients who passed within 3 hours to 56 days of a traumatic brain injury to detect axonal Aß. White matter Aß lacks the density of cortical Aß plaques and is principally primitive in formation (Iwamoto *et al.*, 1997). Nihashi and colleagues established that Aß formation from APP in response to transient ischemia dissipates within 60 days of the insult (Nihashi *et al.*, 2001). APP cleavage mediated by estradiol also averts beta and gamma secretory processes (Jaffe *et al.*, 1994). Therefore, heightened estrogen turnover by SULT1E1 in response to APP cleavage is consistent with elevated [^{11}C]-PiB retention in regions suffering from hypoperfusion.

Moyamoya syndrome is a progressive cerebrovascular condition rising from arterial stenosis that gives rise to a network of collateral vessels. The degree of stenosis may be relatively constant over time, yet the degree of inflammation from the vasculopathy will vary. Moyamoya syndrome encompasses moyamoya disease, where stenosis of the internal carotid arteries gives rise to a network of collateral vessels (Suzuki and Takaku, 1969). Occlusion of the internal carotid arteries (ICA) results from intimal thickening that is a consequence of vascular smooth muscle cells (VSMCs) migrating from the medial wall. Stenosis within the ICA gradually causes the Circle of Willis to occlude with the anterior and middle cerebral arteries particularly vulnerable. In the subsequent stages of moyamoya disease, the brain relies on a network of collateral vessels that ultimately divert from the ICA to the external carotid artery (ECA). The branching pattern of the collateral vessels from the basal ganglia on an arteriogram resembles a “puff of smoke,” which is the translation for the name of the disease (もやもや, or Moyamoya). The progressive diversion of cerebrovascular flow that utilizes collateral vessels facilitates chronic hypoperfusion.

The patterned leptomeningeal vessels provide collateral flow in response to arterial stenosis. The basal ganglia and white matter in particular, however, bear vulnerability to impaired flow from these leptomeningeal vessels that constitute the moyamoya collateralization. Chronic ischemia in moyamoya leaves white matter more susceptible to changes than grey matter with microstructural changes that reflect axonal loss, demyelination and even cognitive impairment (Kazumata *et al.*, 2015). Moreover, plasma samples from patients with moyamoya disease have confirmed cytokines and MMPs, whose role has been previously established to be destructive to white matter in vascular dementia (Rosenberg *et al.*, 2001; Kang *et al.*, 2010). Prior reports suggest that the inflammatory nature of the moyamoya microenvironment is associated with angiogenesis and endothelial interactions seen in VSMCs (Ohkubo *et al.*, 2015). Reports of normally appearing white matter in moyamoya patients demonstrate elevated apparent diffusion coefficient (ADC) values are associated with executive dysfunction in adults (Calviere *et al.*, 2010; Calviere *et al.*, 2012; Nakamizo *et al.*, 2014). Hence, microstructural changes within white matter and deep brain structures from impaired flow in moyamoya patients present important questions regarding responses to inflammation.

It is also imperative to emphasize that moyamoya syndrome is not an amyloid mediated disease. There is no known report that confirms the existence of Aß in moyamoya. Unlike using [^{11}C]-PiB to image patients with Alzheimer's Disease, the signal witnessed from moyamoya patients has contribution from amyloid beta (Aß) plaques. The median age of the moyamoya cohort within the study is 44.7 years, while the lower and upper limits are 27.0 and 76.9 years. The inclusion of the 76.9 year-old

moyamoya patient introduces the possibility that [^{11}C]-PiB signal from this patient may also reflect amyloid deposition associated with aging. While this patient lacked a history of dementia at the time of imaging, the heightened DVR values from this older patient may appear conspicuous, particularly as they contribute to aggregate differences over control patients. The frontal grey matter DVR value of 1.82 in this patient was less than in the corona radiata, thalamus, internal capsule, and pons (1.91, 2.10, 2.09, and 1.92, respectively). The frontal grey matter DVR, however, was less than the frontal white matter DVR of 2.00. [^{11}C]-PiB uptake in white matter of patients with Alzheimer's Disease is characteristically lower than cortical tissue (Fodero-Tavoletti *et al.*, 2009). White matter throughout the entire moyamoya cohort had higher [^{11}C]-PiB retention than cortical tissue both at the regional and global levels. White matter, therefore, exemplifies how heightened inflammatory responses in hemodynamically unstable tissue resulted from cerebrovascular insults and not Aß. The chronically ischemic subcortical and midbrain regions featured in Figure 3.2 do not share the same pathology as cortical tissue in Alzheimer's Disease. Amyloid deposition noted in subcortical and midbrain structures does not transpire until later phases of Alzheimer's Disease and has a lower density than found in cortical tissue (Braak and Braak, 1991; Thal *et al.*, 2002). The patients within this cohort have histories of cerebrovascular insufficiency at ages that are predominantly younger than patients with Alzheimer's Disease. The justification of Aß as the target for the [^{11}C]-PiB signal in this study, therefore, is not plausible on account of the location and magnitude of uptake and the overall demographics of the patient cohort.

3.3 – Inflammatory Stimuli Producing [^{11}C]-PiB Signal in Moyamoya Patients

In Figure 3.3, the restricted diffusion constituting the "ivy-sign" on DWI and dense vascular bundle seen on contrast-enhanced T1 MRIs indicate moyamoya collateral vessels associated with reduced flow in the disease. Heightened [^{11}C]-PiB accumulation, however, is peripheral to these vessels. The thalamus and pons retained elevated [^{11}C]-PiB, particularly when compared to an age-matched control patient.

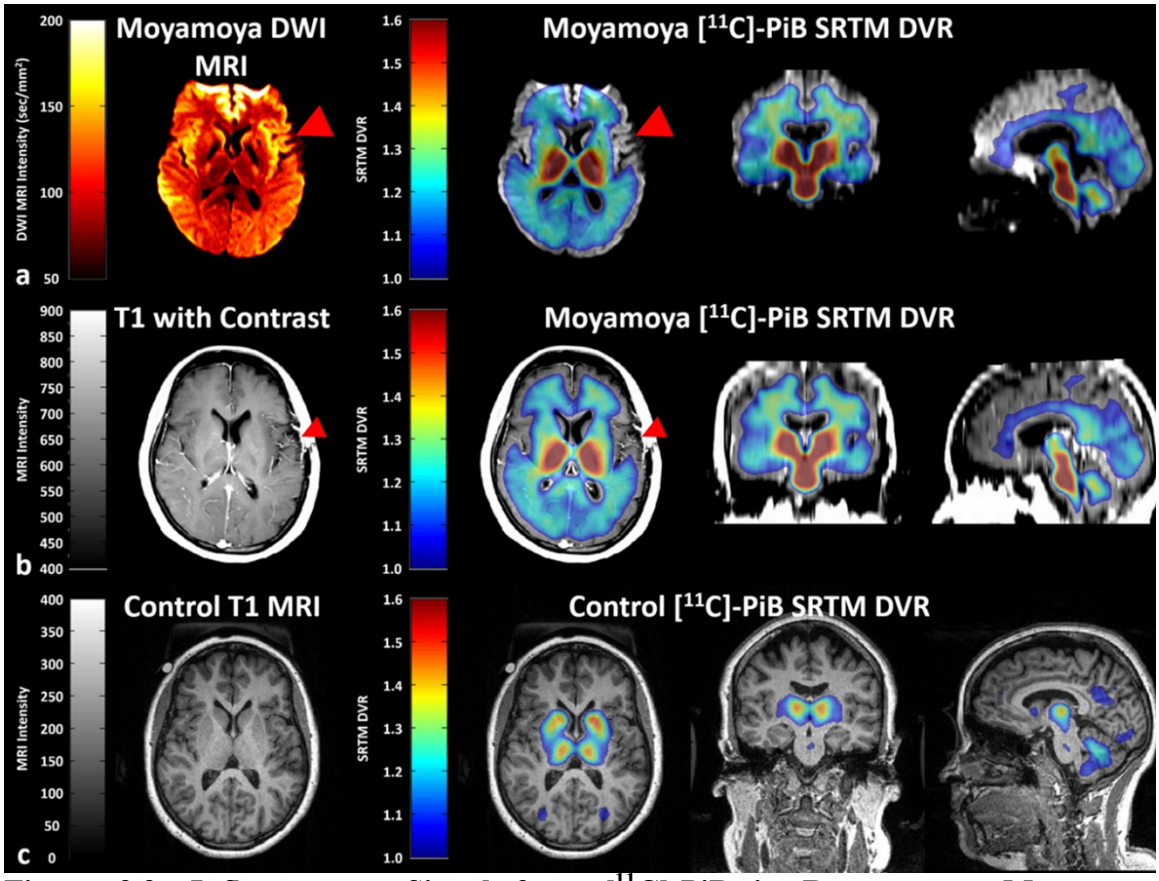

Figure 3.3: Inflammatory Signal from [^{11}C]-PiB in Response to Moyamoya Collateralization

Red arrows highlight moyamoya collateral vessels manifested by restricted diffusion and vascular density in the left basal ganglia of the DWI and T1 post-contrast scans in a 33.4-year old female patient (a and b, respectively). A T1 MRI with a normal appearance from a 34.3-year old female patient (c). Coregistered [^{11}C]-PiB scans for the moyamoya patient show no uptake at the site of the moyamoya vessels yet ostensibly elevated thalamic and pontine uptake compared to the control, whose uptake in these regions is notably lower.

In Figure 3.4, this moyamoya patient with a ventriculoperitoneal (VP) shunt presents severe trauma and tissue damage that is reflected by elevated diffusion in the ADC MRI; the same patient exhibits notably lower ADC values in the basal ganglia and periventricular area that are indicative of ischemia there. [^{11}C]-PiB signal in this patient, however, remains exceptionally elevated in the basal ganglia, subcortical, midbrain structures and white matter, particularly when contrasted against a similarly aged control patient, as these areas border tissue with ischemic damage.

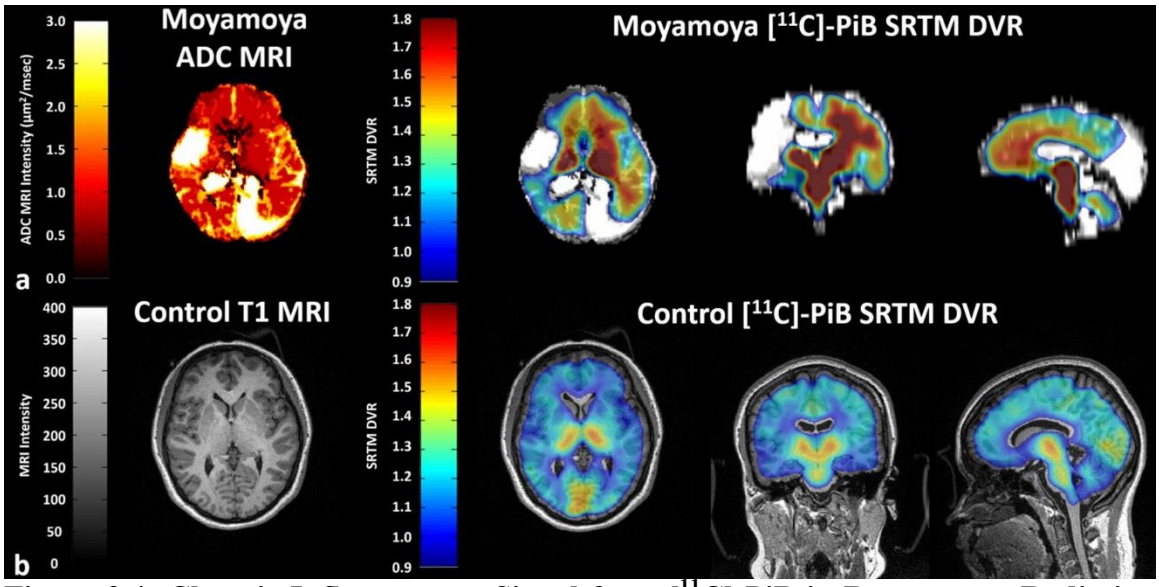

Figure 3.4: Chronic Inflammatory Signal from [^{11}C]-PiB in Response to Radiation in Moyamoya Patient

A 27.0 year-old female patient with moyamoya syndrome received a ventriculoperitoneal shunt and endured significant trauma to the brain, as featured in ADC MRI (a). A 23.5 year-old female control has a T1 MRI with a healthy appearance (b). Coregistered [^{11}C]-PiB scans in both patients show that the moyamoya patients demonstrates profound retention in the basal ganglia and white matter, whose corresponding uptake in the control patient is notably less by comparison.

What is of paramount importance about these cases is the age of these patients. The magnitude of the [^{11}C]-PiB signal achieved in these scans can easily match MCI for Figure 3.3 at 34.3 years old and AD for Figure 3.4 and 27.0 years old, yet the location of tracer retention is distinctly different from neurodegenerative diseases such as

Alzheimer's Disease. [^{11}C]-PiB images in Figures 4.3 and 4.4 illustrate different presentations of moyamoya syndrome that ultimately reflect chronic ischemia. The presentation of cerebrovascular disease elucidates inflammatory patterns seen by [^{11}C]-PiB in areas that border vessel formation and tissue damage in two different moyamoya cases. Both aforementioned cases have a history of moyamoya syndrome and display subcortical and midbrain retention, which is consistent with inherently high inflammatory profiles resulting from moyamoya.

The patient in Figure 3.3 (Moyamoya 3) presented with Cushing syndrome and an indirect revascularization procedure. Postoperative hyperperfusion following a revascularization procedure can jeopardize tissue that is already hemodynamically unstable. Axonal damage, myelin degeneration and even interstitial edema can contribute to reduced white matter integrity, particularly in the internal capsule and in the pyramidal tract, after revascularization (Kazumata *et al.*, 2016c). Pronounced [^{11}C]-PiB uptake in the pons within this patient validates inflammatory responses from microstructural changes reported along the pyramidal tract.

The patient in Figure 3.4 (Moyamoya1) presented with a long history that included a diagnosis for moyamoya syndrome since the age of two. At the time of imaging at 27 years old, the patient also had hydrocephalus, which is quite pronounced on ADC MRI. This patient had an astrocytoma as a child and suffered from a radiation-induced vasculopathy resulting in systemic and chronic stenosis. Pediatric patients, particularly under the age of five, can face long-term morbidity from occlusive cerebral vasculopathy following radiation (Desai *et al.*, 2006). Visualization of radiation-induced atheritis confirms wall enhancement and a ring formation in affected cerebral vessels on

MRI imaging (Aoki *et al.*, 2002). A therapeutic regimen including radiation and chemotherapy engenders inflammation that can lead to fibrosis and consequently stenosis in cerebral vessels (Mitchell *et al.*, 1991; Campen *et al.*, 2012). The severity of stenosis in this patient affected both the ICA and MCA and caused a lifetime of cerebrovascular instability.

Chronic hypoperfusion in the brain gives rise to astrogliosis, neuronal death and cognitive impairment (Cechetti *et al.*, 2012). Throughout the stages of moyamoya syndrome, occlusion of the internal carotid arteries and the Circle of Willis as well as branching collateral vessels impairs cerebrovascular flow and establishes chronic ischemia, which subsequently gives rise to cognitive impairment. The resonating patterns seen in patients with a defined moyamoya collateralization and an acute infarct are the sequestration of [^{11}C]-PiB in subcortical and midbrain structures that border hemodynamic insults presented by these conditions. The moyamoya collateralization in Figure 3.3 defined on DWI and gadolinium contrast T1 MRI has nominal [^{11}C]-PiB uptake, whereas the thalamic and pontine uptake are notably higher than the control counterpart. Similarly, tissue with elevated ADC in Figure 3.4 from an acute infarct shows significantly less uptake than the subcortical white matter and midbrain structures that border diminished ADC in the basal ganglia and periventricular areas. Diminished ADC reflects ischemic lesions in ischemic stroke, whereas heightened ADC in tissue can reflect axonal loss (van Everdingen *et al.*, 1998; Helenius *et al.*, 2002). Subcortical and midbrain regions bordering ischemic lesions and damaged tissue endure inflammatory signaling from astrogliosis. Regions that experience microstructural changes from hypoperfusion, therefore, can experience cytokine surges and, subsequently, elevated

[^{11}C]-PiB uptake. It is within these same regions where moyamoya vessels jeopardize hemodynamic flow.

The arterial zones that transition into the capillary beds within the white matter are rich with glial cells. Astrocytes in particular provide a cellular link to neurons and have endfeet that with the basal lamina to surround endothelial capillary cells that form the blood-brain barrier (Abbott *et al.*, 2006). Astrocytes are responsible for adjusting cerebral blood flow with neuronal synaptic activity by using prostaglandins, epoxyeicosatrienoic acids (EETs), arachidonic acid, potassium ions to communicate with vascular smooth muscle and increase blood flow when stimulated (Koehler *et al.*, 2006). Astrocytes also mediate inflammatory responses that regulate permeability in the blood-brain barrier. Specifically, endothelin-1, a vasoconstrictor found in ischemic stroke, will stimulate IL-1 β production in astrocytes that will increase blood-brain barrier permeability (Didier *et al.*, 2003). In conjunction with microglial cells and oligodendrocytes, astrocytes release increasing amounts of IL-1 β over time in response to ischemia and have intensified amounts released in the white matter (Sairanen *et al.*, 1997). Astrocytes, therefore, provide an inflammatory response that is linked to cerebral blood flow.

Interleukin-1 β (IL-1 β) is not the only cytokine found in the onset of ischemic stroke and blood-brain barrier breakdown, but it has a potent effect on the pathophysiology of vascular disease. IL-1 β is a pro-inflammatory cytokine released from VSMCs that enhances atherosclerotic progression by promoting cell growth (Moyer *et al.*, 1991; Ross, 1999). IL-1 β is capable of inducing VSMC secretion of Platelet Derived Growth Factor, which enhances cell proliferation (Raines *et al.*, 1989). In a porcine

coronary arterial model, IL-1 β induction effected histological and functional changes from PDGF-mediated intimal thickening and vasospactic responses (Shimokawa *et al.*, 1996). IL-1 β increases vascular permeability and decreases vascular tone by stimulating cyclooxygenase-2 activation and increased prostaglandin E2 secretion in moyamoya smooth muscle cells, while nitric oxide production remains unchanged from control cells (COX-2 and PGE_2, respectively; Yamamoto *et al.*, 1998). Elevated IL-1 β levels in moyamoya are responsible for inflammatory actions that participate with many growth factors. IL-1 β is reported to enhance the activity of matrix metalloproteinases (MMPs) that remodel interstitial collagen in cardiac fibroblasts (Siwik *et al.*, 2000). More importantly, however, IL-1 β inhibits STS expression and activity and accelerates SULT1E1 expression in human aortic VMSCs with atherosclerosis (Nakamura *et al.*, 2003). Pro-inflammatory cytokines found in vascular diseases highlight the impact of estrogen metabolism. IL-1 β itself cannot exclusively explain the changes seen in vascular disease and moyamoya, but it is a critical inflammatory stimulus from the glial microenvironment. Higher levels of cytokines necessitate a higher availability of estrogen and subsequently increase SULT1E1 activity. Elevated SULT1E1 expression resulting from heightened cytokines enables SULT1E1 imaging with [^{11}C]-PiB to reflect the role of inflammation in vascular diseases.

The metabolic profile of estrogen is variable in response to tissue damage from stroke and ischemia. Astrocytes and neurons produce estradiol and estrone locally (Zwain and Yen, 1999). Estrogen synthesis from activated astrocytes is seen with enhanced aromatase expression in a model of traumatic brain injury (Gatson *et al.*, 2011). Estrogen has neuroprotective abilities that can equilibrate effects from elevated cytokines (Straub,

2007). Merlo and Sortino verified increased neuronal expression of both MMP-2 and MMP-9, which degraded Aß after exposure to estradiol (Merlo and Sortino, 2012). With elevated cytokine levels in moyamoya, SULT1E1 expression and activity will increase in turn and justify [^{11}C]-PiB imaging with PET as an appropriate method to monitor inflammation in the disease.

Astrogliosis causes a surge in the number of activated astrocytes and results from chronic ischemic conditions. Moyamoya vessels produce inadequate flow that sustains hemodynamic instability. The distribution of incompetent perfusion threatens deep white matter and subcortical structures with microstructural changes from demyelination and axonal loss. The formation of reactive astrocytes introduces accumulation of matrix metalloproteinases that impact the integrity of the blood-brain barrier (Rosenberg *et al.*, 1998; Rosenberg *et al.*, 2001). Activated astrocytic populations have elevated matrix metalloproteinase expression (Muir *et al.*, 2002). Similarly, the serum of moyamoya patients contains elevated levels of matrix metalloproteinase 9 (MMP-9) (Fujimura *et al.*, 2009). The involvement of MMP-9 and other matrix metalloproteinases in the deterioration of the blood-brain barrier can contribute to microstructural changes and subsequent inflammation in moyamoya.

These resulting changes have not yet been fully characterized but have associations with immune modifications seen in moyamoya. Upon investigation after autopsy, intracranial occlusive lesions of moyamoya patients displayed T cell and macrophage infiltration independently of microthrombi (Masuda *et al.*, 1993). The presence of elevated thyroid autoantibodies and autoimmune disease with moyamoya suggests compromised immunity. Additionally, RNF213 deficient mice demonstrated

suppressed FOXP3+ cell circulation in response to immunogenic stimuli, thus suggesting polymorphisms of the gene may compromise immune safeguards against self-recognition (Kanoke *et al.*, 2016). Collectively, these observations establish moyamoya to involve aberrant immune activity that contributes to the inflammatory nature of the disease.

It is necessary to emphasize that estrogen can also participate in T cell mediated inflammation. IFN-γ is an inflammatory cytokine produced by T cells that stimulates Th1 T cell activity and hinders remyelination (Lin *et al.*, 2006). In autoimmune diseases, such as multiple sclerosis, IFN-γ has been reported to have enhanced natural killer activity and caused relapses (Panitch *et al.*, 1987). Estrogen can increase the IFN-γ receptor expression on estrogen receptor positive lymphocytes and IFN-γ production from natural killer cells (Fox *et al.*, 1991; Nakaya *et al.*, 2006). T cells from patients with thyroid autoantibodies produce elevated IFN-γ (Karanikas *et al.*, 2005). Additionally, thyroid autoantibodies are elevated in adult patients with moyamoya disease and intracranial stenosis (Kim *et al.*, 2010; Shi *et al.*, 2014). T cell signaling in moyamoya syndrome may, therefore, shift demand on the availability of estrogen and also cause higher SULT1E1 activity.

3.4 - Dynamic [^{11}C]-PiB Signal in White Matter of Multiple Sclerosis

Figure 3.5 features a patient with multiple sclerosis whose [^{11}C]-PiB signal changed with therapy suppressing immune responses to demyelination. Figure 3.5a shows the patient's T1 MRI, where visualization of demyelinating processes is not evident. Figure 3.5b, however, shows a pre-treatment [^{11}C]-PiB scan that highlights active demyelination in both white matter and basal ganglia. Within one month of initiating steroidal therapy, Figure 3.5c presents notable decrease of [^{11}C]-PiB uptake in

the same patient. Among decreases in many regions, the patient's right ventral pallidum demonstrated a 34.3% drop in [^{11}C]-PiB uptake. In the pre-treatment scan, the ventral pallidum itself displayed visible demyelinating and axonal loss processes that effected 34.9% asymmetry between the right and left ventral pallidum, whereas as asymmetry fell to 3.66% in the post-treatment scan. The resulting changes from therapeutic intervention against inflammation, therefore, caused [^{11}C]-PiB uptake to decrease in regions where inflammation from tissue damage was heightened previously. The corona radiata, thalamus, internal capsule and pons also demonstrated decreases in [^{11}C]-PiB uptake after therapy (30.0%, 14.7%, 16.7%, and 8.27% reduction, respectively).

Multiple sclerosis (MS) is a disease that targets white matter. Autoimmune demyelination and axonal loss in MS reflect inflammatory signaling cascades in white matter (Honma *et al.*, 2002). Neither myelin nor oligodendrocytes express MHC II molecules for recognition by T cell receptors (Lee and Raine, 1989). Reactive microglia are critical for T cell migration across the blood-brain barrier before the formation of MS plaques. Coordination among T cells, astrocytes and microglia facilitates demyelination in MS through pro-inflammatory cytokines and adhesions molecules. Adhesions molecules, such as intracellular adhesion molecule-1 (ICAM-1), achieve elevated levels on the surface of reactive microglia within lesions and can act as antigen presenting cells to $CD4^+$ T cells (Williams *et al.*, 1993). Upon presentation of MHC II molecules to $CD-4^+$ T cells by reactive microglia, T cells secrete IFN-γ, which amplifies Th1 T cell recruitment, microglia activation and proinflammatory cytokine production (Minagar *et al.*, 2002). Reactive microglia are an abundant source of cytokines that participate in neuronal damage and signaling with astrocytes. In MS lesions, IL-1ß expression is

predominant on account of microglia throughout white matter, yet TNF-α expression is within microglial cells outside of lesions, foamy microglia/macrophages within lesions and blood vessels and astrocytes (Cannella and Raine, 1995). Despite their susceptibility to produce destructive cytokines and participation in astrogliosis, astrocytes are also a source of growth factors and prostaglandins that inhibit Th1 T cell proliferation and downregulation of microglia (Meinl *et al.*, 1994; Xiao and Link, 1999). Ultimately, however, cytokine-mediated inflammation governs concerted action among microglia, T cells and astrocytes in the MS microenvironment that causes demyelination.

As chromic ischemia in moyamoya syndrome, demyelinating processes in MS entail inflammatory insults. White matter is the principal target, yet subcortical structures are also vulnerable. Demyelinating lesions have also been reported within the thalamus of multiple sclerosis that can affect cognitive and motor function (Vercellino *et al.*, 2009; Minagar *et al.*, 2013). In earlier phases of the disease, APP accumulation in acute lesions result from failed axonal transport and represents both inflammation and demyelination (Ferguson *et al.*, 1997). In MS, APP coexists with axonal damage, such as demyelination, and is correlated by cytotoxic T-cell migration and microglial activation (Bitsch *et al.*, 2000; Kuhlmann *et al.*, 2002; Smith *et al.*, 2003). Estrogen has many roles that can respond to inflammation from the demyelinating processes, which is why its availability is critical in the brain of an MS patient.

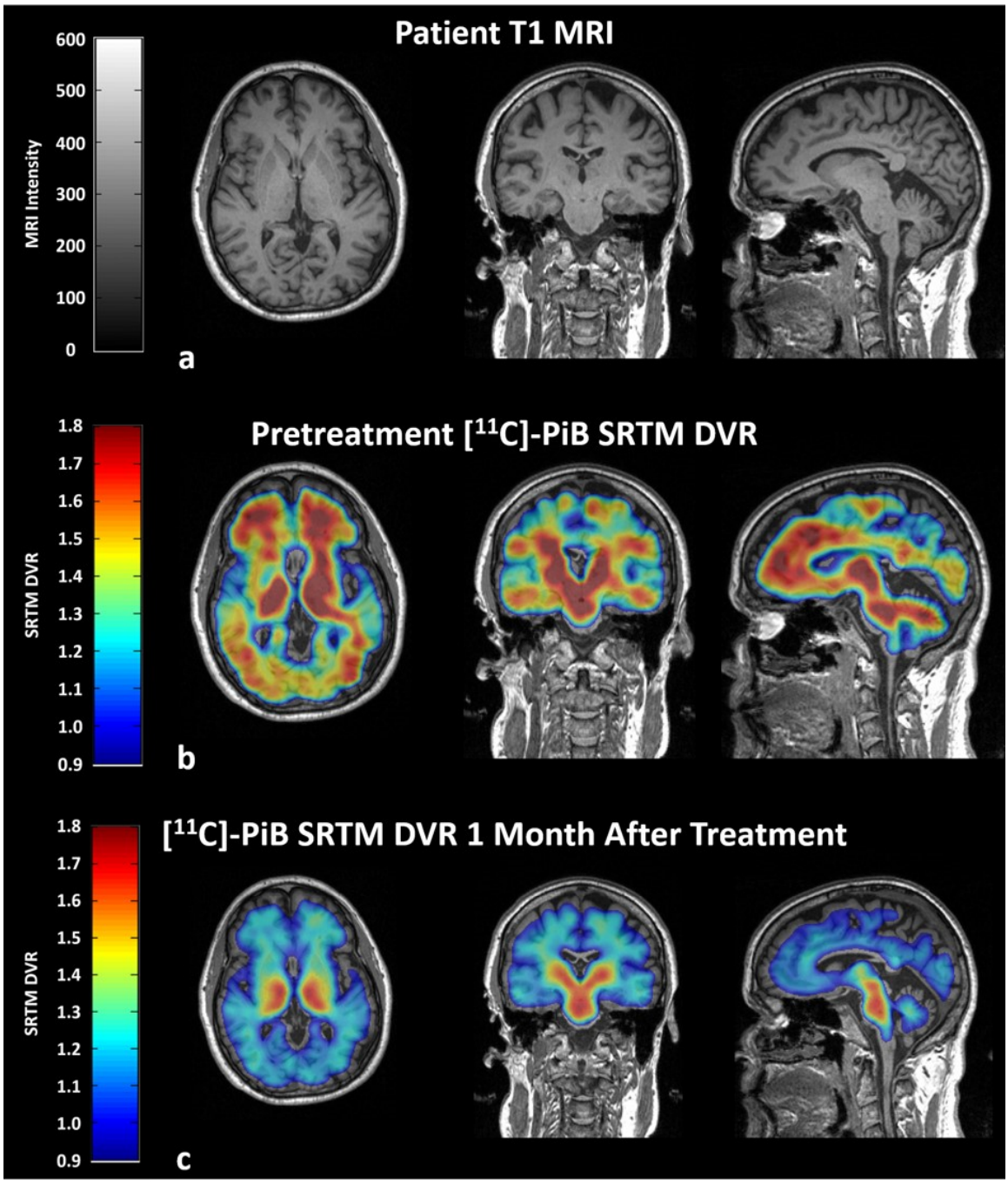

Figure 3.5: Dynamic SULT1E1 Response in White Matter of Multiple Sclerosis
A 50.3 year-old male patient with relapse-remitting multiple sclerosis has a T1 MRI scan that does not portray visible white matter damage. (a). Coregistered [^{11}C]-PiB scans before and one month after steroidal therapy demonstrate a dramatic reduction in [^{11}C]-PiB signal (b and c, respectively).

The MS patient in Figure 3.5 demonstrated responsive estrogen metabolism in white matter. After administration of prednisone, the signal that previously outlined demyelination in the basal ganglia dropped significantly. Prior literature documenting [^{11}C]-PiB imaging of multiple sclerosis in humans and baboons presented evidence for myelin binding protein (MBP) as the target (Stankoff *et al.*, 2011). The present results, however, do not support this conclusion. The patient's response to therapy illustrates a rather dynamic profile within one month of therapy. Prior to administration of interferon-β, the patient is Figure 3.5 had profound [^{11}C]-PiB retention in both white matter and subcortical structures in a similar magnitude to the patient in Figure 3.4. After treatment, the right ventral pallidum [^{11}C]-PiB signal fell 34.3%. Post-treatment reductions in SRTM DVR for the corona radiata, thalamus, internal capsule and pons were also 30.0%, 14.7%, 16.7%, and 8.27%, respectively. Neither Aß plaques nor MBP would dissipate so precipitously within one month. Interestingly, the immunomodulatory behavior of interferon-β may explain the [^{11}C]-PiB signal seen in these multiple sclerosis images. Interferon-β and methylprednisolone can inhibit T-cell trafficking through areas of broken blood-brain barrier, which confers benefit for multiple sclerosis and lowers inflammation. The diminished [^{11}C]-PiB signal after combined treatment with interferon-β and methylprednisolone, therefore, corroborates suppressed inflammation.

Reduction of inflammation by steroids suppresses cytokine-mediated inflammation, which is consistent with reports of diminished cytokines with lower SULT1E1 expression (Xu *et al.*, 2013). The combination of interferon-β and intravenous methylprednisolone has demonstrated reduction of tissue damage in relapse-remitting multiple sclerosis (Richert *et al.*, 2001). Methylprednisolone itself is effective against T-

cell activation and proliferation (Airla *et al.*, 2004). The suppression of T cell trafficking mitigates the inflammatory cascades that propagate autoimmune attacks in MS. Consequently, the demand for estrogen reduces and SULT1E1 activity is lower in the presence of diminished cytokine signaling. Similar to moyamoya syndrome, MS produces no Aß plaques. Additionally, MS patients also have elevated thyroid autoantibodies but in earlier stages of the disease (Annunziata *et al.*, 1999). The genuine impetus behind autoimmune behavior, however, in MS is the surge in reactive microglia. Their activation in an inflammatory environment stimulates T cell proliferation to attack oligodendrocytes and myelin that lack recognition molecules for T cell receptors. The changes from immunomodulatory therapy presented in this figure, therefore, substantiate a dynamic [^{11}C]-PiB signal that varies with disease-related inflammation.

SULT1E1 modulates the availability of estrogen, equilibrates cytokine-mediated responses and also has correlations with other molecules and pathways that govern inflammatory pathways. Inactivated estrogens during adipogenesis in human adipocytes confirmed elevated SULT1E1 and peroxisome proliferator-activated receptor gamma (PPAR-γ) expression that was inhibited by pharmacological inhibition of SULT1E1 with triclosan and genetic knockdown of SULT1E1 (Ihunnah *et al.*, 2014). PPAR-γ is involved with lipid metabolism and insulin sensitization yet also influences cytokine production. Rat cortical astrocytes pretreated with estradiol for 48 hours received exposure to Aß for 24 hours displayed decreased iNOS, IL-1ß, and TNF-α yet an increase in PPAR-γ expression (Valles *et al.*, 2010). PPAR-γ and estrogen metabolism, therefore, participate synergistically in alleviating inflammatory insults.

PPAR-γ is also a negative regulator of macrophage activation and inflammatory pathways. PPAR-γ is markedly upregulated in activated macrophages, and both endogenous and synthetic PPAR-γ agonists inhibit expression of inducible nitric oxide synthase (iNOS), MMP-9, scavenger A receptor, AP-1, STAT and NF-κß (Ricote *et al.*, 1998). In an MCAO model, administration of PPAR-γ agonist pioglitazone 5 days before and 2 days after MCAO attenuated neuronal COX-2 expression, reduced infarct size, and suppressed pro-inflammatory cytokines such as TNF-α (Zhao *et al.*, 2006). Moreover, the same study identified PPAR-γ expression in microglial cells within the peri-infarct area. Murine microglia isolated from an intracerebral hemorrhage model treated with the PPAR-γ agonist rosiglitazone demonstrated more efficient phagocytosis of hematoma, reduced expression of cytokines (iNOS, TNF-α, and IL-1ß), decreased neuronal damage, increased PPAR-γ regulatory genes (catalase and CD 36), and improved functional recovery of the mouse (Zhao *et al.*, 2007). Additionally, human and murine CD4 and CD8 T cells express PPAR-γ and demonstrate repression of IFN-γ in the presence of PPAR-γ agonists (Cunard *et al.*, 2004). Endothelial cells stimulated with IFN-γ stimulated endothelial cells witnessed inhibition of chemokine release and attenuation of Th1 cell recruitment after exposure to PPAR-γ agonists (Marx *et al.*, 2000). Stimulation of PPAR-γ pathway with synthetic and endogenous PPAR-γ agonists demonstrates suppression of pro-inflammatory cytokine proliferation and T cell recruitment. The PPAR-γ mediated intervention demonstrated parallel action to estrogen, thus suggesting coordination between the two molecules against inflammatory consequences of disease.

These results demonstrate how SULT1E1 can achieve elevated expression in diseases that produce an inflammatory environment in the brain. The formation of an astroglial scar in a focal ischemic lesion model, chronic hypoperfusion in patients with moyamoya syndrome, and demyelination in multiple sclerosis exemplified exceptional inflammation in regions with high [^{11}C]-PiB accumulation. Regions with substantially elevated [^{11}C]-PiB SRTM DVR are not replete with Aß plaques, thus questioning whether Aß drives the resulting signal. Although a precise mechanism for the response of SULT1E1 to insults in the brain cannot be established from the data within this report, the signal witnessed in both animals and patients within this study result from the regulatory metabolism of estrogen. Therefore, the [^{11}C]-PiB signal discussed in this paper is indicative of estrogen consumption responding to pathophysiological cues from ischemic and autoimmune conditions.

The results presented in this work are the first report of using PET to image estrogen sulfotransferase in humans. Moreover, this is the first report of [^{11}C]-PiB images in patients with moyamoya syndrome. Fundamentally, these imaging studies produced a potent signal using [^{11}C]-PiB in patients with diseases that lack Aß. Prior demonstrations of [^{11}C]-PiB signals unrelated to Aß plaques involved case reports of meningioma in patients with no prior history of dementia or psychiatric illness. Two reports confirm patent MRI visualization of tumors that display elevated and confined [^{11}C]-PiB uptake within the tumor itself (Kim *et al.*, 2012; Yamamoto *et al.*, 2013). A more recent report in 2015 involved two patients possessing a history of mild cognitive impairment that presented meningioma with [^{11}C]-PiB uptake, yet these same tumors were not [^{18}F]-FDG avid (Chaves *et al.*, 2015). COX-2 overexpression and pro-inflammatory signaling from

prostaglandins stimulate tumor proliferation in meningiomas (Kato *et al.*, 2014). Furthermore, meningioma tissue from patients that produced [^{11}C]-PiB uptake failed to validate the presence of Aß (Johnson *et al.*, 2012). Hence, these observations concerning meningioma corroborate the conclusion that [^{11}C]-PiB signal is not exclusive to Aß itself but can coincide with inflammation. Our study corroborates these conclusions, as the imaging studies presented here are highly inflammatory diseases that do not produce Aß plaques.

Limitations for the study are present. The patient number is low on account of the rarity of moyamoya syndrome, which also precludes patients from being evaluated at similar stages and complicates coordination of imaging patients with such a rare condition. Additionally, the lack of a uniform resolution in the PET images can cause existing constraints on resolution to be exacerbated. Measures to reconstruct images from multiple scanners with high and low frequency corrections could limit variability partially but not entirely (Joshi *et al.*, 2009). PET inherently also has limitations from the partial volume effect, where limitations on resolution may augment with disease-related atrophy. In the use of [^{11}C]-PiB for Alzheimer's Disease, for example, partial volume effect influenced analysis of certain structures (Thomas *et al.*, 2011). Implementations for correcting these hindrances on resolution, though, were not possible, as some scanners in the study were decommissioned. In addition, the prior referenced partial correction methods assume homogeneity in white matter, which is not observed in our results. Finally, it is important to consider that the sulfation capacity will differ among patients and different diseases (Gamage *et al.*, 2006). This is particularly important among patients in this study who present with moyamoya syndrome with different clinical

histories. Hence, the sulfation dynamics of a patient with Cushing's syndrome (Figure 3.3) will have inherent differences from a patient with cranial radiation (Figure 3.4). These limitations fundamentally result from the rarity of moyamoya and the challenges posed in coordinating these studies.

Our study establishes a profound [^{11}C]-PiB signal in moyamoya syndrome that is associated with inflammatory changes from the disease that is irrelevant to Aß. Inflammatory changes in tissue reflected estrogen metabolic processes associated with astrogliosis, demyelination and hypoperfusion. This study also highlighted a dynamic [^{11}C]-PiB signal in multiple sclerosis in response to immunomodulatory therapy, thus showing that [^{11}C]-PiB signal varies with inflammation. Therefore, [^{11}C]-PiB is a proven substrate for SULT1E1, whose expression and activity can change with injury to the brain as seen with estrogen mediated responses to inflammatory processes related to microstructural changes in moyamoya syndrome.

Chapter Four: Conclusions

Moyamoya syndrome is a rare cerebrovascular disorder that threatens cerebral circulation. Inadequate flow stems from moyamoya collateral vessels that develop in response to arterial stenosis within the brain. Stenosis in the Circle of Willis causes cerebral positive pressure to drop. Limited flow provides a stimulus for angiogenesis, yet the vessels themselves sustain delayed flow and jeopardize hemodynamic stability.

Present techniques in imaging moyamoya will characterize perfusion abnormalities very thoroughly. PET, SPECT and MRI can perform hemodynamic assessment in moyamoya patients. Arterial spin-labeled MRI, dynamic susceptibility contrast (DSC) MRI, $H_2{}^{15}O$ and [$^{15}O_2$] PET, and [^{123}I]-IMP SPECT can verify reduced cerebral blood flow and cerebrovascular reserve after a vasodilatory stimulus. DSC MRI can also assess elevated cerebral blood volume (CBV) from vascular distention or decreased CBV within the infarcted area as well as delayed mean transit time and delivery for gadolinium. What these images cannot assess, however, is the impact of inflammation.

The reduced perfusion from these vessels facilitates a state of chronic hypoperfusion that engenders inflammatory reactions from astrocytes and microglial cells. Consequently, subcortical tissue that is perfused by moyamoya collaterals encounters microstructural changes in the form of demyelination and even axonal loss. Apparent Diffusion Coefficient MRI studies have verified that normal appearing white matter in moyamoya can have elevated signal in the hemisphere with reduced flow and cerebrovascular reserve. Diffusion Tensor Imaging and Diffusion Kurtosis Imaging (DKI) have verified that white matter and subcortical structures in moyamoya patients

demonstrate microstructural changes consistent with demyelination and axonal loss. Therefore, inflammatory signaling from these changes should be quite profound.

This is the first report documenting [^{11}C]-PiB in moyamoya patients. It is also the first report that imaged SULT1E1 in humans with [^{11}C]-PiB. In this study, [^{11}C]-PiB imaging provided evidence for elevated signal in response to increased inflammation by targeting estrogen sulfotransferase (SULT1E1). This study used a non-hemorrhagic model of stroke, moyamoya syndrome patients, and a patient with multiple sclerosis receiving immunomodulatory therapy to highlight the retention of [^{11}C]-PiB in inflammatory disease with beta amyloid. These cases were meant to introduce stimuli that lack amyloid for the purpose of gauging estrogen metabolism in response to inflammation.

The middle cerebral arterial occlusion model demonstrated colocalization of SULT1E1 expression with elevated [^{11}C]-PiB in the peri-infarct area, where reactive astrocytes form. Estrogen produced by reactive astrocytes in the peri-infarct region is found in the presence of abundant cytokines. Additionally, SULT1E1 expression colocalized with [^{11}C]-PiB is consistent with previously observed sulfation of [^{11}C]-PiB in tissue homogenates bearing signal. Hence, elevated [^{11}C]-PiB observed in this model supports elevated SULT1E1 expression in the presence of inflammation.

[^{11}C]-PiB SRTM DVR in moyamoya patients was substantially elevated in the corona radiata, thalamus, pons and internal capsule when compared to controls ($p<0.01$). These regions are in agreement with earlier DKI studies that identified microstructural changes in the corona radiata and thalamus. Demyelinating lesions are highly inflammatory and involve cytokine signaling for activation of astrocytes and microglia in

addition to T cell recruitment. Therefore, SULT1E1 activity in these regions can reflect regulatory efforts to maintain availability of estrogen,

[^{11}C]-PiB signal in subcortical and midbrain structures elucidated the inflammatory nature of moyamoya further in the two cases presented. A 33.4-year old female patient that experienced a bilateral EDAS and Cushing syndrome had pronounce [^{11}C]-PiB uptake in the pons. Recovery in white matter after revascularization procedures may experience hemodynamic instability that can cause harm.

A 27.0-year old female patient with radiation-induced atheritis had significant subcortical and midbrain [^{11}C]-PiB uptake. The magnitude was tantamount to cortical signal in AD patients. Her entire circulation was threatened with occlusion and produced an ischemic environment that was chronically inflamed.

The last case was a 50.3-year old relapse-remitting multiple sclerosis patient. After one month of therapy, his post-treatment scan produced a 30% drop in the corona radiata, 34.3% in the ventral pallidum, 14.7% in the thalamus, and 16.7% in the internal capsule. The significance of this result is not only to demonstrate high signal in the pre-treatment scan but also to show that [^{11}C]-PiB is a dynamic signal associated with inflammation. Moreover, this inflammatory signal is consistent with SULT1E1 but not beta amyloid.

In the United States, the incidence of moyamoya disease is 0.0001%, unlike in East Asian countries that could witness nearly ten times greater. The coordination of a study with moyamoya patients is, therefore, challenging. Patients will not have uniform stages of collateral development, nor will they similar have similar demographics such as age. Yet, moyamoya syndrome represents a chronically hypoperfused brain that endures

substantial inflammation. Inflammatory changes in tissue reflected estrogen metabolic processes associated with astrogliosis, demyelination and hypoperfusion. This study also highlighted dynamic response from [^{11}C]-PiB to steroidal therapy associated with changes in inflammation in multiple sclerosis. Observed [^{11}C]-PiB signal accumulation in amyloid is not consistent with reduction. Similarly, declining [^{11}C]-PiB accumulation in myelin binding protein also will not produce such a drop within one month. SULT1E1 expression and activity, however, can change with injury to the brain.

[^{11}C]-PiB accumulation in meningioma is similar to the signal seen in this report. [^{11}C]-PiB retention in these brain tumors that lack amyloid supports the conclusions about inflammatory signaling. Upregulated COX-2 and enhanced prostaglandin synthesis enable tumor proliferation, which explains how SULT1E1 could be active in these tumors. Estrogen-mediated responses to inflammatory processes related to microstructural changes in moyamoya syndrome and multiple sclerosis demonstrated elevated [^{11}C]-PiB signal. Therefore, [^{11}C]-PiB is a proven substrate for SULT1E1 that demonstrated uptake in highly inflamed regions that lack amyloid.

References

Abbott NJ, Ronnback L, Hansson E. Astrocyte-endothelial interactions at the blood-brain barrier. Nat Rev Neurosci 2006; 7(1): 41-53.

Ahima RS, Stanley TL, Khor VK, Zanni MV, Grinspoon SK. Estrogen sulfotransferase is expressed in subcutaneous adipose tissue of obese humans in association with TNF-alpha and SOCS3. The Journal of clinical endocrinology and metabolism 2011; 96(7): E1153-8.

Ahn IM, Park DH, Hann HJ, Kim KH, Kim HJ, Ahn HS. Incidence, prevalence, and survival of moyamoya disease in Korea: a nationwide, population-based study. Stroke; a journal of cerebral circulation 2014; 45(4): 1090-5.

Airla N, Luomala M, Elovaara I, Kettunen E, Knuutila S, Lehtimaki T. Suppression of immune system genes by methylprednisolone in exacerbations of multiple sclerosis. Preliminary results. J Neurol 2004; 251(10): 1215-9.

Annunziata P, Lore F, Venturini E, Morana P, Guarino E, Borghi S*, et al.* Early synthesis and correlation of serum anti-thyroid antibodies with clinical parameters in multiple sclerosis. Journal of the neurological sciences 1999; 168(1): 32-6.

Aoki S, Hayashi N, Abe O, Shirouzu I, Ishigame K, Okubo T*, et al.* Radiation-induced arteritis: thickened wall with prominent enhancement on cranial MR images report of five cases and comparison with 18 cases of Moyamoya disease. Radiology 2002; 223(3): 683-8.

Arai KI, Lee F, Miyajima A, Miyatake S, Arai N, Yokota T. Cytokines: coordinators of immune and inflammatory responses. Annu Rev Biochem 1990; 59: 783-836.

Arteaga DF, Strother MK, Faraco CC, Jordan LC, Ladner TR, Dethrage LM*, et al.* The vascular steal phenomenon is an incomplete contributor to negative cerebrovascular reactivity in patients with symptomatic intracranial stenosis. Journal of cerebral blood flow and metabolism : official journal of the International Society of Cerebral Blood Flow and Metabolism 2014; 34(9): 1453-62.

Arevalo MA, Azcoitia I, Garcia-Segura LM. The neuroprotective actions of oestradiol and oestrogen receptors. Nat Rev Neurosci 2015; 16(1): 17-29.

Avants BB, Epstein CL, Grossman M, Gee JC. Symmetric diffeomorphic image registration with cross-correlation: evaluating automated labeling of elderly and neurodegenerative brain. Med Image Anal 2008; 12(1): 26-41.

Bengel FM, Minoshima S. 2012 SNM Highlights Lectures. Journal of nuclear medicine : official publication, Society of Nuclear Medicine 2012; 53(9): 15N-31N.

Biancalana M, Koide S. Molecular mechanism of Thioflavin-T binding to amyloid fibrils. Biochim Biophys Acta 2010; 1804(7): 1405-12.

Bitsch A, Schuchardt J, Bunkowski S, Kuhlmann T, Bruck W. Acute axonal injury in multiple sclerosis. Correlation with demyelination and inflammation. Brain 2000; 123 (Pt 6): 1174-83.

Blanchard RL, Freimuth RR, Buck J, Weinshilboum RM, Coughtrie MW. A proposed nomenclature system for the cytosolic sulfotransferase (SULT) superfamily. Pharmacogenetics 2004; 14(3): 199-211.

Blennow K, Zetterberg H. Pinpointing plaques with PIB. Nat Med 2006; 12(7): 753-4; discussion 4.

Braak H, Braak E. Neuropathological stageing of Alzheimer-related changes. Acta Neuropathol 1991; 82(4): 239-59.

Brown WR, Moody DM, Thore CR, Challa VR, Anstrom JA. Vascular dementia in leukoaraiosis may be a consequence of capillary loss not only in the lesions, but in normal-appearing white matter and cortex as well. Journal of the neurological sciences 2007; 257(1-2): 62-6.

Burchell B, Coughtrie MW. Genetic and environmental factors associated with variation of human xenobiotic glucuronidation and sulfation. Environ Health Perspect 1997; 105 Suppl 4: 739-47.

Burke GM, Burke AM, Sherma AK, Hurley MC, Batjer HH, Bendok BR. Moyamoya disease: a summary. Neurosurg Focus 2009; 26(4): E11.

Cairns NJ, Ikonomovic MD, Benzinger T, Storandt M, Fagan AM, Shah AR*, et al.* Absence of Pittsburgh compound B detection of cerebral amyloid beta in a patient with clinical, cognitive, and cerebrospinal fluid markers of Alzheimer disease: a case report. Arch Neurol 2009; 66(12): 1557-62.

Calviere L, Catalaa I, Marlats F, Viguier A, Bonneville F, Cognard C*, et al.* Correlation between cognitive impairment and cerebral hemodynamic disturbances on perfusion magnetic resonance imaging in European adults with moyamoya disease. Clinical article. J Neurosurg 2010; 113(4): 753-9.

Calviere L, Ssi Yan Kai G, Catalaa I, Marlats F, Bonneville F, Larrue V. Executive dysfunction in adults with moyamoya disease is associated with increased diffusion in frontal white matter. J Neurol Neurosurg Psychiatry 2012; 83(6): 591-3.

Campen CJ, Kranick SM, Kasner SE, Kessler SK, Zimmerman RA, Lustig R*, et al.* Cranial irradiation increases risk of stroke in pediatric brain tumor survivors. Stroke; a journal of cerebral circulation 2012; 43(11): 3035-40.

Cannella B, Raine CS. The adhesion molecule and cytokine profile of multiple sclerosis lesions. Annals of neurology 1995; 37(4): 424-35.

Carswell HV, Dominiczak AF, Garcia-Segura LM, Harada N, Hutchison JB, Macrae IM. Brain aromatase expression after experimental stroke: topography and time course. J Steroid Biochem Mol Biol 2005; 96(1): 89-91.

Cechetti F, Pagnussat AS, Worm PV, Elsner VR, Ben J, da Costa MS*, et al.* Chronic brain hypoperfusion causes early glial activation and neuronal death, and subsequent long-term memory impairment. Brain Res Bull 2012; 87(1): 109-16.

Chaves H, Bergamo Y, Paz S, Sanchez F, Vazquez S. Sphenoid wing meningioma behavior on 11C-PiB and 18F-FDG PET. Clin Nucl Med 2015; 40(1): e81-2.

Cole GB. In Vivo Molecular Imaging Probes for Estrogen Sulfotransferase Enzyme (SULT1E1) [Doctoral Dissertation]. Los Angeles, CA: University of California, Los Angeles; 2011.

Cole GB, Keum G, Liu J, Small GW, Satyamurthy N, Kepe V*, et al.* Specific estrogen sulfotransferase (SULT1E1) substrates and molecular imaging probe candidates. Proceedings of the National Academy of Sciences of the United States of America 2010; 107(14): 6222-7.

Conklin J, Fierstra J, Crawley AP, Han JS, Poublanc J, Mandell DM*, et al.* Impaired cerebrovascular reactivity with steal phenomenon is associated with increased diffusion in white matter of patients with Moyamoya disease. Stroke; a journal of cerebral circulation 2010; 41(8): 1610-6.

Cunard R, Eto Y, Muljadi JT, Glass CK, Kelly CJ, Ricote M. Repression of IFN-gamma expression by peroxisome proliferator-activated receptor gamma. J Immunol 2004; 172(12): 7530-6.

Czabanka M, Pena-Tapia P, Schubert GA, Woitzik J, Vajkoczy P, Schmiedek P. Characterization of cortical microvascularization in adult moyamoya disease. Stroke; a journal of cerebral circulation 2008; 39(6): 1703-9.

Desai SS, Paulino AC, Mai WY, Teh BS. Radiation-induced moyamoya syndrome. Int J Radiat Oncol Biol Phys 2006; 65(4): 1222-7.

Didier N, Romero IA, Creminon C, Wijkhuisen A, Grassi J, Mabondzo A. Secretion of interleukin-1beta by astrocytes mediates endothelin-1 and tumour necrosis factor-alpha effects on human brain microvascular endothelial cell permeability. Journal of neurochemistry 2003; 86(1): 246-54.

Donahue MJ, Ayad M, Moore R, van Osch M, Singer R, Clemmons P*, et al.* Relationships between hypercarbic reactivity, cerebral blood flow, and arterial circulation times in patients with moyamoya disease. J Magn Reson Imaging 2013; 38(5): 1129-39.

Dorfman LJ, Fischbein NJ, Woodard JI, Choudhri O, Bell-Stephens TE, Steinberg GK. Moyamoya disease can masquerade as multiple sclerosis. Neurologist 2012; 18(6): 398-403.

Falany CN. Enzymology of human cytosolic sulfotransferases. FASEB J 1997; 11(4): 206-16.

Falany CN, Krasnykh V, Falany JL. Bacterial expression and characterization of a cDNA for human liver estrogen sulfotransferase. J Steroid Biochem Mol Biol 1995; 52(6): 529-39.

Falany JL, Pilloff DE, Leyh TS, Falany CN. Sulfation of raloxifene and 4-hydroxytamoxifen by human cytosolic sulfotransferases. Drug Metab Dispos 2006; 34(3): 361-8.

Ferguson B, Matyszak MK, Esiri MM, Perry VH. Axonal damage in acute multiple sclerosis lesions. Brain 1997; 120 (Pt 3): 393-9.

Fodero-Tavoletti MT, Rowe CC, McLean CA, Leone L, Li QX, Masters CL*, et al.* Characterization of PiB binding to white matter in Alzheimer disease and other dementias. Journal of nuclear medicine : official publication, Society of Nuclear Medicine 2009; 50(2): 198-204.

Fox HS, Bond BL, Parslow TG. Estrogen regulates the IFN-gamma promoter. J Immunol 1991; 146(12): 4362-7.

Fukui M. Guidelines for the diagnosis and treatment of spontaneous occlusion of the circle of Willis ('moyamoya' disease). Research Committee on Spontaneous Occlusion of the Circle of Willis (Moyamoya Disease) of the Ministry of Health and Welfare, Japan. Clin Neurol Neurosurg 1997; 99 Suppl 2: S238-40.

Fukui M, Kono S, Sueishi K, Ikezaki K. Moyamoya disease. Neuropathology 2000; 20 Suppl: S61-4.

Fujimura M, Niizuma K, Inoue T, Sato K, Endo H, Shimizu H*, et al.* Minocycline prevents focal neurological deterioration due to cerebral hyperperfusion after

extracranial-intracranial bypass for moyamoya disease. Neurosurgery 2014a; 74(2): 163-70; discussion 70.

Fujimura M, Sonobe S, Nishijima Y, Niizuma K, Sakata H, Kure S*, et al.* Genetics and Biomarkers of Moyamoya Disease: Significance of RNF213 as a Susceptibility Gene. J Stroke 2014b; 16(2): 65-72.

Fujimura M, Watanabe M, Narisawa A, Shimizu H, Tominaga T. Increased expression of serum Matrix Metalloproteinase-9 in patients with moyamoya disease. Surg Neurol 2009; 72(5): 476-80; discussion 80.

Furimsky AM, Green CE, Sharp LE, Catz P, Adjei AA, Parman T*, et al.* Effect of resveratrol on 17beta-estradiol sulfation by human hepatic and jejunal S9 and recombinant sulfotransferase 1E1. Drug Metab Dispos 2008; 36(1): 129-36.

Furst H, Hartl WH, Janssen I. Patterns of cerebrovascular reactivity in patients with unilateral asymptomatic carotid artery stenosis. Stroke; a journal of cerebral circulation 1994; 25(6): 1193-200.

Gamage N, Barnett A, Hempel N, Duggleby RG, Windmill KF, Martin JL*, et al.* Human sulfotransferases and their role in chemical metabolism. Toxicol Sci 2006; 90(1): 5-22.

Garcia-Segura LM, Chowen JA, Duenas M, Torres-Aleman I, Naftolin F. Gonadal steroids as promoters of neuro-glial plasticity. Psychoneuroendocrinology 1994; 19(5-7): 445-53.

Gatson JW, Simpkins JW, Yi KD, Idris AH, Minei JP, Wigginton JG. Aromatase is increased in astrocytes in the presence of elevated pressure. Endocrinology 2011; 152(1): 207-13.

Grossman EJ, Jensen JH, Babb JS, Chen Q, Tabesh A, Fieremans E*, et al.* Cognitive impairment in mild traumatic brain injury: a longitudinal diffusional kurtosis and perfusion imaging study. AJNR Am J Neuroradiol 2013; 34(5): 951-7, S1-3.

Gunn RN, Lammertsma AA, Hume SP, Cunningham VJ. Parametric imaging of ligand-receptor binding in PET using a simplified reference region model. NeuroImage 1997; 6(4): 279-87.

Heistad DD, Mayhan WG, Coyle P, Baumbach GL. Impaired dilatation of cerebral arterioles in chronic hypertension. Blood Vessels 1990; 27(2-5): 258-62.

Helenius J, Soinne L, Salonen O, Kaste M, Tatlisumak T. Leukoaraiosis, ischemic stroke, and normal white matter on diffusion-weighted MRI. Stroke; a journal of cerebral circulation 2002; 33(1): 45-50.

Hobkirk R. Steroid sulfotransferases and steroid sulfate sulfatases: characteristics and biological roles. Can J Biochem Cell Biol 1985; 63(11): 1127-44.

Holcomb L, Gordon MN, McGowan E, Yu X, Benkovic S, Jantzen P*, et al.* Accelerated Alzheimer-type phenotype in transgenic mice carrying both mutant amyloid precursor protein and presenilin 1 transgenes. Nat Med 1998; 4(1): 97-100.

Hong YT, Veenith T, Dewar D, Outtrim JG, Mani V, Williams C*, et al.* Amyloid imaging with carbon 11-labeled Pittsburgh compound B for traumatic brain injury. JAMA Neurol 2014; 71(1): 23-31.

Honma S, Shimodaira K, Shimizu Y, Tsuchiya N, Saito H, Yanaihara T*, et al.* The influence of inflammatory cytokines on estrogen production and cell proliferation in human breast cancer cells. Endocr J 2002; 49(3): 371-7.

Iadecola C. The pathobiology of vascular dementia. Neuron 2013; 80(4): 844-66.

Ihunnah CA, Wada T, Philips BJ, Ravuri SK, Gibbs RB, Kirisci L*, et al.* Estrogen sulfotransferase/SULT1E1 promotes human adipogenesis. Mol Cell Biol 2014; 34(9): 1682-94.

Im SH, Cho CB, Joo WI, Chough CK, Park HK, Lee KJ*, et al.* Prevalence and epidemiological features of moyamoya disease in Korea. J Cerebrovasc Endovasc Neurosurg 2012; 14(2): 75-8.

Ishii R, Takeuchi S, Ibayashi K, Tanaka R. Intelligence in children with moyamoya disease: evaluation after surgical treatments with special reference to changes in cerebral blood flow. Stroke; a journal of cerebral circulation 1984; 15(5): 873-7.

Ito A, Fujimura M, Niizuma K, Kanoke A, Sakata H, Morita-Fujimura Y*, et al.* Enhanced post-ischemic angiogenesis in mice lacking RNF213; a susceptibility gene for moyamoya disease. Brain Res 2015; 1594: 310-20.

Iwamoto N, Nishiyama E, Ohwada J, Arai H. Distribution of amyloid deposits in the cerebral white matter of the Alzheimer's disease brain: relationship to blood vessels. Acta Neuropathol 1997; 93(4): 334-40.

Jack CR, Jr., Lowe VJ, Senjem ML, Weigand SD, Kemp BJ, Shiung MM*, et al.* 11C PiB and structural MRI provide complementary information in imaging of Alzheimer's disease and amnestic mild cognitive impairment. Brain 2008; 131(Pt 3): 665-80.

Jaffe AB, Toran-Allerand CD, Greengard P, Gandy SE. Estrogen regulates metabolism of Alzheimer amyloid beta precursor protein. J Biol Chem 1994; 269(18): 13065-8.

Jefferson AL, Glosser G, Detre JA, Sinson G, Liebeskind DS. Neuropsychological and perfusion MR imaging correlates of revascularization in a case of moyamoya syndrome. AJNR Am J Neuroradiol 2006; 27(1): 98-100.

Jensen JH, Helpern JA, Ramani A, Lu H, Kaczynski K. Diffusional kurtosis imaging: the quantification of non-gaussian water diffusion by means of magnetic resonance imaging. Magn Reson Med 2005; 53(6): 1432-40.

Jeong H, Kim J, Choi HS, Kim ES, Kim DS, Shim KW*, et al.* Changes in integrity of normal-appearing white matter in patients with moyamoya disease: a diffusion tensor imaging study. AJNR Am J Neuroradiol 2011; 32(10): 1893-8.

Johnson G, Nathan M, Parisi J, Lingle W, Hunt C, Peller P*, et al.* PiB PET/CT identification of meningiomas is not due to presence of amyloid-beta within tumors. J NUCL MED MEETING ABSTRACTS 2012; 53(1_MeetingAbstracts): 253-.

Joshi A, Koeppe RA, Fessler JA. Reducing between scanner differences in multi-center PET studies. NeuroImage 2009; 46(1): 154-9.

Kakuta Y, Pedersen LG, Carter CW, Negishi M, Pedersen LC. Crystal structure of estrogen sulphotransferase. Nat Struct Biol 1997; 4(11): 904-8.

Kakuta Y, Petrotchenko EV, Pedersen LC, Negishi M. The sulfuryl transfer mechanism. Crystal structure of a vanadate complex of estrogen sulfotransferase and mutational analysis. J Biol Chem 1998; 273(42): 27325-30.

Kamada F, Aoki Y, Narisawa A, Abe Y, Komatsuzaki S, Kikuchi A*, et al.* A genome-wide association study identifies RNF213 as the first Moyamoya disease gene. J Hum Genet 2011; 56(1): 34-40.

Kang HS, Kim JH, Phi JH, Kim YY, Kim JE, Wang KC*, et al.* Plasma matrix metalloproteinases, cytokines and angiogenic factors in moyamoya disease. J Neurol Neurosurg Psychiatry 2010; 81(6): 673-8.

Kanoke A, Fujimura M, Niizuma K, Fujimura T, Kakizaki A, Ito A*, et al.* Temporal profile of magnetic resonance angiography and decreased ratio of regulatory T cells after immunological adjuvant administration to mice lacking RNF213, a susceptibility gene for moyamoya disease. Brain Res 2016; 1642: 1-9.

Karanikas G, Schuetz M, Wahl K, Paul M, Kontur S, Pietschmann P*, et al.* Relation of anti-TPO autoantibody titre and T-lymphocyte cytokine production patterns in Hashimoto's thyroiditis. Clin Endocrinol (Oxf) 2005; 63(2): 191-6.

Karzmark P, Zeifert PD, Bell-Stephens TE, Steinberg GK, Dorfman LJ. Neurocognitive impairment in adults with moyamoya disease without stroke. Neurosurgery 2012; 70(3): 634-8.

Karzmark P, Zeifert PD, Tan S, Dorfman LJ, Bell-Stephens TE, Steinberg GK. Effect of moyamoya disease on neuropsychological functioning in adults. Neurosurgery 2008; 62(5): 1048-51; discussion 51-2.

Kazumata K, Tha KK, Narita H, Ito YM, Shichinohe H, Ito M*, et al.* Characteristics of Diffusional Kurtosis in Chronic Ischemia of Adult Moyamoya Disease: Comparing Diffusional Kurtosis and Diffusion Tensor Imaging. AJNR Am J Neuroradiol 2016a; 37(8): 1432-9.

Kazumata K, Tha KK, Narita H, Kusumi I, Shichinohe H, Ito M*, et al.* Chronic ischemia alters brain microstructural integrity and cognitive performance in adult moyamoya disease. Stroke; a journal of cerebral circulation 2015; 46(2): 354-60.

Kazumata K, Tha KK, Narita H, Shichinohe H, Ito M, Uchino H*, et al.* Investigating Brain Network Characteristics Interrupted by Covert White Matter Injury in Patients with Moyamoya Disease: Insights from Graph Theoretical Analysis. World Neurosurg 2016b; 89: 654-65 e2.

Kazumata K, Tha KK, Uchino H, Shiga T, Shichinohe H, Ito M*, et al.* Topographic changes in cerebral blood flow and reduced white matter integrity in the first 2 weeks following revascularization surgery in adult moyamoya disease. J Neurosurg 2016: 1-10.

Kepe V, Moghbel MC, Langstrom B, Zaidi H, Vinters HV, Huang SC*, et al.* Amyloid-beta positron emission tomography imaging probes: a critical review. J Alzheimers Dis 2013; 36(4): 613-31.

Kester MH, van Dijk CH, Tibboel D, Hood AM, Rose NJ, Meinl W*, et al.* Sulfation of thyroid hormone by estrogen sulfotransferase. The Journal of clinical endocrinology and metabolism 1999; 84(7): 2577-80.

Kim EH, Yum MS, Ra YS, Park JB, Ahn JS, Kim GH*, et al.* Importance of RNF213 polymorphism on clinical features and long-term outcome in moyamoya disease. J Neurosurg 2016; 124(5): 1221-7.

Kim HY, Kim J, Lee JH. Incidental finding of meningioma on C11-PIB PET. Clin Nucl Med 2012; 37(2): e36-7.

Kim SJ, Heo KG, Shin HY, Bang OY, Kim GM, Chung CS*, et al.* Association of thyroid autoantibodies with moyamoya-type cerebrovascular disease: a prospective study. Stroke; a journal of cerebral circulation 2010; 41(1): 173-6.

Kirkham FJ, Calamante F, Bynevelt M, Gadian DG, Evans JP, Cox TC*, et al.* Perfusion magnetic resonance abnormalities in patients with sickle cell disease. Annals of neurology 2001; 49(4): 477-85.

Klunk WE, Engler H, Nordberg A, Wang Y, Blomqvist G, Holt DP*, et al.* Imaging brain amyloid in Alzheimer's disease with Pittsburgh Compound-B. Annals of neurology 2004; 55(3): 306-19.

Klunk WE, Lopresti BJ, Ikonomovic MD, Lefterov IM, Koldamova RP, Abrahamson EE*, et al.* Binding of the positron emission tomography tracer Pittsburgh compound-B reflects the amount of amyloid-beta in Alzheimer's disease brain but not in transgenic mouse brain. The Journal of neuroscience : the official journal of the Society for Neuroscience 2005; 25(46): 10598-606.

Klunk WE, Wang Y, Huang GF, Debnath ML, Holt DP, Mathis CA. Uncharged thioflavin-T derivatives bind to amyloid-beta protein with high affinity and readily enter the brain. Life Sci 2001; 69(13): 1471-84.

Kobayashi H, Matsuda Y, Hitomi T, Okuda H, Shioi H, Matsuda T*, et al.* Biochemical and Functional Characterization of RNF213 (Mysterin) R4810K, a Susceptibility Mutation of Moyamoya Disease, in Angiogenesis In Vitro and In Vivo. J Am Heart Assoc 2015; 4(7).

Koehler RC, Gebremedhin D, Harder DR. Role of astrocytes in cerebrovascular regulation. J Appl Physiol (1985) 2006; 100(1): 307-17.

Kuhlmann T, Lingfeld G, Bitsch A, Schuchardt J, Bruck W. Acute axonal damage in multiple sclerosis is most extensive in early disease stages and decreases over time. Brain 2002; 125(Pt 10): 2202-12.

Kuroda S, Houkin K. Moyamoya disease: current concepts and future perspectives. Lancet Neurol 2008; 7(11): 1056-66.

Lammertsma AA, Hume SP. Simplified reference tissue model for PET receptor studies. NeuroImage 1996; 4(3 Pt 1): 153-8.

Lee M, Zaharchuk G, Guzman R, Achrol A, Bell-Stephens T, Steinberg GK. Quantitative hemodynamic studies in moyamoya disease: a review. Neurosurg Focus 2009; 26(4): E5.

Lee SC, Raine CS. Multiple sclerosis: oligodendrocytes in active lesions do not express class II major histocompatibility complex molecules. J Neuroimmunol 1989; 25(2-3): 261-6.

Leinonen V, Alafuzoff I, Aalto S, Suotunen T, Savolainen S, Nagren K*, et al.* Assessment of beta-amyloid in a frontal cortical brain biopsy specimen and by positron emission tomography with carbon 11-labeled Pittsburgh Compound B. Arch Neurol 2008; 65(10): 1304-9.

Lee DJ, Liebeskind DS. Characterization of inpatient moyamoya in the United States: 1988-2004. Frontiers in neurology 2011; 2: 43.

Li H, Zhang ZS, Dong ZN, Ma MJ, Yang WZ, Han C*, et al.* Increased thyroid function and elevated thyroid autoantibodies in pediatric patients with moyamoya disease: a case-control study. Stroke; a journal of cerebral circulation 2011; 42(4): 1138-9.

Liebeskind DS. Collateral circulation. Stroke; a journal of cerebral circulation 2003; 34(9): 2279-84.

Lin CS, Polsky K, Nadler JV, Crain BJ. Selective neocortical and thalamic cell death in the gerbil after transient ischemia. Neuroscience 1990; 35(2): 289-99.

Lin W, Kemper A, Dupree JL, Harding HP, Ron D, Popko B. Interferon-gamma inhibits central nervous system remyelination through a process modulated by endoplasmic reticulum stress. Brain 2006; 129(Pt 5): 1306-18.

Liu W, Morito D, Takashima S, Mineharu Y, Kobayashi H, Hitomi T*, et al.* Identification of RNF213 as a susceptibility gene for moyamoya disease and its possible role in vascular development. PLoS One 2011; 6(7): e22542.

Liu P, Uh J, Devous MD, Adinoff B, Lu H. Comparison of relative cerebral blood flow maps using pseudo-continuous arterial spin labeling and single photon emission computed tomography. NMR Biomed 2012; 25(5): 779-86.

Liu T, McDonnell PC, Young PR, White RF, Siren AL, Hallenbeck JM*, et al.* Interleukin-1 beta mRNA expression in ischemic rat cortex. Stroke; a journal of cerebral circulation 1993; 24(11): 1746-50; discussion 50-1.

Logan J, Kim SW, Pareto D, Telang F, Wang GJ, Fowler JS*, et al.* Kinetic analysis of [11C]vorozole binding in the human brain with positron emission tomography. Mol Imaging 2014; 13: 1-12.

Lopresti BJ, Klunk WE, Mathis CA, Hoge JA, Ziolko SK, Lu X*, et al.* Simplified quantification of Pittsburgh Compound B amyloid imaging PET studies: a comparative analysis. Journal of nuclear medicine: official publication, Society of Nuclear Medicine 2005; 46(12): 1959-72.

Lubman DI, Pantelis C, Desmond P, Proffitt TM, Velakoulis D. Moyamoya disease in a patient with schizophrenia. J Int Neuropsychol Soc 2003; 9(5): 806-10.

Ly JV, Rowe CC, Villemagne VL, Zavala JA, Ma H, Sahathevan R*, et al.* Subacute ischemic stroke is associated with focal 11C PiB positron emission tomography retention but not with global neocortical Abeta deposition. Stroke; a journal of cerebral circulation 2012; 43(5): 1341-6.

Maeda J, Ji B, Irie T, Tomiyama T, Maruyama M, Okauchi T*, et al.* Longitudinal, quantitative assessment of amyloid, neuroinflammation, and anti-amyloid treatment in a living mouse model of Alzheimer's disease enabled by positron emission tomography. The Journal of neuroscience : the official journal of the Society for Neuroscience 2007; 27(41): 10957-68.

Mandell DM, Han JS, Poublanc J, Crawley AP, Kassner A, Fisher JA*, et al.* Selective reduction of blood flow to white matter during hypercapnia corresponds with leukoaraiosis. Stroke; a journal of cerebral circulation 2008; 39(7): 1993-8.

Marx N, Mach F, Sauty A, Leung JH, Sarafi MN, Ransohoff RM*, et al.* Peroxisome proliferator-activated receptor-gamma activators inhibit IFN-gamma-induced expression of the T cell-active CXC chemokines IP-10, Mig, and I-TAC in human endothelial cells. J Immunol 2000; 164(12): 6503-8.

Masuda J, Ogata J, Yutani C. Smooth muscle cell proliferation and localization of macrophages and T cells in the occlusive intracranial major arteries in moyamoya disease. Stroke; a journal of cerebral circulation 1993; 24(12): 1960-7.

Mathis CA, Wang Y, Holt DP, Huang GF, Debnath ML, Klunk WE. Synthesis and evaluation of 11C-labeled 6-substituted 2-arylbenzothiazoles as amyloid imaging agents. J Med Chem 2003; 46(13): 2740-54.

Mathis CAH, D. P.; Wang, Y.; Huang, G. F.; Debnath, M. L.; Shao, L.; Klunk, W. E. "Species-dependent metabolism of the amyloid imaging agent [C-11] PIB." Journal of nuclear medicine : official publication, Society of Nuclear Medicine 2004; 45(5 (Suppl)).

Meyer PT, Hellwig S, Amtage F, Rottenburger C, Sahm U, Reuland P*, et al.* Dual-biomarker imaging of regional cerebral amyloid load and neuronal activity in dementia with PET and 11C-labeled Pittsburgh compound B. Journal of nuclear medicine : official publication, Society of Nuclear Medicine 2011; 52(3): 393-400.

Mintun MA, Larossa GN, Sheline YI, Dence CS, Lee SY, Mach RH*, et al.* [11C]PIB in a nondemented population: potential antecedent marker of Alzheimer disease. Neurology 2006; 67(3): 446-52.

Moghbel MC, Saboury B, Basu S, Metzler SD, Torigian DA, Langstrom B*, et al.* Amyloid-beta imaging with PET in Alzheimer's disease: is it feasible with current radiotracers and technologies? Eur J Nucl Med Mol Imaging 2012; 39(2): 202-8.

Meinl E, Aloisi F, Ertl B, Weber F, de Waal Malefyt R, Wekerle H*, et al.* Multiple sclerosis. Immunomodulatory effects of human astrocytes on T cells. Brain 1994; 117 (Pt 6): 1323-32.

Merlo S, Sortino MA. Estrogen activates matrix metalloproteinases-2 and -9 to increase beta amyloid degradation. Mol Cell Neurosci 2012; 49(4): 423-9.

Minagar A, Barnett MH, Benedict RH, Pelletier D, Pirko I, Sahraian MA*, et al.* The thalamus and multiple sclerosis: modern views on pathologic, imaging, and clinical aspects. Neurology 2013; 80(2): 210-9.

Minagar A, Shapshak P, Fujimura R, Ownby R, Heyes M, Eisdorfer C. The role of macrophage/microglia and astrocytes in the pathogenesis of three neurologic disorders: HIV-associated dementia, Alzheimer disease, and multiple sclerosis. Journal of the neurological sciences 2002; 202(1-2): 13-23.

Meyer PT, Hellwig S, Amtage F, Rottenburger C, Sahm U, Reuland P*, et al.* Dual-biomarker imaging of regional cerebral amyloid load and neuronal activity in dementia with PET and 11C-labeled Pittsburgh compound B. Journal of nuclear medicine : official publication, Society of Nuclear Medicine 2011; 52(3): 393-400.

Miki Y, Nakata T, Suzuki T, Darnel AD, Moriya T, Kaneko C*, et al.* Systemic distribution of steroid sulfatase and estrogen sulfotransferase in human adult and fetal tissues. The Journal of clinical endocrinology and metabolism 2002; 87(12): 5760-8.

Miller AP, Feng W, Xing D, Weathington NM, Blalock JE, Chen YF*, et al.* Estrogen modulates inflammatory mediator expression and neutrophil chemotaxis in injured arteries. Circulation 2004; 110(12): 1664-9.

Minopoli G, Stante M, Napolitano F, Telese F, Aloia L, De Felice M*, et al.* Essential roles for Fe65, Alzheimer amyloid precursor-binding protein, in the cellular response to DNA damage. J Biol Chem 2007; 282(2): 831-5.

Mitchell WG, Fishman LS, Miller JH, Nelson M, Zeltzer PM, Soni D*, et al.* Stroke as a late sequela of cranial irradiation for childhood brain tumors. J Child Neurol 1991; 6(2): 128-33.

Moody DM, Bell MA, Challa VR. Features of the cerebral vascular pattern that predict vulnerability to perfusion or oxygenation deficiency: an anatomic study. AJNR Am J Neuroradiol 1990; 11(3): 431-9.

Mori S, Oishi K, Jiang H, Jiang L, Li X, Akhter K*, et al.* Stereotaxic white matter atlas based on diffusion tensor imaging in an ICBM template. NeuroImage 2008; 40(2): 570-82.

Morimoto T, Mineharu Y, Kobayashi H, Harada KH, Funaki T, Takagi Y*, et al.* Significant Association of the RNF213 p.R4810K Polymorphism with Quasi-Moyamoya Disease. J Stroke Cerebrovasc Dis 2016.

Mugikura S, Takahashi S, Higano S, Shirane R, Sakurai Y, Yamada S. Predominant involvement of ipsilateral anterior and posterior circulations in moyamoya disease. Stroke; a journal of cerebral circulation 2002; 33(6): 1497-500.

Muir EM, Adcock KH, Morgenstern DA, Clayton R, von Stillfried N, Rhodes K*, et al.* Matrix metalloproteases and their inhibitors are produced by overlapping populations of activated astrocytes. Brain Res Mol Brain Res 2002; 100(1-2): 103-17.

Nadkarni S, Cooper D, Brancaleone V, Bena S, Perretti M. Activation of the annexin A1 pathway underlies the protective effects exerted by estrogen in polymorphonuclear leukocytes. Arterioscler Thromb Vasc Biol 2011; 31(11): 2749-59.

Nakamizo A, Kikkawa Y, Hiwatashi A, Matsushima T, Sasaki T. Executive function and diffusion in frontal white matter of adults with moyamoya disease. J Stroke Cerebrovasc Dis 2014; 23(3): 457-61.

Nakamura Y, Miki Y, Suzuki T, Nakata T, Darnel AD, Moriya T*, et al.* Steroid sulfatase and estrogen sulfotransferase in the atherosclerotic human aorta. Am J Pathol 2003; 163(4): 1329-39.

Nakamura Y, Suzuki T, Sasano H. Estrogen actions and in situ synthesis in human vascular smooth muscle cells and their correlation with atherosclerosis. J Steroid Biochem Mol Biol 2005; 93(2-5): 263-8.

Nakanishi M, Kaito M, Gondo Y, Takada H, Matsui M, Hirose G. Moyamoya disease presenting with an acute confusional state in an elderly patient. J Stroke Cerebrovasc Dis 2010; 19(3): 247-50.

Nakaya M, Tachibana H, Yamada K. Effect of estrogens on the interferon-gamma producing cell population of mouse splenocytes. Biosci Biotechnol Biochem 2006; 70(1): 47-53.

Nash AR, Glenn WK, Moore SS, Kerr J, Thompson AR, Thompson EO. Oestrogen sulfotransferase: molecular cloning and sequencing of cDNA for the bovine placental enzyme. Aust J Biol Sci 1988; 41(4): 507-16.

Negishi M, Pedersen LG, Petrotchenko E, Shevtsov S, Gorokhov A, Kakuta Y*, et al.* Structure and function of sulfotransferases. Arch Biochem Biophys 2001; 390(2): 149-57.

Neumaier B, Deisenhofer S, Furst D, von Arnim CA, Thees S, Buck AK*, et al.* Radiosynthesis and evaluation of [11C]BTA-1 and [11C]3'-Me-BTA-1 as potential radiotracers for in vivo imaging of beta-amyloid plaques. Nuklearmedizin 2007; 46(6): 271-80.

Nihashi T, Inao S, Kajita Y, Kawai T, Sugimoto T, Niwa M*, et al.* Expression and distribution of beta amyloid precursor protein and beta amyloid peptide in reactive astrocytes after transient middle cerebral artery occlusion. Acta Neurochir (Wien) 2001; 143(3): 287-95.

Ogasawara K, Ito H, Sasoh M, Okuguchi T, Kobayashi M, Yukawa H*, et al.* Quantitative measurement of regional cerebrovascular reactivity to acetazolamide using 123I-N-isopropyl-p-iodoamphetamine autoradiography with SPECT: validation study using H2 15O with PET. Journal of nuclear medicine : official publication, Society of Nuclear Medicine 2003; 44(4): 520-5.

Ohkubo K, Sakai Y, Inoue H, Akamine S, Ishizaki Y, Matsushita Y*, et al.* Moyamoya disease susceptibility gene RNF213 links inflammatory and angiogenic signals in endothelial cells. Scientific reports 2015; 5: 13191.

Oishi K, Faria A, Jiang H, Li X, Akhter K, Zhang J*, et al.* Atlas-based whole brain white matter analysis using large deformation diffeomorphic metric mapping: application to normal elderly and Alzheimer's disease participants. NeuroImage 2009; 46(2): 486-99.

Panitch HS, Hirsch RL, Schindler J, Johnson KP. Treatment of multiple sclerosis with gamma interferon: exacerbations associated with activation of the immune system. Neurology 1987; 37(7): 1097-102.

Pantoni L, Garcia JH. Pathogenesis of leukoaraiosis: a review. Stroke; a journal of cerebral circulation 1997; 28(3): 652-9.

Pantoni L, Garcia JH, Gutierrez JA. Cerebral white matter is highly vulnerable to ischemia. Stroke; a journal of cerebral circulation 1996; 27(9): 1641-6; discussion 7.

Pedersen LC, Petrotchenko E, Shevtsov S, Negishi M. Crystal structure of the human estrogen sulfotransferase-PAPS complex: evidence for catalytic role of Ser137 in the sulfuryl transfer reaction. J Biol Chem 2002; 277(20): 17928-32.

Phelps ME, Barrio JR. Correlation of brain amyloid with "aerobic glycolysis": A question of assumptions? Proceedings of the National Academy of Sciences of the United States of America 2010; 107(41): 17459-60.

Pober JS, Collins T, Gimbrone MA, Jr., Cotran RS, Gitlin JD, Fiers W*, et al.* Lymphocytes recognize human vascular endothelial and dermal fibroblast Ia antigens induced by recombinant immune interferon. Nature 1983; 305(5936): 726-9.

Powers WJ. Cerebral hemodynamics in ischemic cerebrovascular disease. Annals of neurology 1991; 29(3): 231-40.

Rafat N, Beck G, Pena-Tapia PG, Schmiedek P, Vajkoczy P. Increased levels of circulating endothelial progenitor cells in patients with Moyamoya disease. Stroke; a journal of cerebral circulation 2009; 40(2): 432-8.

Ragel BT, Jensen RL, Couldwell WT. Inflammatory response and meningioma tumorigenesis and the effect of cyclooxygenase-2 inhibitors. Neurosurg Focus 2007; 23(4): E7.

Ragel BT, Jensen RL, Gillespie DL, Prescott SM, Couldwell WT. Ubiquitous expression of cyclooxygenase-2 in meningiomas and decrease in cell growth following in vitro treatment with the inhibitor celecoxib: potential therapeutic application. J Neurosurg 2005; 103(3): 508-17.

Research Committee on the P, Treatment of Spontaneous Occlusion of the Circle of W, Health Labour Sciences Research Grant for Research on Measures for Infractable D. Guidelines for diagnosis and treatment of moyamoya disease (spontaneous occlusion of the circle of Willis). Neurol Med Chir (Tokyo) 2012; 52(5): 245-66.

Richert ND, Ostuni JL, Bash CN, Leist TP, McFarland HF, Frank JA. Interferon beta-1b and intravenous methylprednisolone promote lesion recovery in multiple sclerosis. Mult Scler 2001; 7(1): 49-58.

Ricote M, Li AC, Willson TM, Kelly CJ, Glass CK. The peroxisome proliferator-activated receptor-gamma is a negative regulator of macrophage activation. Nature 1998; 391(6662): 79-82.

Ridet JL, Malhotra SK, Privat A, Gage FH. Reactive astrocytes: cellular and molecular cues to biological function. Trends Neurosci 1997; 20(12): 570-7.

Rizopoulos D. Latent Trait Models under IRT. In: Rizopoulos D, editor. 1.0-0 ed; 2013-12-20. p. Analysis of multivariate dichotomous and polytomous data using latent trait models under the Item Response Theory approach. It includes the Rasch, the Two-Parameter Logistic, the Birnbaum's Three-Parameter, the Graded Response, and the Generalized Partial Credit Models.

Rogg J, Rutigliano M, Yonas H, Johnson DW, Pentheny S, Latchaw RE. The acetazolamide challenge: imaging techniques designed to evaluate cerebral blood flow reserve. AJR Am J Roentgenol 1989; 153(3): 605-12.

Rosell A, Cuadrado E, Ortega-Aznar A, Hernandez-Guillamon M, Lo EH, Montaner J. MMP-9-positive neutrophil infiltration is associated to blood-brain barrier breakdown and basal lamina type IV collagen degradation during hemorrhagic transformation after human ischemic stroke. Stroke; a journal of cerebral circulation 2008; 39(4): 1121-6.

Rosenberg GA, Cunningham LA, Wallace J, Alexander S, Estrada EY, Grossetete M*, et al.* Immunohistochemistry of matrix metalloproteinases in reperfusion injury to rat brain: activation of MMP-9 linked to stromelysin-1 and microglia in cell cultures. Brain Res 2001; 893(1-2): 104-12.

Rosenberg GA, Estrada EY, Dencoff JE. Matrix metalloproteinases and TIMPs are associated with blood-brain barrier opening after reperfusion in rat brain. Stroke; a journal of cerebral circulation 1998; 29(10): 2189-95.

Rosenberg GA, Sullivan N, Esiri MM. White matter damage is associated with matrix metalloproteinases in vascular dementia. Stroke; a journal of cerebral circulation 2001; 32(5): 1162-8.

Sairanen TR, Lindsberg PJ, Brenner M, Siren AL. Global forebrain ischemia results in differential cellular expression of interleukin-1beta (IL-1beta) and its receptor at mRNA and protein level. Journal of cerebral blood flow and metabolism : official journal of the International Society of Cerebral Blood Flow and Metabolism 1997; 17(10): 1107-20.

Salinas CA, Searle GE, Gunn RN. The simplified reference tissue model: model assumption violations and their impact on binding potential. Journal of cerebral blood flow and metabolism : official journal of the International Society of Cerebral Blood Flow and Metabolism 2015; 35(2): 304-11.

Sato-Maeda M, Fujimura M, Kanoke A, Morita-Fujimura Y, Niizuma K, Tominaga T. Transient middle cerebral artery occlusion in mice induces neuronal expression of RNF213, a susceptibility gene for moyamoya disease. Brain Res 2016; 1630: 50-5.

Schaefer PW, Grant PE, Gonzalez RG. Diffusion-weighted MR imaging of the brain. Radiology 2000; 217(2): 331-45.

Scott RM, Smith ER. Moyamoya disease and moyamoya syndrome. N Engl J Med 2009; 360(12): 1226-37.

Scuteri A, Nilsson PM, Tzourio C, Redon J, Laurent S. Microvascular brain damage with aging and hypertension: pathophysiological consideration and clinical implications. J Hypertens 2011; 29(8): 1469-77.

Shi Z, Zhang X, Chen Z, Liebeskind DS, Lou M. Elevated thyroid autoantibodies and intracranial stenosis in stroke at an early age. Int J Stroke 2014; 9(6): 735-40.

Shimada IS, Borders A, Aronshtam A, Spees JL. Proliferating reactive astrocytes are regulated by Notch-1 in the peri-infarct area after stroke. Stroke; a journal of cerebral circulation 2011; 42(11): 3231-7.

Shimada IS, Peterson BM, Spees JL. Isolation of locally derived stem/progenitor cells from the peri-infarct area that do not migrate from the lateral ventricle after cortical stroke. Stroke; a journal of cerebral circulation 2010; 41(9): e552-60.

Smith DH, Uryu K, Saatman KE, Trojanowski JQ, McIntosh TK. Protein accumulation in traumatic brain injury. Neuromolecular Med 2003; 4(1-2): 59-72.

Solbach C, Uebele M, Reischl G, Machulla HJ. Efficient radiosynthesis of carbon-11 labelled uncharged Thioflavin T derivatives using [11C]methyl triflate for beta-amyloid imaging in Alzheimer's Disease with PET. Appl Radiat Isot 2005; 62(4): 591-5.

Sonobe S, Fujimura M, Niizuma K, Nishijima Y, Ito A, Shimizu H*, et al.* Temporal profile of the vascular anatomy evaluated by 9.4-T magnetic resonance angiography and histopathological analysis in mice lacking RNF213: a susceptibility gene for moyamoya disease. Brain Res 2014; 1552: 64-71.

Song SK, Yoshino J, Le TQ, Lin SJ, Sun SW, Cross AH*, et al.* Demyelination increases radial diffusivity in corpus callosum of mouse brain. NeuroImage 2005; 26(1): 132-40.

Song WC. Biochemistry and reproductive endocrinology of estrogen sulfotransferase. Ann N Y Acad Sci 2001; 948: 43-50.

Soros P, Whitehead S, Spence JD, Hachinski V. Antihypertensive treatment can prevent stroke and cognitive decline. Nat Rev Neurol 2013; 9(3): 174-8.

Stankoff B, Freeman L, Aigrot MS, Chardain A, Dolle F, Williams A*, et al.* Imaging central nervous system myelin by positron emission tomography in multiple sclerosis using [methyl-(1)(1)C]-2-(4'-methylaminophenyl)- 6-hydroxybenzothiazole. Annals of neurology 2011; 69(4): 673-80.

Straub RH. The complex role of estrogens in inflammation. Endocrine reviews 2007; 28(5): 521-74.

Suzuki J, Kodama N. Moyamoya disease--a review. Stroke; a journal of cerebral circulation 1983; 14(1): 104-9.

Suzuki J, Takaku A. Cerebrovascular "moyamoya" disease. Disease showing abnormal net-like vessels in base of brain. Arch Neurol 1969; 20(3): 288-99.

Takagi M, Miki Y, Miyashita M, Hata S, Yoda T, Hirakawa H*, et al.* Intratumoral estrogen production and actions in luminal A type invasive lobular and ductal carcinomas. Breast Cancer Res Treat 2016; 156(1): 45-55.

Takagi Y, Kikuta K, Nozaki K, Fujimoto M, Hayashi J, Imamura H*, et al.* Expression of hypoxia-inducing factor-1 alpha and endoglin in intimal hyperplasia of the middle

cerebral artery of patients with Moyamoya disease. Neurosurgery 2007a; 60(2): 338-45; discussion 45.

Takagi Y, Kikuta K, Nozaki K, Hashimoto N. Histological features of middle cerebral arteries from patients treated for Moyamoya disease. Neurol Med Chir (Tokyo) 2007b; 47(1): 1-4.

Takagi Y, Kikuta K, Sadamasa N, Nozaki K, Hashimoto N. Caspase-3-dependent apoptosis in middle cerebral arteries in patients with moyamoya disease. Neurosurgery 2006; 59(4): 894-900; discussion -1.

Tatu L, Moulin T, Vuillier F, Bogousslavsky J. Arterial territories of the human brain. Front Neurol Neurosci 2012; 30: 99-110.

Team R. RStudio: Integrated Development Environment for R. In: RStudio I, editor. RStudio: Integrated Development for R RStudio, Inc. Desktop ed. Boston, MA.: RStudio, Inc.; 2015.

Thal DR, Rub U, Orantes M, Braak H. Phases of A beta-deposition in the human brain and its relevance for the development of AD. Neurology 2002; 58(12): 1791-800.

Thal DR, Rub U, Schultz C, Sassin I, Ghebremedhin E, Del Tredici K*, et al.* Sequence of Abeta-protein deposition in the human medial temporal lobe. J Neuropathol Exp Neurol 2000; 59(8): 733-48.

Thomas BA, Erlandsson K, Modat M, Thurfjell L, Vandenberghe R, Ourselin S*, et al.* The importance of appropriate partial volume correction for PET quantification in Alzheimer's disease. Eur J Nucl Med Mol Imaging 2011; 38(6): 1104-19.

Toyama H, Ye D, Ichise M, Liow JS, Cai L, Jacobowitz D*, et al.* PET imaging of brain with the beta-amyloid probe, [11C]6-OH-BTA-1, in a transgenic mouse model of Alzheimer's disease. Eur J Nucl Med Mol Imaging 2005; 32(5): 593-600.

Uchino K, Johnston SC, Becker KJ, Tirschwell DL. Moyamoya disease in Washington State and California. Neurology 2005; 65(6): 956-8.

Uchino H, Kuroda S, Hirata K, Shiga T, Houkin K, Tamaki N. Predictors and clinical features of postoperative hyperperfusion after surgical revascularization for moyamoya disease: a serial single photon emission CT/positron emission tomography study. Stroke; a journal of cerebral circulation 2012; 43(10): 2610-6.

Vagal AS, Leach JL, Fernandez-Ulloa M, Zuccarello M. The acetazolamide challenge: techniques and applications in the evaluation of chronic cerebral ischemia. AJNR Am J Neuroradiol 2009; 30(5): 876-84.

Valles SL, Dolz-Gaiton P, Gambini J, Borras C, Lloret A, Pallardo FV*, et al.* Estradiol or genistein prevent Alzheimer's disease-associated inflammation correlating with an increase PPAR gamma expression in cultured astrocytes. Brain Res 2010; 1312: 138-44.

van Everdingen KJ, van der Grond J, Kappelle LJ, Ramos LM, Mali WP. Diffusion-weighted magnetic resonance imaging in acute stroke. Stroke; a journal of cerebral circulation 1998; 29(9): 1783-90.

Vercellino M, Masera S, Lorenzatti M, Condello C, Merola A, Mattioda A*, et al.* Demyelination, inflammation, and neurodegeneration in multiple sclerosis deep gray matter. J Neuropathol Exp Neurol 2009; 68(5): 489-502.

Wardak M, Wong KP, Shao W, Dahlbom M, Kepe V, Satyamurthy N*, et al.* Movement correction method for human brain PET images: application to quantitative analysis of dynamic 18F-FDDNP scans. Journal of nuclear medicine : official publication, Society of Nuclear Medicine 2010; 51(2): 210-8.

Weinberg DG, Arnaout OM, Rahme RJ, Aoun SG, Batjer HH, Bendok BR. Moyamoya disease: a review of histopathology, biochemistry, and genetics. Neurosurg Focus 2011a; 30(6): E20.

Weinberg DG, Rahme RJ, Aoun SG, Batjer HH, Bendok BR. Moyamoya disease: functional and neurocognitive outcomes in the pediatric and adult populations. Neurosurg Focus 2011b; 30(6): E21.

Weissbrod E. Moyamoya. Monroe Carrell, Jr. Children's Hospital at Vanderbilt University Medical Center; 2011.

Weston GC, Haviv I, Rogers PA. Microarray analysis of VEGF-responsive genes in myometrial endothelial cells. Mol Hum Reprod 2002; 8(9): 855-63.

Williams K, Jr., Ulvestad E, Cragg L, Blain M, Antel JP. Induction of primary T cell responses by human glial cells. J Neurosci Res 1993; 36(4): 382-90.

Wilson AA, Garcia, A., Chestakova, A., Kung, H. and Houle, S. A rapid one-step radiosynthesis of the β -amyloid imaging radiotracer N-methyl-[11C]2-(4′ -methylaminophenyl)-6-hydroxybenzothiazole ([11C]-6-OH-BTA-1). J Label Compd Radiopharm 2004; 47: 679–82.

Wodarz R. Watershed infarctions and computed tomography. A topographical study in cases with stenosis or occlusion of the carotid artery. Neuroradiology 1980; 19(5): 245-8.

Wong K-P, Bergsneider M, Glenn TC, Kepe V, Barrio JR, Hovda DA*, et al.* A semi-automated workflow solution for multimodal neuroimaging: application to patients with traumatic brain injury. Brain Informatics 2015; 3(1): 1-15.

Xu Y, Yang X, Wang Z, Li M, Ning Y, Chen S*, et al.* Estrogen sulfotransferase (SULT1E1) regulates inflammatory response and lipid metabolism of human endothelial cells via PPARgamma. Molecular and cellular endocrinology 2013; 369(1-2): 140-9.

Xiao BG, Link H. Is there a balance between microglia and astrocytes in regulating Th1/Th2-cell responses and neuropathologies? Immunol Today 1999; 20(11): 477-9.

Yamamoto M, Aoyagi M, Fukai N, Matsushima Y, Yamamoto K. Differences in cellular responses to mitogens in arterial smooth muscle cells derived from patients with moyamoya disease. Stroke; a journal of cerebral circulation 1998; 29(6): 1188-93.

Yamamoto Y, Maeda Y, Kawai N, Kudomi N, Nishiyama Y. Unexpected finding of cerebral meningioma on (11)C-PiB PET. Clin Nucl Med 2013; 38(4): 292-3.

Yamashita M, Oka K, Tanaka K. Histopathology of the brain vascular network in moyamoya disease. Stroke; a journal of cerebral circulation 1983; 14(1): 50-8.

Yamashita M, Oka K, Tanaka K. Cervico-cephalic arterial thrombi and thromboemboli in moyamoya disease--possible correlation with progressive intimal thickening in the intracranial major arteries. Stroke; a journal of cerebral circulation 1984; 15(2): 264-70.

Ye H, Wong KP, Wardak M, Dahlbom M, Kepe V, Barrio JR*, et al.* Automated movement correction for dynamic PET/CT images: evaluation with phantom and patient data. PLoS One 2014; 9(8): e103745.

Yushkevich PA, Piven J, Hazlett HC, Smith RG, Ho S, Gee JC*, et al.* User-guided 3D active contour segmentation of anatomical structures: significantly improved efficiency and reliability. NeuroImage 2006; 31(3): 1116-28.

Zhao X, Sun G, Zhang J, Strong R, Song W, Gonzales N*, et al.* Hematoma resolution as a target for intracerebral hemorrhage treatment: role for peroxisome proliferator-activated receptor gamma in microglia/macrophages. Annals of neurology 2007; 61(4): 352-62.

Zhao Y, Patzer A, Herdegen T, Gohlke P, Culman J. Activation of cerebral peroxisome proliferator-activated receptors gamma promotes neuroprotection by attenuation of neuronal cyclooxygenase-2 overexpression after focal cerebral ischemia in rats. FASEB J 2006; 20(8): 1162-75.

Zwain IH, Yen SS. Neurosteroidogenesis in astrocytes, oligodendrocytes, and neurons of cerebral cortex of rat brain. Endocrinology 1999; 140(8): 3843-52.